NONLINEAR GYROSCOPIC METASTRUCTURES FOR VIBRATION ATTENUATION IN ROTORS

André Albuquerque Thomas e Brandão

Tese de Doutorado

Ciências Mecânicas

Brasília, 8 de dezembro de 2025

UNIVERSIDADE DE BRASÍLIA

Faculdade de Tecnologia

Departamento de Engenharia Mecânica

UNIVERSIDADE DE BRASÍLIA
FACULDADE DE TECNOLOGIA
DEPARTAMENTO DE ENGENHARIA MECÂNICA

NONLINEAR GYROSCOPIC METASTRUCTURES FOR VIBRATION ATTENUATION IN ROTORS

André Albuquerque Thomas e Brandão

Orientadora: Aline Souza de Paula, Dr. (ENM / UnB)
Coorientador: Adriano Fabro, Dr. (ENM/UnB)

TESE DE DOUTORADO

PUBLICAÇÃO: ENM.DM - XXX/25

BRASÍLIA/DF: 8 de dezembro de 2025

UNIVERSIDADE DE BRASÍLIA
FACULDADE DE TECNOLOGIA
DEPARTAMENTO DE ENGENHARIA MECÂNICA

Nonlinear Gyroscopic Metastructures for Vibration Attenuation in Rotors

André Albuquerque Thomas e Brandão

DISSERTAÇÃO DE DOUTORADO SUBMETIDA AO DEPARTAMENTO DE ENGENHARIA MECÂNICA DA FACULDADE DE TECNOLOGIA DA UNIVERSIDADE DE BRASÍLIA COMO PARTE DOS REQUISITOS PARCIAIS PARA A OBTENÇÃO DO GRAU DE DOUTOR/PH.D. EM CIÊNCIAS MECÂNICAS.

APROVADA POR:

Aline Souza de Paula, Dr. (ENM / UnB)
(Orientadora)

Laís Bittencourt Visnadi, Dr. (ENM / UnB)
(Examinadora Interna)

Carlos de Marqui Junior, Dr. (EESC / USP)
(Examinador Externo)

Ilmar Ferreira Santos, Dr. (DTU Construct)
(Examinador Externo)

BRASÍLIA/DF, 27 DE NOVEMBRO DE 2025.

FICHA CATALOGRÁFICA

Brandão, A. A. T.
Nonlinear Gyroscopic Metastructures for Vibration Attenuation in Rotors
[Distrito Federal] 2025.
xxi, 116p. (ENM/FT/UnB, Doutor/Ph.D., Ciências Mecânicas, 2025.
Tese de Doutorado - Universidade de Brasília.
Faculdade de Tecnologia.
Departamento de Engenharia Mecânica.
Palavras-chave:
1. Metastructures 2. Nonlinear Rotordynamics
3. Vibration Attenuation 4. Chaos
I. ENM/FT/UnB II. Título (série)

REFERÊNCIA BIBLIOGRÁFICA

Brandão, A. A. T.(2025). Metaestruturas Giroscópicas Não-lineares para Atenuação de Vibração em Rotores. Tese de Doutorado, Publicação ENM.DM - XXX/25, Departamento de Engenharia Mecânica, Universidade de Brasília, Brasília, Distrito Federal, xxi, 116p.

CESSÃO DE DIREITOS

NOME DO AUTOR: André Albuquerque Thomas e Brandão.

TÍTULO DA TESE DE DOUTORADO: Nonlinear Gyroscopic Metastructures for Vibration Attenuation in Rotors.

GRAU / ANO: DOUTOR/PH.D. / 2025

André Albuquerque Thomas e Brandão

Agradecimentos

À minha mãe. Força e motivação primeiras na minha vida, me ensinou o que é coragem e me presenteou com a calma e a pausa.

Ao meu irmão e primeiro professor, Matheus. Por me mostrar a beleza no conhecimento, o valor do cuidado com o mais fraco e cujo olhar orgulhoso é sempre meu grande prêmio.

À minha companheira da vida e cúmplice nos silêncios diários, Natasha. Pelo cuidado, pela paciência e por me apresentar à lindeza da coexistência. Por cada olhar, sorriso ou gargalhada em uma longa vida cheia de manhãs de domingo.

Ao meu pai, que me ensinou que a vida precisa de arte. Um abraço apertado e um sorriso orgulhoso cheio de saudade.

À minha eterna orientadora Aline, pela confiança contagiante e por cada conselho preciso.

Ao meu orientador Adriano pela pergunta que iniciou este trabalho e por confundir, com precisão e consistência, ciência e festa.

Ao meu afilhado Cassiano pelas noites de cinema e pipoca.

À minha afilhada Cecília por cada sorriso banguela.

À comunidade do ROSS - Open Source Rotordynamics Software.

Aos colegas da Petrobras pelas aulas e pelo incentivo.

Aos colegas da Squadra pelas tão necessárias doses de dopamina.

We live only to discover beauty.

All else is a form of waiting.

Khalil Gibran

Resumo

Metaestruturas Giroscópicas Não-lineares para Atenuação de Vibração em Rotores

Autor: André Albuquerque Thomas e Brandão

Orientadora: Aline Souza de Paula, Dr. (ENM / UnB)

Coorientador: Adriano Fabro, Dr. (ENM/UnB)

Programa de Pós Graduação em Ciências Mecânicas

Brasília, 8 de dezembro de 2025

O potencial de aplicação das metaestruturas para de atenuação de vibrações mecânicas tem se mostrado promissor para aplicação em diversos campos recentemente. Esta tese apresenta resultados e análises que estabelecem os fundamentos técnicos que viabilizam a exploração de dois aspectos principais de tais estruturas: (1) a investigação da aplicação das metaestruturas para atenuação de vibrações em rotores e (2) os efeitos da não linearidades em seu desempenho geral de atenuação de vibrações, bem como a fenomenologia associada. Uma abordagem em três etapas foi adotada para permitir uma compreensão progressiva dos fenômenos com nível crescente de complexidade. Em uma primeira etapa, um rotor bi-apoiado com ressonadores lineares foi analisado, levando a uma descrição detalhada do impacto dos efeitos giroscópicos nos mecanismos tradicionais de formação de bandgaps. Os resultados mostraram atenuação consistente de vibrações para arranjos de ressonadores tanto translacionais quanto rotacionais, bem como comportamentos únicos como o fenômeno de polarização e coexistência de modos ópticos e acústicos. Em uma segunda etapa, o conceito de osciladores não lineares foi introduzido usando um modelo base de cadeia unidimensional simples com acoplamentos biestáveis. Os resultados revelaram os efeitos do comportamento caótico no desempenho geral de atenuação de vibrações, especialmente na ampliação da largura de banda de atenuação. Análises adicionais também revelaram que os mecanismos envolvidos na atenuação de vibrações são fundamentalmente diferentes daqueles observados em sua contraparte linear. Finalmente, o mesmo conceito de ressonador não linear foi aplicado a uma estrutura rotativa, o que levou ao surgimento de padrões de resposta dinâmica singulares com degradação do desempenho de atenuação em algumas faixas de frequência. Estas aparentes desvantagens da aplicação impulsionaram o desenvolvimento e a proposta de estratégias inovadoras de disposição e sintonia dos osciladores que melhoram o desempenho geral do sistema, fornecendo recursos práticos valiosos para o projeto de tais metaestruturas.

Palavras-chaves: Metaestruturas; Rotodinâmica Não-linear; Atenuação de vibração; Caos.

Abstract

Nonlinear Gyroscopic Metastructures for Vibration Attenuation in Rotors

Author: André Albuquerque Thomas e Brandão

Supervisor: Aline Souza de Paula, Dr. (ENM / UnB)

Co-supervisor: Adriano Fabro, Dr. (ENM/UnB)

PhD in Mechanical Sciences

Brasília, 2025

The vibration attenuation capabilities of metastructures have demonstrated promising potential for application in several fields. This thesis presents results and analyses that lay the foundations of understanding for the ultimate goal of exploring two main aspects of such structures: (1) the investigation of its application for vibration attenuation in rotors and (2) the effects of nonlinearities on its overall vibration attenuation performance as well as the associated phenomenology. A three-step approach was adopted to allow for a progressive understanding of the phenomena with increasing level complexity. In the first place, a linear rotor system with disk resonator attachments is analyzed, leading to a detailed description of the impact of gyroscopic effects on the traditional bandgap formation mechanisms. The results showed consistent vibration attenuation for both translational and rotational resonator arrangements, as well as unique behaviors such as polarization phenomenon and coexistence of optical and acoustic modes. In a second step, the concept of non-linear oscillators is introduced using a simpler 1-D chain base model with bistable attachments. The results revealed the effects of chaotic behavior on the overall vibration attenuation performance, especially in attenuation bandwidth widening. Further analyses also revealed that the mechanisms involved in the vibration attenuation are fundamentally different from those observed in its linear counterpart. Finally, the same nonlinear resonator concept was applied to a rotating structure, which led to the emergence of unique dynamic response patterns with degradation of attenuation performance in some frequency ranges. These apparent disadvantages have driven the development and proposal of innovative layout and tuning strategies that improve the system's general performance, providing valuable insight for the practical design of such metastructures.

Key-words: Metastructures; Nonlinear Rotordynamics; Vibration Attenuation; Chaos.

Table of Contents

1 INTRODUCTION . . . 2
1.1 Contributions . . . 4

2 BIBLIOGRAPHIC REVIEW . . . 6
2.1 Mechanical Metamaterials . . . 7
2.1.1 Metastructure fundamentals . . . 8
2.1.2 Bandgap performance improvement . . . 9
2.1.3 Scale . . . 10
2.1.4 Non-reciprocity . . . 10
2.1.5 Nonlinear metastructures . . . 11
2.1.6 Tunability and control . . . 13
2.2 Rotordynamics . . . 13
2.3 Final remarks . . . 15

3 THEORETICAL BACKGROUND . . . 18
3.1 Metastructures for Vibration Attenuation . . . 18
3.2 Rotordynamics . . . 25
3.3 Numerical solution of nonlinear differential equations . . . 33
3.3.1 The Harmonic Balance Method . . . 33
3.3.2 Stability of periodic solutions in nonlinear systems . . . 37
3.3.2.1 Floquet multipliers . . . 37

4 RAINBOW GYROSCOPIC DISK METASTRUCTURES FOR BROADBAND VIBRATION ATTENUATION IN ROTORS . . . 39
4.1 Rotor model . . . 40
4.1.1 Translational resonators . . . 44
4.1.1.1 Forced response . . . 46
4.1.2 Rotational resonators . . . 52
4.1.2.1 Forced response . . . 53
4.2 Turboexpander Application . . . 60

4.3 Final Remarks . . . 68

5 BANDGAP FORMATION AND CHAOS IN PERIODIC LATTICES WITH GRADED BI-STABLE RESONATORS . . . 70
5.1 System Description . . . 70
5.2 Results . . . 72
5.3 Final Remarks . . . 82

6 NONLINEAR GYROSCOPIC METASTRUCTURES . . . 84
6.1 System Description . . . 84
6.1.1 System parameters . . . 88
6.2 Results and discussion . . . 90
6.2.1 Standard Oscillator Distribution . . . 90
6.2.2 Modally Matched Distribution of the Oscillators . . . 96
6.2.3 Attenuation bandwidth comparison . . . 104
6.3 Final Remarks . . . 105

7 CONCLUSIONS . . . 106
7.1 Linear gyroscopic resonators . . . 106
7.2 Nonlinear 1-D oscillators . . . 107
7.3 Nonlinear gyroscopic oscillators . . . 107
7.4 Final remarks . . . 108

BIBLIOGRAPHY . . . 110

List of Figures

Figure 2.1 – Organization of the following chapters. 17
Figure 3.1 – Basic 1 DoF arrangement (a) and simple DVA system (b). 20
Figure 3.2 – Frequency Response Functions and phase of a base 1DoF system with and without DVA. 20
Figure 3.3 – Phase relationships between elastic link force and base mass velocity. . 21
Figure 3.4 – Simplified periodic chain with 2-cell periodicity and resonators attachments. 21
Figure 3.5 – Frequency response function showing Bragg Scattering and Locally Resonant bandgaps. 23
Figure 3.6 – Bandgap widening with rainbow resonators. 24
Figure 3.7 – Two degrees of freedom rotor model. 26
Figure 3.8 – Orbit representation as the composition of two orthogonal coordinates. 27
Figure 3.9 – Bode plots of an unbalanced Jeffcott Rotor for different values of damping factor ζ. 29
Figure 3.10–Four degrees of freedom Jeffcott rotor. 30
Figure 3.11–Typical Campbell Diagram and mode shapes for a 4 DoF Jeffcott rotor. (a) Backward conical mode, (b) Forward conical mode, (c) Forward cylindrical mode and (d) Backward cylindrical mode. 32
Figure 3.12–Frequency Response obtained with both HBM and direct integration. . 38
Figure 4.1 – Rotor FEM model of the shaft (grey), rigid axisymmetric disks (red), isotropic bearings (dark blue) and resonators (light blue), the bearings at the ends. 40
Figure 4.2 – Stiffness matrix arrangement in sparse representation. 41
Figure 4.3 – Campbell Diagram and the mode shapes of the corresponding synchronous natural frequencies of the bare the rotor. 43
Figure 4.4 – Campbell diagrams with translational resonators tuned to 377 rad/s. (a) Periodic resonators and A_{avg} colorscale. (b) Periodic resonators and ϕ_{avg} colorscale. (c) Rainbow resonators and A_{avg} colorscale. (d) Rainbow resonators and ϕ_{avg} colorscale. 45

Figure 4.5 – Major axis response with translational resonators tuned to 377 rad/s. (a) Forward excitation. (b) Backward excitation. 47

Figure 4.6 – Response amplitudes as a function of the frequency and rotation speed of the shaft due to backward excitation. (a) Bare rotor. (b) Translational rainbow resonators. 48

Figure 4.7 – Deflected shapes for periodic translational resonators tuned to 377 rad/s with forward excitation. 50

Figure 4.8 – Deflected shapes for translational rainbow resonators tuned to 377 rad/s with forward excitation. 51

Figure 4.9 – Campbell diagrams with rotational resonators tuned to 634.4 rad/s. (a) Periodic resonators and A_{avg} colorscale. (b) Periodic resonators and ϕ_{avg} colorscale. (c) Rainbow resonators and A_{avg} colorscale. (d) Rainbow resonators and ϕ_{avg} colorscale. 54

Figure 4.10–Amplitude of the frequency response with rotational resonators tuned to 634.4 rad/s. (a) Forward excitation. (b) Backward excitation. 54

Figure 4.11–Campbell diagram (a) and the amplitude of the frequency response to backward excitation (b) with rotational resonators tuned to $634.4 rad/s$ and $m = 3$. 55

Figure 4.12–Response amplitudes as a function of the frequency and rotation speed of the shaft due to backward excitation. 56

Figure 4.13–Deflected shapes for rotational rainbow resonators tuned to $634.4 rad/s$ with forward excitation. 57

Figure 4.14–Deflected shapes for rotational rainbow resonators tuned to 634.4 rad/s with backward excitation. 58

Figure 4.15–Spatially averaged amplification and phase angle with rotational resonators tuned to 634.4 rad/s subject to backward excitation. (a) Periodic resonators and A_{avg} colorscale. (b) Periodic resonators and ϕ_{avg} colorscale. (c) Rainbow resonators and A_{avg} colorscale. (d) Rainbow resonators and ϕ_{avg} colorscale. 59

Figure 4.16–Spatially averaged amplification and phase angle with rotational resonators tuned to 634.4 rad/s subject to forward excitation. (a) Periodic resonators and A_{avg} colorscale. (b) Periodic resonators and ϕ_{avg} colorscale. (c) Rainbow resonators and A_{avg} colorscale. (d) Rainbow resonators and ϕ_{avg} colorscale. 60

Figure 4.17–Typical turboexpander-compressor showing key parts (API Std 617, 2022). Reproduced courtesy of the American Petroleum Institute. . . . 61

Figure 4.18–Turboexpander compressor rotor model. 62

Figure 4.19–Campbell diagram of the turboexpander-compressor before application of resonators. 62

Figure 4.20–Campbell diagram of the turboexpander-compressor before application of resonators. 64

Figure 4.21–Unbalance responses plots for turboexpander compressor with midspan unbalance. (a) Left side bearing and (b) right side bearing. 64
Figure 4.22–Unbalance responses plots for turboexpander compressor with left side impeller unbalance. (a) Left side bearing and (b) right side bearing. . . 65
Figure 4.23–Mode shape of the target natural frequency. Red dashed lines indicate the position of the resonators. 66
Figure 4.24–Response heatmap for unitary forward excitation. (a) Bare rotor, (b) rotor with identical resonators and (c) rainbow resonators. 67
Figure 4.25–Response heatmap for unitary backward excitation. (a) Bare rotor and (b) rotor with identical resonators. 67
Figure 4.26–Averaged amplification and phase angle maps for identical (a-b) and rainbow resonators (c-d). 68
Figure 5.1 – 1-D chain arrangement used for the simulations in this chapter. 70
Figure 5.2 – Frequency Response plots comparing the system's response for different excitation amplitudes: (a) 1000 N, (b) 3000 N, (c) 6000 N and (d) 9000 N. 73
Figure 5.3 – Bifurcation Diagrams for different excitation amplitudes: (a) 1000 N, (b) 3000 N, (c) 6000 N, (d) 9000 N. 74
Figure 5.4 – Frequency Response heatmap of the system for different excitation amplitudes: (a) 1000 N, (b) 3000 N, (c) 6000 N and (d) 9000 N. 75
Figure 5.5 – Spatially averaged amplification (a) and relative phase (b) between base chain and resonators for excitation amplitude of 1000 N. 76
Figure 5.6 – Spatially averaged amplification (a) and relative phase (b) between base chain and resonators for excitation amplitude of 6000 N. 76
Figure 5.7 – Spatially averaged amplification (a) and relative phase (b) between base chain and resonators for excitation amplitude of 9000 N. 77
Figure 5.8 – Spatial distribution of vibration for the linear system (a) and for the non linear system with different excitation amplitudes: (b) 1000 N, (c) 6000 N and (d) 9000 N. 77
Figure 5.9 – Frequency Response plots comparing the system's response with graded resonators and with different excitation amplitudes: (a) 1000 N, (b) 3000 N, (c) 6000 N and (d) 9000 N. 79
Figure 5.10–Bifurcation Diagrams for different excitation amplitudes with graded resonators: (a) 1000 N, (b) 3000 N, (c) 6000 N, (d) 9000 N. 79
Figure 5.11–Frequency Response heatmap of the system with graded resonators for different excitation amplitudes: (a) 1000 N, (b) 3000 N, (c) 6000 N and (d) 9000 N. 80
Figure 5.12–Spatially averaged amplification (a) and relative phase (b) between base chain and graded resonators for excitation amplitude of 1000 N. 81
Figure 5.13–Spatially averaged amplification (a) and relative phase (b) between base chain and graded resonators for excitation amplitude of 6000 N. 81

Figure 5.14–Spatially averaged amplification (a) and relative phase (b) between base chain and graded resonators for excitation amplitude of 9000 N. 81
Figure 5.15–Spatial distribution of vibration with graded resonators for the linear system (a) and for the non linear system with different excitation amplitudes: (b) 1000 N, (c) 6000 N and (d) 9000 N. 82
Figure 6.1 – Rotor FEM model of the shaft (grey), rigid axisymmetric disks (red), isotropic bearings (green) and oscillators (blue) and the bearings at the shaft ends. 85
Figure 6.2 – Nonlinear oscillator and rotor attachment on X-Y plane projection. . . 86
Figure 6.3 – Matrix composition of the linear stiffness components. 87
Figure 6.4 – Mode shape at the targeted natural frequency for attenuation. 90
Figure 6.5 – Frequency Response Functions for (a) forward and (b) backward excitations with identical oscillators. 91
Figure 6.6 – Frequency Response Functions for (a) forward and (b) backward excitations with graded oscillators. 92
Figure 6.7 – Frequency Response Functions for unbalance excitation. (a) Identical oscillators and (b) graded oscillators. 93
Figure 6.8 – Orbit plots of oscillator 1 (left) and shaft end (right) for linear and nonlinear oscillators. All cases correspond to identical resonators under a $10U$ unbalance excitation. Excitation frequencies are 360 rad/s for (a) and (b) and 700 rad/s for (c) and (d). 94
Figure 6.9 – Orbit plots of the oscillator and corresponding shaft node under $6U$ unbalance excitation condition, with identical oscillators and $\Omega = 503$ rad/s. (a) First leftmost oscillator. (b) Second leftmost oscillator. . . . 95
Figure 6.10–Averaged amplification and phase angle plots for high excitation amplitude. (a) Averaged amplification heatmap and (b) phase angle map for forward excitation of 500 N. (c) Averaged amplification heatmap and (d) phase angle map for unbalance excitation of $4U$. 96
Figure 6.11–Full spectrum waterfall heatmaps for the right-most element response. (a) Forward excitation of 400 N. (b) Unbalance excitation of $4U$. (c) Forward excitation of 500 N. (d) Unbalance excitation of $6U$. 97
Figure 6.12–Oscillators positioning with Modally Matched Distribution (MMD). (a) Shows the mode shape of the target natural frequency and (b) shows the adjusted distribution of oscillators. 98
Figure 6.13–Unbalance response comparison for different values of ω_0. The unbalance is set at $4U$ and the linear case uses $\omega_0 = 300$ rad/s. 99
Figure 6.14–Frequency Response Functions for (a) forward and (b) backward excitations and identical oscillators with MMD. 99
Figure 6.15–Frequency Response Functions for (a) forward and (b) backward excitations and graded oscillators with MMD. 99

Figure 6.16–Frequency Response Functions for unbalance excitation. (a) Identical oscillators and (b) graded oscillators, both with MMD. 100
Figure 6.17–Orbit plots of oscillator 1 (left) and shaft end (right) for linear and nonlinear oscillators with MMD. All cases are for identical resonators under $10U$ unbalance excitation. Excitation frequencies are 250 rad/s for (a) and (b) and 730 rad/s for (c) and (d). 100
Figure 6.18–Averaged amplification and phase angle plots for high excitation amplitude and oscillator with MMD. (a) Averaged amplification heatmap and (b) phase angle map for forward excitation of 500 N. (c) Averaged amplification heatmap and (d) phase angle map for unbalance excitation of $4U$. 101
Figure 6.19–Amplification and phase angle averaged of the first three oscillators at high excitation amplitude and oscillator with MMD. (a) Averaged amplification heatmap and (b) phase angle map for unbalance excitation of $4U$. 102
Figure 6.20–Full spectrum waterfall heatmaps for the right-most element response in the system with MMD. (a) Forward excitation of 400 N. (b) Unbalance excitation of $4U$. (c) Forward excitation of 500 N. (d) Unbalance excitation of $6U$. 103
Figure 6.21–Poincaré map for the X-direction motion of the first oscillator with forward excitation at 400 N amplitude and 600 rad/s frequency. 103
Figure 6.22–Bar chart showing a comparison of attenuation bandwith for the different configurations. 105

List of Tables

Table 1 – FEM parameters, geometrical and material properties of the rotor model. 43
Table 2 – Radial bearing input data for calculation of dynamic force coefficients. . 61
Table 3 – Resonator parameters. 63

List of abbreviations and acronyms

AFT	Alternating Frequency/Time-Domain
API	American Petroleum Institute
DFT	Direct Fourier Transform
DoF	Degrees of Freedom
DVA	Dynamic Vibration Absorber
FEM	Finite Element Method
FFT	Fast Fourier Transform
FRF	Frequency Response Function
HBM	Harmonic Balance Method
ISO	International Organization for Standardization
MMD	Modally Matched Distribution
NES	Nonlinear Energy Sink
$RK4$	Runge-Kutta 4th Order
SMA	Shape Memory Alloys
SS	Stainless Steel
VG	Viscosity Grade

List of symbols

α	Nonlinear coefficient of the Duffing oscillator $[N/m^3]$
β	Linear coefficient of the Duffing oscillator $[N/m]$
δ	Dissipative coefficient of the Duffing oscillator $[N \cdot s/m]$
ε_n	Mass gradation factor for the nth resonator [dimensionless]
λ	Floquet multiplier [dimensionless]
μ	Mass ratio between resonators and base structure [dimensionless]
ν	Frequency scaling factor for the harmonic balance method [dimensionless]
ϕ	Phase angle [rad]
ϕ_{avg}	Spatial average of phase angle [rad]
ϕ_i	Phase angle of the i-th resonator [rad]
θ_x	Rotation around x-axis [rad]
θ_y	Rotation around y-axis [rad]
ζ	Damping factor [dimensionless]
A_{avg}	Spatial average of amplification factor [dimensionless]
A_i	Amplification factor of the ith resonator [dimensionless]
c	Damping coefficient $[N \cdot s/m]$
c_0	Viscous damping between adjecent chain elements $[N \cdot s/m]$
c_p	Proportional damping coefficient [s]
c_r	Resonator damping coefficient $[N \cdot s/m]$
c_{xx}	Direct damping coefficient in x-direction $[N \cdot s/m]$
c_{yy}	Direct damping coefficient in y-direction $[N \cdot s/m]$

d	Distance between chain elements [m]
d_i	Inner diameter [m]
d_o	Outer diameter [m]
F, f	Excitation force amplitude [N]
f_{nl}	Nonlinear force [N]
F_r	Restoring force [N]
I_p	Polar moment of inertia $[kg \cdot m^2]$
$I_{p_{\text{res}}}$	Polar moment of inertia of the resonator $[kg \cdot m^2]$
I_t	Transverse moment of inertia $[kg \cdot m^2]$
$I_{t_{\text{res}}}$	Transverse moment of inertia of the resonator $[kg \cdot m^2]$
$I_{t_{\text{osc}}}$	Transverse moment of inertia of the oscillator $[kg \cdot m^2]$
k	Stiffness $[N/m]$
k_0	Stiffness between chain elements $[N/m]$
k_1	Rotational stiffness $[N \cdot m/rad]$
k_θ	Rotational coupling stiffness $[N \cdot m/rad]$
k_{lin}	Linearized oscillator stiffness $[N/m]$
k_{nl}	Nonlinear stiffness $[N/m]$
k_r	Resonator stiffness $[N/m]$
k_y	Coupling stiffness in y-direction $[N/m]$
k_{xx}	Direct stiffness coefficient in x-direction $[N/m]$
k_{xy}, k_{yx}	Cross-coupling stiffness coefficients $[N/m]$
k_{yy}	Direct stiffness coefficient in y-direction $[N/m]$
L	Length [m]
m	Mass [kg]
m_0	Reference mass [kg]
m_n	Mass of the nth resonator/oscillator [kg]
m_o	Oscillator mass [kg]

m_r	Resonator mass [kg]
N	Total number of shaft nodes [dimensionless]
N_0	Number of degrees of freedom of the chain [dimensionless]
N_1	Number of resonators [dimensionless]
N_H	Number of harmonics considered in the harmonic balance method [dimensionless]
N_o	Number of oscillators [dimensionless]
N_r	Number of resonators [dimensionless]
r	Distance between rotor center of mass and rotation axis [m]
t	Time [s]
T	Period [s]
U	Unbalance magnitude [$kg \cdot m$]
U_p	Potential energy [J]
W	Total rotor weight [kg]
x	Displacement in x-direction [m]
x_0	Stable equilibrium position of the Duffing oscillator [m]
y	Displacement in y-direction [m]
ω	Excitation frequency [rad/s]
ω_0	Reference natural frequency [rad/s]
ω_1	Rotational natural frequency [rad/s]
ω_c	Critical speed [rad/s]
ω_n	Natural frequency [rad/s]
ω_r	Resonator natural frequency [rad/s]
ω_t	Target frequency [rad/s]
Ω	Shaft rotation speed [rad/s]
Ω_c	Critical speed [rad/s]
Ω_t	Target synchronous frequency [rad/s]

$\mathbf{A}$	Harmonic balance method matrix
$\mathbf{b}$	Vector of Fourier coefficients of forces in the harmonic balance method
$\mathbf{C}$	Damping matrix $[N \cdot s/m]$
$\mathbf{f}$	Force vector $[N]$
$\mathbf{f}_{nl}$	Nonlinear force vector $[N]$
$\mathbf{G}$	Gyroscopic matrix $[kg \cdot m^2]$
$\mathbf{h}$	Vector of harmonic balance method equations
$\mathbf{H}_\omega$	Transfer matrix [variable]
$\mathbf{J}_\mathbf{z}$	Jacobian matrix
$\mathbf{K}$	Stiffness matrix $[N/m]$
$\mathbf{M}$	Mass matrix $[kg]$
$\mathbf{M}_0$	Monodromy matrix
$\mathbf{x}$	Displacement vector $[m]$
$\mathbf{z}$	Vector of Fourier coefficients of displacements $[m]$
$\mathbf{\Gamma}$	Linear operator for inverse Fourier transform

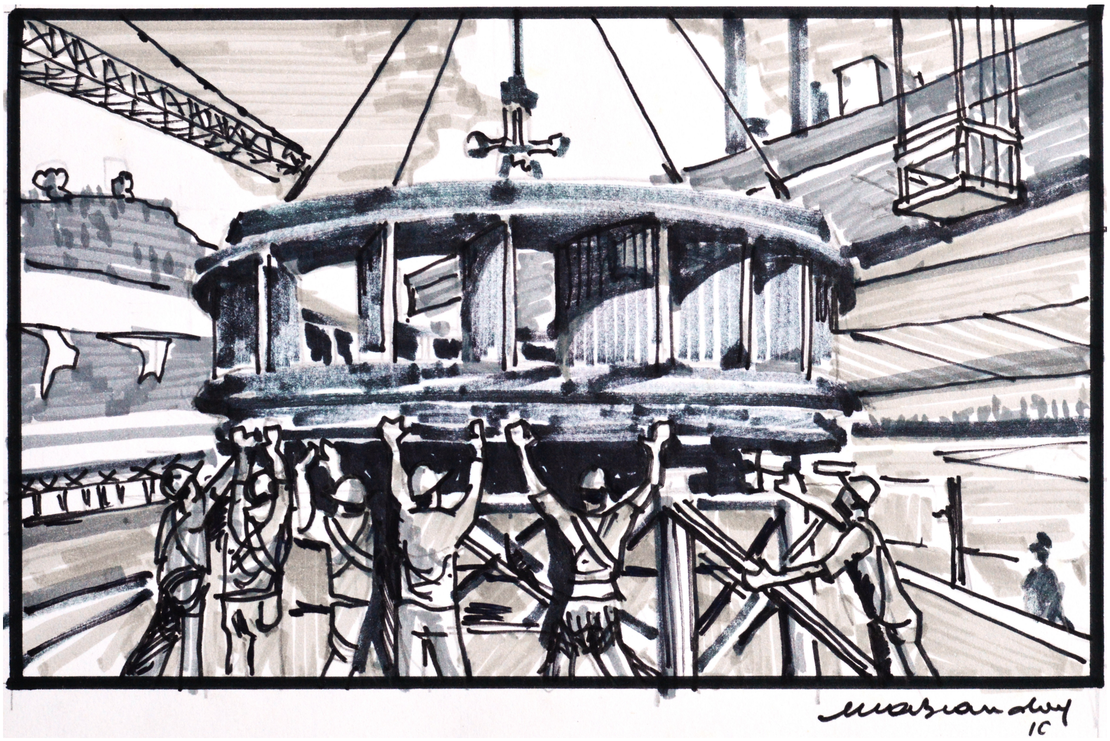

1 Introduction

The investigation of dynamical behavior emerging from periodic structures has been gaining increasing attention from the scientific community over the last 20 years. These types of structures were first investigated by Isaac Newton in the Seventeenth Century as a way to describe the velocity of sound in air (NEWTON, 1686) and continued to get a steady flow of contributions in the following centuries that built an initial basic understanding of their unique dynamic characteristics.

The first comprehensive work that structured and deepened the available knowledge about the dynamics and wave propagation in periodic structures was the book "Wave Propagation in Periodic Structures", by Léon Brillouin first published in 1946 (BRILLOUIN, 1946). The main motivation for the formulations described by Brillouin at the time was the studies of the dynamics of atoms and ended up forming the mathematical basis for the formulations of modern Quantum Mechanics.

However, more recently, the study of periodic structures has found increasingly expanding grounds for the application of large-scale structural systems. In the last 20 years, the number of papers published each year with investigations on large-scale periodic structures, or mechanical metastructures, increased more than 5 times. This recent trend is in part motivated and enabled by previously developments that formed a solid theoretical foundation for the understanding of periodic structures, such as the work of Mead (1975) where some of the most fundamental aspects of periodic systems' dynamic behavior were first described.

A practical motivation that has become central in recent work on metastructures is structural vibration attenuation. The unique properties of bandgap formation and other wave propagation restriction mechanisms make this type of structure an important tool for vibration control. Special topological configurations enable extremely flexible control of wave propagation, especially in the field of optics and waveguides, but also for mechanical systems. Broadband, low-frequency bandgap formation mechanisms in large-scale mechanical systems can enable vibration control of a myriad of structures, from industrial piping systems to building earthquake protection. Related works often focus on ways to improve the performance of these bandgaps, using topological variations, periodicity breaks (BELI et al., 2019; MENG et al., 2020a; HODGES, 1982; CAI; LIN, 1991), and nonlinear elements (XIA; RUZZENE; ERTURK, 2019; XIA; RUZZENE; ERTURK, 2020;

SHENG et al., 2021; NARISETTI; LEAMY; RUZZENE, 2010; MOSQUERA-SÁNCHEZ; De Marqui, 2024) to achieve broadband, easily tunable, and robust vibration control.

Research works that have focused on investigating the effects of nonlinear periodic structures on vibration attenuation indicate significant advantages on attenuation performance, both in bandwidth and in amplitude (MATLACK et al., 2016; LIU et al., 2011; PAI; PENG; JIANG, 2014). In many cases, as shown in Xia, Ruzzene & Erturk (2020), Brandão, de Paula & Fabro (2024), the attenuation is greatly improved by the chaotic behavior that emerges at higher input excitation amplitudes. However, these works focus on attenuating vibrations on simple beam structures using local resonators that couple only to the translation degrees of freedom of the main beam. Few works, such as Sheng et al. (2021), explore the angular component of beam vibration by attaching flexural resonators to the structure. These works, especially those developing analytical solutions, also usually consider the formulation of plane waves, since the orthogonal directions are independent (XIAO; WEN; WEN, 2012).

Exploring the behaviors that arise from the rotation of the main structures and resonators, coupling the orthogonal directions through the gyroscopic effect, is still rare (XU et al., 2023; LAMAS; NICOLETTI, 2024) and does not always focus on the vibration attenuation potential. Gyroscopic effects have fundamental implications on the system's dynamics, creating new forms of interaction between the base structure and attached resonating structures. Furthermore, the combination of these gyroscopic-related effects with the nonlinear effects reported in the literature may provide a promising way to efficient and robust vibration attenuation in rotating structures. The current challenges in the design of rotating machinery in industry are still numerous (DELLACORTE; BRUCKNER, 2011). The search for innovative ways to produce machines with lower vibration levels and better reliability in increasingly challenging applications is a prolific field that needs to be continuously pushed. This thesis contributes with a possible solution, or additional design tool, that can be used to overcome some of these challenges.

The central proposal of this thesis is to apply the vibration attenuation capabilities of metastructures to rotating systems, presenting a new alternative for vibration control in rotating machinery rotordynamic design. The goal is pursued by applying the concept of locally resonant metastructures to rotor systems and subsequently exploring the limits and opportunities that arise from this combination, which is done by characterizing the phenomenology of the system's behavior and exploring alternative setups such as rainbow arrangements and nonlinear oscillators. This innovative concept opens up a new research area for Gyroscopic Metastructures.

The **general objectives** of this thesis are to (1) explore the vibration attenuation capabilities of linear and nonlinear metastructures in rotating systems and (2) develop and present a set of tools and methods to model and analyze this type of system. The **specific objectives** of the thesis are (1) to investigate and discuss how gyroscopic effects can impact the dynamics of rotating metastructures, (2) to develop a case study applying the concepts developed to the model of a real industrial machine, (3) explore and propose design optimization practices that can improve vibration attenuation performance, and (4) enable a deeper understanding of the underlying phenomena that generate chaotic vibration attenuation in nonlinear metastructures.

The thesis follows a specific progressive investigation path that allowed the understanding of key physical phenomena separately and in a systematic way. This strategy consisted of 3 steps: (1) linear metastructure on a rotating shaft as base structure in Chapter 4, (2) nonlinear bi-stable metastructure on a non-rotating 1D lattice as base structure in Chapter 5 and (3) nonlinear bi-stable metastructure on a rotating shaft as base structure in Chapter 6.

1.1 Contributions

The main contribution of this work is to explore the dynamic behavior and vibration attenuation performance of periodic structures considering the gyroscopic effect and nonlinearities. As the main, high-level results of this investigation we highlight: (1) the clear definition of the main aspects of these periodic systems' behaviors, including the influence of the gyroscopic effect and functional gradation in linear and nonlinear systems; (2) the definition and understanding of the underlying mechanisms that create such behaviors, especially vibration attenuation; and ultimately (3) to provide the foundations of applicability and design aspects to pave the way for future practical applications.

The list of main publications associated with this thesis is presented below.

- Brandão, de Paula & Fabro (2022) - In this work, the concept of periodic locally resonant metastructures has been extended to rotors in two different configurations: identical and rainbow resonators. The results show consistent vibration attenuation and unique behaviors such as the coexistence of acoustic and optical modes. The content of this work is presented in Chapter 4.
- Brandão, de Paula & Fabro (2024) - This work explores the vibration attenuation mechanisms in a 1-D chain with an array of bi-stable attachments, both in periodic and graded arrangements. The results show amplitude-dependent, broadband vibration amplitude effects, especially when chaotic behavior emerges. The mechanisms of vibration attenuation are also discussed and have been shown to be significantly different than those in linear systems.The content of this work is presented in Chapter 5.
- Brandão, de Paula & Fabro (2025) - The work combines the fundamental concepts of the previously mentioned papers to investigate the behavior and vibration attenuation capabilities of nonlinear oscillators on a rotating system. In this case, particular phenomena, previously not clearly present, were observed. Novel strategies for tuning

and positioning the oscillators have been proposed and have been shown to overcome some of the weaknesses in attenuation performance.The content of this work is presented in Chapter 6.

2 Bibliographic Review

In the last decade, there has been a fast and substantial increase in interest in investigating periodic structures, which in some contexts have become known as *metamaterials* (WALSER, 2000) or *metastructures*. This fast evolution was accompanied by a significant increase in richness of the academic research environment during the period, with the basic initial concepts branching out to several different knowledge domains, applications and with different levels of complexity.

The exploration of the basic phenomena of periodic structures was initially largely focused on electromagnetism and the manipulation of electromagnetic waves, in works such as Joannopoulos, Villeneuve & Fan (1997), Walser (2001), Biswas, Li & Ho (2004), Baba et al. (2004), which often applied the term *photonic crystals* to refer to these new materials. However, some works were already building the foundations that allowed the expansion of these same concepts to mechanical systems (MEAD, 1996; VASSEUR et al., 1994; KUSHWAHA et al., 1994).

At a certain point, research interest shifted to become predominantly focused on the study of mechanical wave propagation, in a prolific exploration of several different and creative configurations of *phononic crystals* or *sonic crystals*. This shift may be attributed to the unique frequency response characteristics of these systems, which opened a new realm of possible applications for acoustics and structural dynamics, especially in vibration attenuation and control (CREMER; HECKL; PETERSSON, 2005; SÁNCHEZ-DEHESA et al., 2011; VASILEIADIS et al., 2021).

The effects of periodicity and local resonance can be explored for enhancing the structural dynamics and improve broadband vibration attenuation (WU et al., 2021). Additionally, it has been shown that the rainbow distribution can further increase the attenuation bandwidth with no added mass by a suitable choice of spatial distribution of the resonance frequency (ZHU et al., 2013; BELI et al., 2019; MENG et al., 2020d; MENG et al., 2020a). Typically, gradient spatial profiles are used, but other types of spatial profiles have also been shown to be effective (CELLI et al., 2019; FABRO et al., 2021; FABRO; MENG; CHRONOPOULOS, 2021). This approach is also known as rainbow metamaterial, originally proposed in the context of optics (TSAKMAKIDIS; BOARDMAN; HESS, 2007), and it uses spatial gradient changes in the metastructure for the creation of wider bandgaps (BELI et al., 2019; MENG et al., 2020d) and can be extended to 2D and

3D metastructures (MENG et al., 2020b; MENG et al., 2020a). Similar effects of bandgap widening can also be achieved using random disorder (CELLI et al., 2019) and correlated disorder (FABRO; MENG; CHRONOPOULOS, 2021).

At this stage, the focus was still on relatively small-scale structures. The term *crystal* itself implies an interest in the average properties of a macroscopic body composed of a large number of smaller unit cells. Or, as described by Walser (2001), "(...) *achieving performance beyond that of conventional macroscopic composites (...) by first disassembling, then recombining macroscopic constituents*".

The concepts were then gradually diffused to larger-scale structures. These new investigations explored systems that no longer relied on a large size difference between unit cells and the whole structure, but still manifested some of the unique and potentially useful dynamic characteristics of conventional metamaterials. Sugino et al. (2017) provides an important foundation for this new trend when it demonstrates that an elastic beam with as few as seven locally resonant unit cells can already achieve vibration attenuation performance similar to that of the same beam with an infinite number of unit cells. This new approach paved the way for practical engineering applications, where systems have to be finite and spatially constrained by manufacturing processes, economic restrictions, and other application-specific restrictions (RICHARDS; PINES, 2003; POLICARPO; NEVES; RIBEIRO, 2010; LAMAS; NICOLETTI, 2024).

The work published by Hussein, Leamy & Ruzzene (2014) presents a comprehensive review of the main contributions and motivations behind the developments in periodic structures and phononic materials dating back to the first investigations by Issac Newton. The review paper finally highlights that the next frontier for the research of mechanical metamaterials would be in enabling the ultrahigh- and ultralow-frequency application.

Soon after, Mace (2014) complemented the discussions of Hussein, Leamy & Ruzzene (2014) by adding a more objective perspective on some of the most fundamental aspects of the developments in metamaterials. More recent reviews like Dalela, Balaji & Jena (2021) and Wu et al. (2025) provide an update on the latest developments in the field, placing Artificial Intelligence (AI) as a central tool in the development and optimization of future metamaterials.

However, the integration of these concepts with rotating systems, where gyroscopic effects introduce additional complexity and opportunities, remains largely unexplored.

2.1 Mechanical Metamaterials

This section reviews the current state of metamaterial research, identifying three main research trends and highlighting the promising but underdeveloped intersection with rotordynamics, which forms the foundation for the novel contributions presented in this thesis.

Recent contributions in the field focused on the following main categories: metastructure fundamentals (Section 2.1.1), bandgap performance improvement (Section 2.1.2), scale (Section 2.1.3), non-reciprocity (Section 2.1.4), nonlinear metastructures (Section 2.1.5) and tunability and control (Section 2.1.6). Some of the relevant contributions in each of these categories will be briefly explored in the following sections.

2.1.1 Metastructure fundamentals

Several articles focus on the theoretical description and characterization of fundamental dynamic phenomena emerging from periodic structures. A topic that attracts significant attention is the mechanisms of bandgap formation, its definition, and the transition between different mechanisms.

There are two mechanisms for bandgap formation:

- The **Bragg scattering** mechanism is associated with small wavelengths, on the order of magnitude of the lattice unit cell. Because of that, it is usually linked to high frequency stopband regions, in which wave propagation is totally absent;
- The **Local Resonance** mechanism is associated with the resonance of local structures that guide and concentrate all the vibration energy, stopping wave propagation in the main structure. This mechanism tends to function on lower frequencies and is more easily tunable.

Liu et al. (2000) were probably the first to present an experimental study showing the concept of a locally resonant mechanism of bandgap formation. This paper focuses on showing the band structure and transmission coefficients for different frequency ranges, confirming the possibility of creating low-frequency bandgaps in real, large-scale periodic structures.

Liu & Hussein (2012) showed a detailed work in which wave propagation in an elastic beam with different kinds of periodicity is evaluated using Bloch's Theorem and the Transfer Matrix Method. The authors not only describe the influence of different types of periodicity in the system's bandgap structure, but also develop a detailed, rigorous mathematical description of the transition between Bragg-scattering and Local Resonance as bandgap formation mechanisms.

Sun and coauthors in 2010 contributed with a comprehensive evaluation of metamaterial beams and the mechanisms involved in bandgap formation in these systems (SUN; DU; PAI, 2010). This work shows formulations for both infinite beams, using the Bloch-Floquet Theorem approach, and finite structures, by using the Finite Element Method (FEM).

A significant contribution was presented in Sugino et al. (2017), when a general theory was developed to describe the bandgap formation mechanism in an elastic beam with local resonators. The theory is able to predict bandgap performance as a function of the mass ratio between beam and resonators, base frequency, and number of resonators. An especially interesting result is that for a given mass ratio, there is an optimal number of resonators that maximizes the bandgap width.

Xiao et al. (2021) extended the work of Sugino et al. (2017), developing more complete closed-form expressions for bandgap design in beam-type metastructures. The results are compared with good agreement and are able to predict bandgaps also for a small number of resonators. The expressions are therefore able to predict the optimal number of resonators for maximum bandgap width.

2.1.2 Bandgap performance improvement

Matlack et al. (2016) presented an interesting 3-D printed configuration of a cubic lattice with lumped mass inclusions that was able to achieve broadband vibration attenuation. The authors explore numerical results for high and low stiffness of the main base lattice and compare the first case with experimental results. As the authors show, the bandgap formation mechanism of these structures uses local resonances to control the occurrence of Bragg scattering.

The combination of the unique elastic properties of metamaterials with the interesting dynamic behavior of large-scale periodic structures is being explored as a way to improve bandgap performance. Liu et al. (2011) showed numerical results for the first time for a chiral metamaterial beam with local resonator inclusions that should create good bandgap performance with lightweight and high load capacity characteristics. Zhu et al. (2014) showed experimental and numerical (FEM) results for the dynamic behavior of the same design. The combination resulted in broadband vibration attenuation with no compromise on the beam's load bearing capacity, since the resonators are fitted in the structure's natural spaces.

Pai, Peng & Jiang (2014) developed a concept of acoustic metamaterial beam with local 2-dof resonators that, by creating two separate bandgaps, significantly increases the attenuation intensity and frequency range. The wave propagation along the elastic beam within the bandgaps are, of course, strongly attenuated. However, the most interesting result is that the frequency range between the two bandgaps is also significantly attenuated, creating an extended attenuation zone.

Meng et al. (2020a) and Meng et al. (2020d) applied the increasingly popular concept of rainbow metamaterials to create structures with different levels of spatial variability of their properties to achieve significant extension in the bandgap frequency range. It is shown that even variability from the manufacturing processes of such structures can generate improved vibration attenuation performance. Similar concepts have also been used by Xiao, Wen & Wen (2012), and several other works have investigated the influence of breaks in periodicity on bandgap performance enhancement as a well-know phenomenon called *Localization* (HODGES, 1982; CAI; LIN, 1991; HODGES; WOODHOUSE, 1983). This effect was experimentally demonstrated for the first time by Beli et al. (2019).

Recently, an interesting setup was explored by Dong, Chronopoulos & Yang (2021) using inerter-based periodic structures to obtain vibration attenuation on a beam structure. The inerter was first proposed by Smith (2002) as a mechanical analogous to the capacitor in electrical systems. The component adds an inertial coupling between two nodes of the system and can have the effect of isolating vibrations between two points of the system at specific frequencies. The paper presents results for 3 different arrangements of beams with oscillators that combine inerters and negative stiffness elements. In a second approach, the work explores the arrangement of a periodically supported beam element in which the supports include inerters. The arrangements showed the formation of bandgaps and good attenuation and damping effects on the evaluated systems.

2.1.3 Scale

Significant attention has been given to ultralarge-scale periodic structures, especially on seismic wave attenuation for earthquake proofing.

Krödel, Thomé & Daraio (2015) presented a study that used the concept of rainbow traps to design a seismic metastructure for wide bandgap at very low frequency range. The propagation of longitudinal and transverse waves was evaluated for different numbers of subsoil resonators. A bandgap with significant attenuation between 4-7 Hz could be achieved with 15 resonators. The simulation results were compared with data from the 1994 Northrige earthquake, and the hipothetical soil response attenuation was discussed.

Similar works developed by Colombi et al. (2016b) and Muhammad, Wu & Lim (2020) explored the natural distribution of trees in a forest as resonators for Rayleigh surface waves generated by earthquakes. The work presented by Colombi et al. shows a comparison between numerical and experimental results for an actual forest that conclude that two ultra-wide bandgaps are caused by the trees acting as local resonators for the vertical components of the Rayleigh waves. Based on that conclusion, the authors propose a concept for man-made structures for earthquake attenuation.

2.1.4 Non-reciprocity

Many of the current research works on mechanical metamaterials find motivation in the early work developed on electromagnetic and optical systems. In these systems, the waveguide concept is quite popular as a way to manipulate the direction of propagation of a wave. For mechanical systems, the development of topologies that generate non-reciprocal wave propagation can be seen as the mechanical version of a waveguide concept. In such non-reciprocal systems, wave propagation is allowed in one or more particular directions, but not in others.

Trainiti & Ruzzene (2016) presented a concept of spatiotemporal periodic elastic beam. In this example, the material properties of the structure vary in space and in time. The authors develop analytical solutions for the system in which the conventional bandgaps are identified for a simple spatial periodicity and nonreciprocal bandgaps are formed when time periodic variation is introduced. The analytical results are compared with numerical Finite Element simulations with good agreement. A similar system is investigated by Matos et al. (2022), where a pipe with two-phase flow is analytically modeled as a spatio-temporal unit cell and the results are experimentally verified.

Ruzzene, Scarpa & Soranna (2003) have shown the specific directional characteristic of wave propagation in periodic two-dimensional structures. Hexagonal and re-entrant grids with negative Poisson coefficient were simulated and the patterns of wave propagation determined for different topology parameters defining the extend of the no-propagation zones for each case. The authors' work can enable the design of structures with specific wave guidance properties.

Colombi et al. (2016a) analyzed a concept of seismic metamaterial with interesting properties. Exploring a system similar to those previously discussed here (COLOMBI et al., 2016b; MUHAMMAD; WU; LIM, 2020), the authors simulated the incidence of seismic Rayleigh waves in a series of tree-like structures of linearly varying length, what they called a *metawedge*. Different effects result from waves coming from one side of the array or the other. If coming from the tall side of the metawedge, the surface Rayleigh waves would be reflected downward and converted to bulk elastic shear waves. When propagating from the other end of the array, the waves would be diverted upward and attenuated one frequency at a time, generating a *seismic rainbow* effect, as the authors call it.

2.1.5 Nonlinear metastructures

In recent years, there has been a significant increase in the number of studies focusing on nonlinear periodic structures (DENG et al., 2021). A significant portion of these works often focuses on the enhanced bandgap performance of such structures or the characterization of nonlinear phenomena and the transition between periodic and chaotic behavior.

Two works of Xia and coauthors (XIA; RUZZENE; ERTURK, 2019; XIA; RUZZENE; ERTURK, 2020) describe a system consisting of an elastic beam with bi-stable local resonators and investigate the effects of such nonlinearity in the system's frequency response for different excitation levels. The system exhibits rich dynamic behavior with linear intrawell, nonlinear intrawell and nonlinear interwell behavior. For higher excitation levels, the system reaches chaotic behavior, which greatly improves the vibration attenuation performance outside the bandgaps. In the work, the authors applied both the harmonic balance method and the time-domain integration to obtain the results.

Sheng et al. (2021) presented numerical and experimental results of a beam with nonlinear resonator attachments. The nonlinear resonator unit cell consists of a complex arrangement of a Duffing oscillator, a flexural resonator, and a vibro-impact resonator. The results show significant vibration attenuation enhancement, especially under conditions resulting in chaotic behavior. Different variations in the system's parameters are studied to assess the impact on the final attenuation performance. Another interesting conclusion is the increasing attenuation rate with increased excitation amplitude, which is a direct consequence of the introduced nonlinearities.

Boechler, Theocharis & Daraio (2011) presented an experimentally verified concept of acoustic rectifiers that use bifurcation to quasiperiodic and chaotic behavior to achieve the desired performance. The sudden nature of bifurcation phenomena allows the system to provide a sharp transition between states, which is a desirable aspect of these devices and otherwise unachievable with other mechanical setups.

Narisetti, Leamy & Ruzzene (2010) developed a perturbation approach for predicting wave propagation in weakly nonlinear periodic chains, and the article has become one of the most cited in the field of nonlinear periodic structures. The simplified perturbation approach enables the authors to develop dispersion relations for the nonlinear systems and estimate the amplitude dependent dispersion properties. The results are validated by numerical simulations and can be used to obtain useful estimations of the amplitude dependent properties of other weakly nonlinear systems. Manktelow et al. (2013) applied this perturbation approach to a nonlinear two-dimensional periodic structure.

Nadkarni, Daraio & Kochmann (2014) developed an analytical study of a periodic one-dimensional chain of bi-stable elements and evaluated its dynamics. Three main regions of behavior were identified and described. The first region, with small response amplitudes, has linear-like wave propagation behavior. At moderate and large amplitudes, the dynamic response becomes richer and solitary waves arise along the system. The analytical solutions are compared with the numerical results in good agreement.

Fang et al. (FANG et al., 2017) have shown numerically and experimentally the existence of ultra-broad-band nonlinear metamaterials in beams and plates induced by chaotic response. Evenly attached nonlinear Duffing oscillators were based on nonlinear force between permanent magnets and internal collisions, constructed columniform magnets and strut and a bolt. The elastic energy is shown to be distributed from a harmonic input to a broadband chaotic response, which is known as energy dispersion (FANG et al., 2016).

Hwang & Arrieta (2021) assess a bistable structure capable of achieving extreme broadband frequency conversion. Their research includes an examination of the frequency characteristics associated with chaotic behavior.

The concept of Nonlinear Energy Sinks (NES) (SAEED; NASAR; AL-SHUDEIFAT, 2023; DING; CHEN, 2020) has been frequently applied as unit cells of nonlinear periodic structures, with extreme attenuation bandwidth widening results (MOSQUERA-SÁNCHEZ; De Marqui, 2024; XIA; RUZZENE; ERTURK, 2019; XIA; RUZZENE; ERTURK, 2020).

2.1.6 Tunability and control

Most of the works exploring the control and tunability of periodic structures use piezoelectric systems to profit from their easily tunable properties. Purely mechanical systems usually have more predefined characteristics of mass and stiffness. However, a few works have used shape memory alloys (SMAs) to obtain some level of control over a purely mechanical periodic structure.

One of the first and most influential works on the active control of periodic structures was developed by Baz (2001). In the author's study, they describe the governing theory and numerical simulations of systems with active piezoelectric actuators that induce periodicity breaks in the system's properties to obtain the Localization effect when and where needed to obtain the desired wave propagation effects.

Sousa et al. (2018) presents the simulations and experimental validation of a beam with SMA resonators. They reported an increase of up to 15% in vibration attenuation bandwidth and estimated a potential shift of 70% in the bandgap frequency for other SMA reported in the literature.

Anigbogu & Bardaweel (2020) developed numerical and experimental investigations of a magnetomechanical metamaterial for simultaneous vibration attenuation and energy harvesting. The developed structures had two separate bandgaps, one of them with significantly higher levels of vibration attenuation. The results for electric power generation showed that the vibration attenuation level and the power generation level were coupled, with the deepest bandgap region generating up to $5.2\mu W$. According to the authors, these results represent a significant improvement compared to other systems available in the literature.

2.2 Rotordynamics

The dynamics of rotating structures is a widely explored problem in the research literature. The historical and foundational work that defines this type of system is described in more detail in Section 3.2. However, the exploration of periodic rotating structures is not so common, with relatively few works available in the literature.

The work of Chatelet, Lornage & Jacquet-Richardet (2002) presents the analysis of a composite shaft with a rotationally periodic flexible disk mounted on one of its ends. The authors propose a finite element method to build a three-dimensional model of this system and elaborate on some of the results and its interpretation. The work of Brandão et al. (2017) presents an analysis of a rotor with periodically spaced flexible blades, exploring the nonlinear interactions between rotor and stator. The stator is considered as a flexible two-dimensional shell structure, and the contact interactions between the shell and rotor blades give rise to modal interaction phenomena. However, both works, as well as the majority of similar literature, do not delve into vibration attenuation aspects, bandgap formation, or wave propagation phenomena of these systems.

One of the few available works exploring the wave propagation properties of rotating structures has been published by Chan, Stephen & Reid (2005), in which they develop an analytical study showing the polarization of forward and backward whirl waves and its speed-dependent dispersion properties. Another interesting work presented by Rosso, Bonisoli & Bruzzone (2019a) proposed an arrangement of resonators attached to a disk that might be a feasible solution for the implementation of such elements in rotating machinery.

The works of Lamas and Nicoletti (LAMAS; NICOLETTI, 2022c; LAMAS; NICOLETTI, 2022b; LAMAS; NICOLETTI, 2022a; LAMAS; NICOLETTI, 2024) also describe the mechanisms of bandgap formation in rotors with longitudinal inertia periodicity, with experimental validation. The concept is especially interesting considering that industrial multistage turbomachinery often has similar periodic arrangements by design.

Attarzadeh et al. (2019) have shown the mechanism of non-reciprocal waves caused by the gyroscopic effects of embedded rotating elements, called gyric metamaterial. This setup allows for the tuning of the inertia properties along the metastructure by spinning the embedded elements without affecting the local stiffness. Alsafar et al. (ALSAFFAR; SASSI; BAZ, 2018) have investigated the stop band created by periodic inserts in drill strings at different rotational speeds. The backward and forward modes and the corresponding bandgaps are shown to be affected differently. Yang et al. (YANG et al., 2019) investigated numerical aspects of the modal and spatial discretisation of spinning beams with distributed rigid gyroscopes. Rosso, Bonisoli & Bruzzone (2019b) proposed the possibility of expanding the concept of metamaterial-based vibration attenuation to an axisymmetric component attached to a rotor.

In a recent work, Xu et al. (2023) presented an analytical model of a nonlinear rotor metastructure. Strong and weak geometrical nonlinearities are explored. The analytical model is compared with the numerical results and an evaluation of the dispersion curves is presented.

Even though the above-mentioned research does not directly explore these aspects from a rotor vibration control perspective, this is certainly one of the most widely explored and prolific fields in Rotordynamics, being one of the most critical aspects in industrial rotating machinery design. Typical methods for controlling vibration in such systems consist of different ways of manipulating and maximizing the damping acting upon the rotor. With the increasing industry demand for more compact, efficient, environmentally friendly, and power intensive systems, the challenges of designing reliable machines that meet these extreme requirements are pushing the boundaries of current vibration control technology. Furthermore, most industrial machines rely on fluid-film bearings as the primary damping source (BENTLY, 2002), especially for high-speed and high-flow centrifugal compressors.

Current industry needs require rotors with higher energy density, smaller diameters, and higher rotation speeds, which can render current bearing technology insufficient to provide the appropriate amount of damping to systems. Insufficient damping and stiffness characteristics in bearings have been listed as one of the main gaps to be surpassed for the design of oil-free machines for future power generation applications (DELLACORTE; BRUCKNER, 2011). Although damping enhancement technologies such as squeeze film dampers have been reliably applied in the industry for decades (MOHAN; HAHN, 1974), the challenge of vibration control for these recent extreme applications is still an open issue.

The Texas A&M University Turbomachinery Laboratory proposed a profoundly innovative concept (DELGADO; ERTAS, 2019; GARY; ERTAS, 2020; ERTAS, 2019; ERTAS; DELGADO, 2019; ERTAS; GARY, 2021) consisting of a hermetically sealed 3-D printed squeeze film damper design that could contribute to overcoming such challenges.

Actively-controlled bearings are also largely explored as a possible solution for improved damping performance, which have shown very promising results. Santos (2018) provides a comprehensive overview of all the different strategies and types of control solutions applied to bearings for vibration attenuation. Different concepts of controllable bearing designs have been proposed, with strategies such as hybrid lubrication bearings, in which the hydrodynamic component of the lubrication is combined with a controllable hydrostatic element (JENSEN; SANTOS, 2022; MOROSI; SANTOS, 2011; PIERART; SANTOS, 2016), and bearings with controllable geometry (CHASALEVRIS; DOHNAL, 2016; KRODKIEWSKI; SUN, 1998).

Naturally, these recent research efforts are concentrated on bearing design solutions. As mentioned above, these components are the primary source of damping for most rotors. This thesis proposes an alternative to this path, proposing a gyroscopic metastructure for vibration attenuation in rotors.

2.3 Final remarks

This chapter presented the main trends of research on mechanical metastructures and rotordynamics in the last 20 years. Although each field has matured independently, their convergence represents an unexplored frontier with significant potential to address current limitations in rotating machinery vibration control. The review shows increasing interest in the application of metastructures for vibration attenuation purposes, and more recently, the investigation of nonlinear systems to achieve enhanced, amplitude-dependent vibration suppression.

The identified gap is particularly relevant given the industry's push toward higher-speed, more compact rotating machinery, where conventional damping solutions are reaching their limits. This thesis addresses this gap by developing the theoretical foundations for gyroscopic nonlinear metastructures.

Studies on system characterization are extremely important to help all other research efforts better understand the observed behaviors and even guide the improvement of current designs. Lately, the use of property variability and periodicity breaks in *quasi*-periodic structures has been a strong motivation for bandgap performance enhancement. Large-scale seismic resonators seem to be a viable option for earthquake protection as they are receiving increasing attention from the scientific community. Non-reciprocal wave propagation has been found as a result of several different topological configurations of metastructures and can be an interesting way to control and guide wave propagation as desired.

There are significant research gaps in the area of nonlinear metastructures. None of those particular phenomena mentioned above has been thoroughly investigated for nonlinear systems, for which the investigations tend to focus only on bandgap performance and the characterization of amplitude dependent properties. There is significant ground to be covered on applying the types of nonlinearities known to generate good bandgap performance to some of the linear configurations described in this article.

On the other side of the spectrum we find rotordynamics. This field has a prolific research environment, but its intersection with the world of the above-mentioned subjects of metastructures and vibration attenuation is still barely explored. This shows a clearly promising new avenue towards the solutions for some of the most pressing challenges in contemporary aspects of turbomachinery design.

The following chapters of this thesis are organized to progressively deepen the understanding of gyroscopic nonlinear metastructures as an alternative strategy to address these challenges. This step-by-step exploration will allow for a gradual understanding of the novel aspects and characteristics of such systems. Figure 2.1 shows a diagram with a visual representation of the thesis structure and the subjects it progressively explores in each chapter.

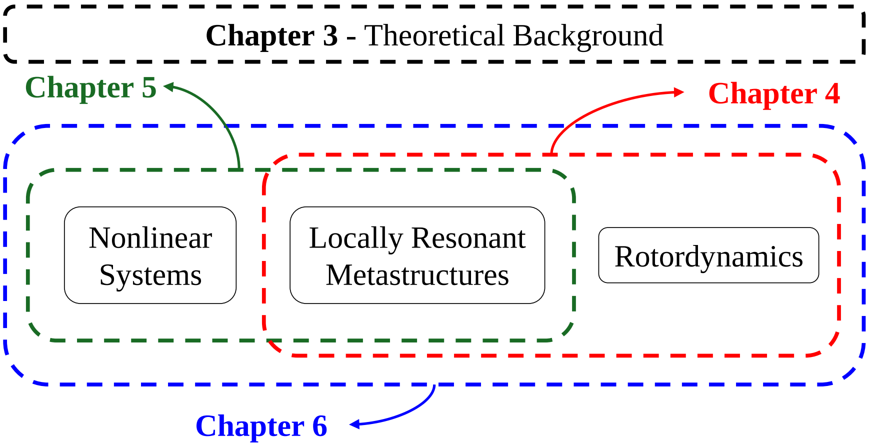

Figure 2.1 – Organization of the following chapters.

3 Theoretical Background

3.1 Metastructures for Vibration Attenuation

A good way to start the study of metastructures and its vibration attenuation capabilities is to investigate the dynamics of the well-known arrangement known as Dynamic Vibration Absorbers (DVAs). DVAs, also known as Vibration Neutralizers or Tuned Mass Dampers, were first introduced by Hermann Frahm in 1909 and had their dynamics described with mathematical rigor two decades later by Ormondroyd (1928). Since then, it has been used in numerous engineering applications: from Stockbridge dampers for vibration control in overhead power transmission lines to earthquake protection in sky-scrappers and vibration reduction in large bridges. A good description and overview of this kind of device is also provided by Steffen & Rade (2001).

Some fundamental aspects of DVAs' attenuation mechanisms are explored here to provide an intuitive and mathematical base of understanding that will later be helpful for the description of vibration attenuation phenomena in mechanical metastructures.

Starting from the classic spring-mass damper model, as shown in Figure 3.1a, we can describe its equation of motion and response amplitude to harmonic excitation, respectively, as

$$m\ddot{x}(t) + c\dot{x}(t) + kx(t) = F_0 e^{j\omega t} \quad \text{and} \tag{3.1}$$

$$x(t) = \frac{F_0}{-\omega^2 m + jc\omega + k} e^{j\omega t + \phi}, \tag{3.2}$$

where ω is the excitation frequency, F_0 is the excitation amplitude, ϕ the response phase angle, and $j = \sqrt{-1}$.

The arrangement proposed in Figure 3.1b, on the other hand, has 2 degrees of freedom. The attachment - or *resonator* - with mass m_r and stiffness and damping k_r and c_r, respectively, can be regarded as a DVA tuned to the frequency of $\omega_r = \sqrt{\frac{k_r}{m_r}}$. To understand the dynamic behavior of this system, let us consider that a harmonic excitation is applied only on the base structure, i.e. on the mass m, and its own response is of interest. This assumption is consistent with practical applications, in which we intend to neutralize the vibration of a base structure that is subjected to a specific dynamic excitation. The system's equation of motion can be described as the system of second-order differential equations

$$\begin{bmatrix} m & 0 \\ 0 & m_r \end{bmatrix} \begin{Bmatrix} \ddot{x} \\ \ddot{x}_r \end{Bmatrix} + \begin{bmatrix} c + c_r & -c_r \\ -c_r & c_r \end{bmatrix} \begin{Bmatrix} \dot{x} \\ \dot{x}_r \end{Bmatrix} + \begin{bmatrix} k + k_r & -k_r \\ -k_r & k_r \end{bmatrix} \begin{Bmatrix} x \\ x_r \end{Bmatrix} = \begin{Bmatrix} F_0 e^{j\omega t} \\ 0 \end{Bmatrix}. \tag{3.3}$$

Assuming the a harmonic steady state response in the form

$$\mathbf{x} = \begin{Bmatrix} x \\ x_r \end{Bmatrix} = \begin{Bmatrix} X_0 \\ X_{r0} \end{Bmatrix} e^{j\omega t}, \tag{3.4}$$

where X_0 and X_{r0} are the complex response amplitudes of the base and resonator masses, respectively, we can rewrite Eq. 3.3 as

$$\mathbf{Z} \begin{Bmatrix} X_0 \\ X_{r0} \end{Bmatrix} = \begin{Bmatrix} F_0 \\ 0 \end{Bmatrix}, \tag{3.5}$$

where $\mathbf{Z}$ is the impedance matrix defined as

$$\mathbf{Z} = \begin{bmatrix} Z_{11} & Z_{12} \\ Z_{21} & Z_{22} \end{bmatrix} = \begin{bmatrix} -\omega^2 m + j\omega(c + c_r) + k + k_r & -j\omega c_r - k_r \\ -j\omega c_r - k_r & -\omega^2 m_r + j\omega c_r + k_r \end{bmatrix} \quad \text{with} \tag{3.6}$$

$$\mathbf{Z}^{-1} = \frac{1}{Z_{11} Z_{22} - Z_{12} Z_{21}} \begin{bmatrix} Z_{22} & -Z_{12} \\ -Z_{21} & Z_{11} \end{bmatrix}. \tag{3.7}$$

We can then easily obtain the base mass' response amplitude X_0 to the harmonic excitation as

$$X_0 = \frac{Z_{22} F_0}{Z_{11} Z_{22} - Z_{12}^2}. \tag{3.8}$$

The FRF shown in Figure 3.2 presents the fundamental characteristics of the DVA vibration attenuation phenomenon. The phase plot shows the phase between displacements of base mass and DVA.

Two fundamental aspects are easily observed in Figure 3.2. First, the base mass response is greatly neutralized around the frequency to which the DVA is tuned, while two other amplification peaks, usually referred to as *side frequencies* or *side modes*, appear on both sides. The second aspect is that there is a phase shift 180 ° between the base structure and the DVA as the excitation frequency crosses the maximum attenuation range. This phase shift is fundamental for understanding the attenuation mechanism of the DVA. Let us now investigate the phase relationships between the elastic link force of k_r over the

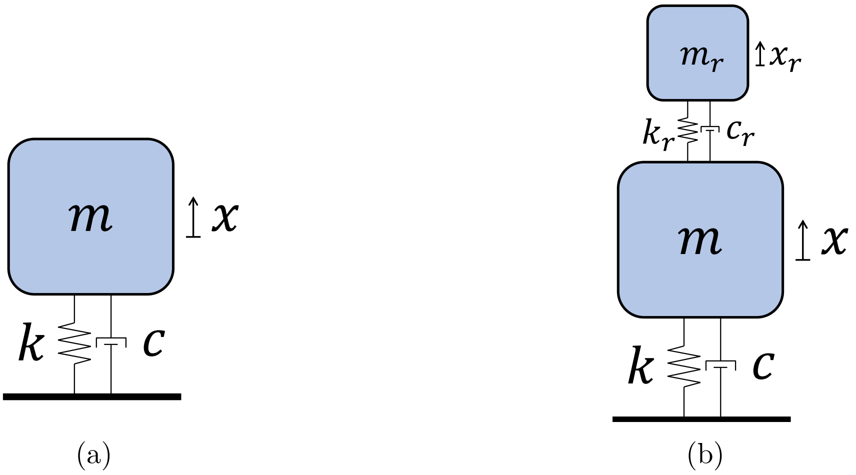

Figure 3.1 – Basic 1 DoF arrangement (a) and simple DVA system (b).

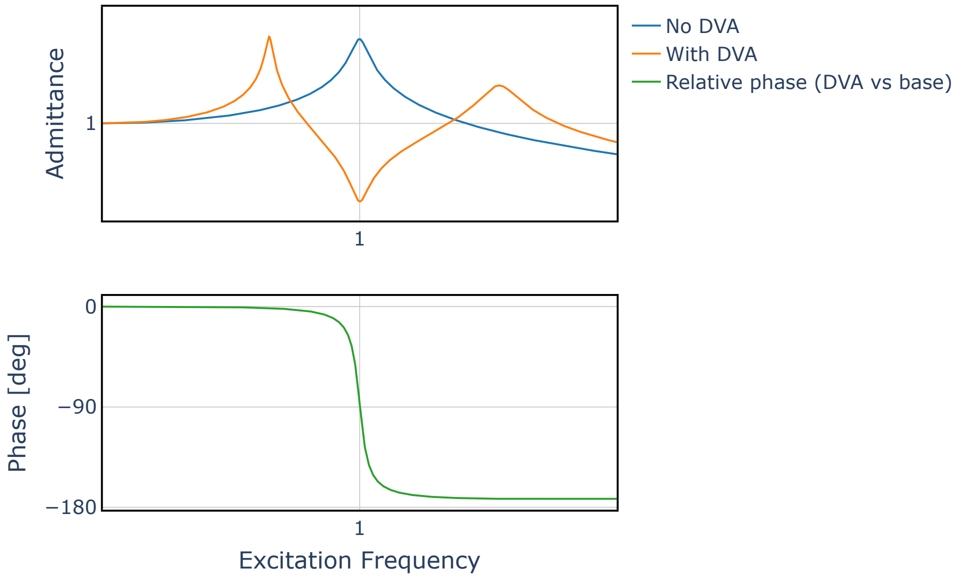

Figure 3.2 – Frequency Response Functions and phase of a base 1DoF system with and without DVA.

base mass m and the velocity of this mass'. The plots in Figure 3.3 show these relations, revealing that exactly at the tuned frequency of 1 rad/s, the elastic force and the velocity of the base mass are perfectly out of phase, with a phase difference of 180 °. This indicates that the effect of the DVA's movement is always creating an opposing force for the base mass vibration, which ultimately creates the attenuation effect. This shows that the phase shift shown in Figure 3.2 is essentially what causes the DVA attenuation effect.

The same concept explained above has been expanded for application in numerous systems, greatly varying in scale and overall complexity. An interesting application was proposed by Ribeiro, Pereira & Alberto Bavastri (2015), where a non linear DVA-like structure is used as an attachment for the rotor bearings. The DVAs were connected to the bearing housing with a viscoelastic material, generating significant vibration attenuation.

Expanding the concept even further and drawing inspiration from recent advancements in Quantum Physics, novel explorations into periodic topological arrangements start

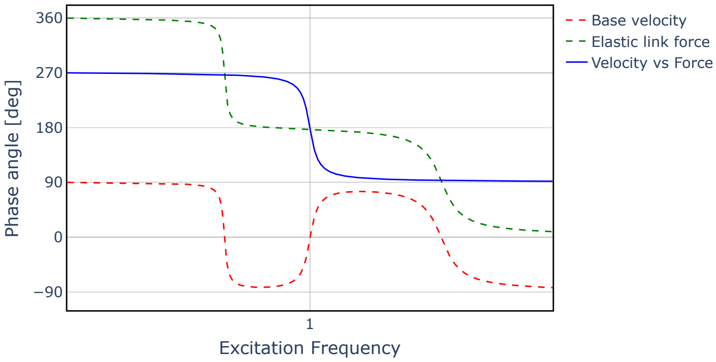

Figure 3.3 – Phase relationships between elastic link force and base mass velocity.

to emerge. The area of wave propagation was the first to take advantage of the particular characteristics of periodic mechanical structures. In 1946, Brillouin (1946) published what is still one of the main references for the study of wave propagation in periodic structures. A vast range of peculiar dynamic behavior emerge from this type of system, such as negative mass and stiffness effects, wave guide capabilities, and non-reciprocal wave propagation. However, one specific characteristic is of special interest for the study of mechanical periodic structures (or mechanical metastructures): the *bandgap* phenomenon.

As a general definition, bandgap can be understood as a particular frequency in the range in which wave propagation is a specific structure is impossible, or strongly attenuated. From a mathematical perspective, we can say that the bandgap occurs at a particular frequency range in which the resulting wave number has a complex component that causes its amplitude to decay in the direction of propagation.

To illustrate the bandgap phenomenon and its two main formation mechanisms, let us consider the simplified system illustrated in Figure 3.4.

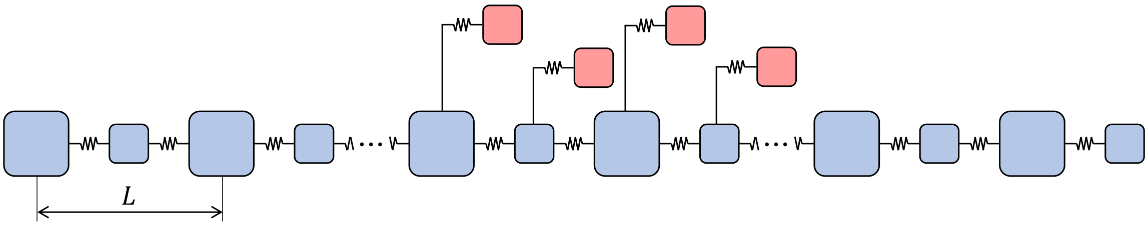

Figure 3.4 – Simplified periodic chain with 2-cell periodicity and resonators attachments.

The elements represented in blue are referred to as base structure, and the ones in red are henceforth called resonators. Note that the base structure has a periodic configuration, in which it repeats every 2 elements, or two cells. Each set of 2 cells that repeat along the base structure can be called a *unit cell*, and this periodic characteristic is the source of a very particular ind of bandgap.

Each unit cell can be regarded as a *scatterer* if we consider the standpoint of wave propagation across the base structure. This means that a mechanical wave incident on a unit cell will be scattered - or reflected - because of the sudden change in mechanical impedance of the propagation medium.

If we assume that a particular condition is possible in which the complete destructive interference of scattered and incident waves takes place, this would lead to no wave propagation for this condition. The total destructive interference of superimposing waves of the same amplitude occurs when their relative phase is of 180°. Two adjacent unit cells will scatter waves with a spatial offset of $\Delta x = L$, where L is the length of each unit cell. Thus, the waves scattered by two adjacent unit cells will interfere destructively if

$$L = \lambda/2, \tag{3.9}$$

where λ is the wavelength of a particular propagating wave. Given the direct relation between wavelength and frequency of a particular wave, given by the medium's dispersion curve, we can say that the frequency related to the wavelength λ cannot generate wave propagation in this medium.

The condition presented in Eq. 3.9 is known as Bragg condition, and the bandgap effect that emerges when this condition is satisfied is called *Bragg Scattering* bandgap. The Bragg Scattering bandgap phenomenon is caused by the destructive interference of waves scattered from periodically arranged scatterers (DEYMIER, 2013).

This type of bandgap formation mechanism, however, poses an important obstacle for many practical vibration attenuation applications: *scale*. In mechanical systems, the Bragg Condition is usually satisfied only in very high frequency ranges or very large unit cells. This might not be a problem for acoustic systems that are often subjected to high frequencies - $f > 1000$ Hz -, but can be quite impractical for smaller, lighter structures subjected to lower frequency excitation.

A clever way to overcome this obstacle and enable low frequency bandgaps for vibration attenuation is the use of locally resonant periodic structures. Several works can be found exploring this kind of strategy to achieve effective low frequency vibration attenuation in structures with more feasible scale (LAZAROV; JENSEN, 2007; MATLACK et al., 2016; ELMADIH et al., 2019; BARAVELLI; RUZZENE, 2013).

The type of bandgap formation mechanism is known as *Locally Resonant* bandgap, and its basic phenomenology is quite similar to that of the DVA, which was presented earlier in this chapter. The opposing force generated by the relative motion between the resonating cell and the base structure creates an obstacle for the wave propagation, thus strongly reducing the systems transmissibility across the locally resonant array.

The resonators illustrated in red in Figure 3.4 are a very simple way of generating this locally resonant effect. The main advantage of this arrangement is that it allows the bandgap to be tuned to any frequency virtually, arbitrarily low, or high.

The work published by Sugino et al. (2017) presents a general theory for bandgap estimation in locally resonant metastructures. In this work, the effect of variation of two fundamental parameters of such structures is explored: (1) the number of resonators S and

(2) total mass ratio μ between resonators and base structure. This work is fundamental for understanding how finite resonator arrays affect vibration attenuation performance and it is instrumental for the design of such structures.

The authors show that for a large number of resonators, a locally resonant bandgap is formed at frequencies ω such that

$$\omega_t < \omega < \omega_t\sqrt{1+\mu}, \tag{3.10}$$

where ω_t is the target frequency, which is defined by the natural frequency related to the locally resonant structures - or resonators. The results of Sugino et al. (2017) show that a finite number of resonators is capable of producing a bandgap with a frequency span close to, and even wider than, that of Eq. 3.10. The definition of the optimal number of resonators to maximize the bandgap width depends on the system's parameters, especially the target frequency and the resonator mass ratio.

The frequency response function in Figure 3.5 shows the transmissibility of a structure like that of Figure 3.4, with and without the attached resonators. It is interesting to notice that the Bragg Scattering bandgap occurs for both cases, while the locally resonant bandgap only appears when the resonators are added. It is important to remember that, although not shown in this example, the periodicity of the attachments can itself also create a Bragg type bandgap.

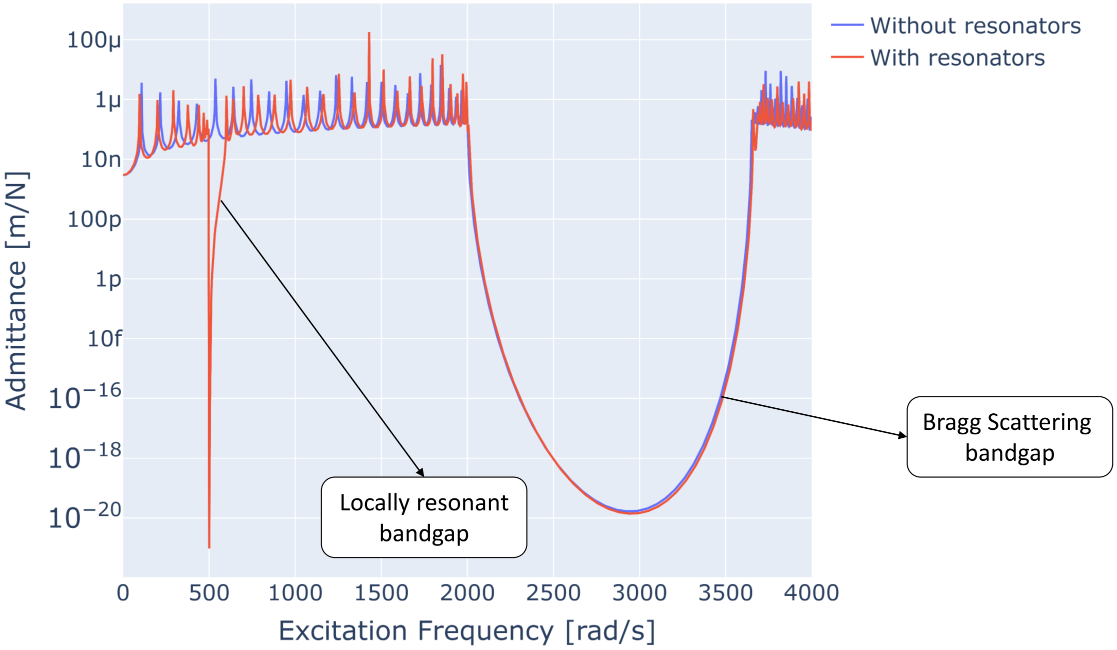

Figure 3.5 – Frequency response function showing Bragg Scattering and Locally Resonant bandgaps.

From the perspective of the mechanical metastructure design, it is clear that locally resonant bandgaps have the potential to be much more versatile. It is tunable to virtually any desired frequency and can provide strong effective attenuation. However, a downside is also easily observed from Figure 3.5: its bandwidth tends to be generally narrower than that of Bragg bandgaps.

There are several strategies that can lead to the broadening of locally resonant bandgaps. One of them was already mentioned and described by Eq. 3.10, and is achieved by increasing the mass ratio μ. In practical applications, however, we cannot indefinitely increase this ratio, since the ideal design will always seek the minimization of the added mass to resonators. One strategy of increasing the locally resonant bandgap bandwidth is of particular interest for this works: resonator variability - also known as functionally graded or *rainbow* metastructures.

A great number of works have been published exploring the first concept, i.e. the idea of breaking the periodicity of the attachments or locally resonant structures in order to obtain wider bandgaps. The concept is a way of spreading the vibration attenuation effect across the different resonating cells, each tuned to a slightly different frequency. In this way, the attenuation of different frequencies is spatially distributed across the structure, hence the reference to the effect of a *rainbow*, in which a spatial distribution of slightly different frequencies is also observed. This leads to a superposition of many smaller slightly offset bandgaps into a single, wider bandgap.

Figure 3.6 shows the same chain system used in the figures above, but now with the widening effect of resonators mass variability. In both cases, the mass ratio μ was kept the same and a 30% mass gradation was imposed on the resonating attachments. The bandgap is significantly widened, while the vibration attenuation performance - bandgap depth - is slightly worse.

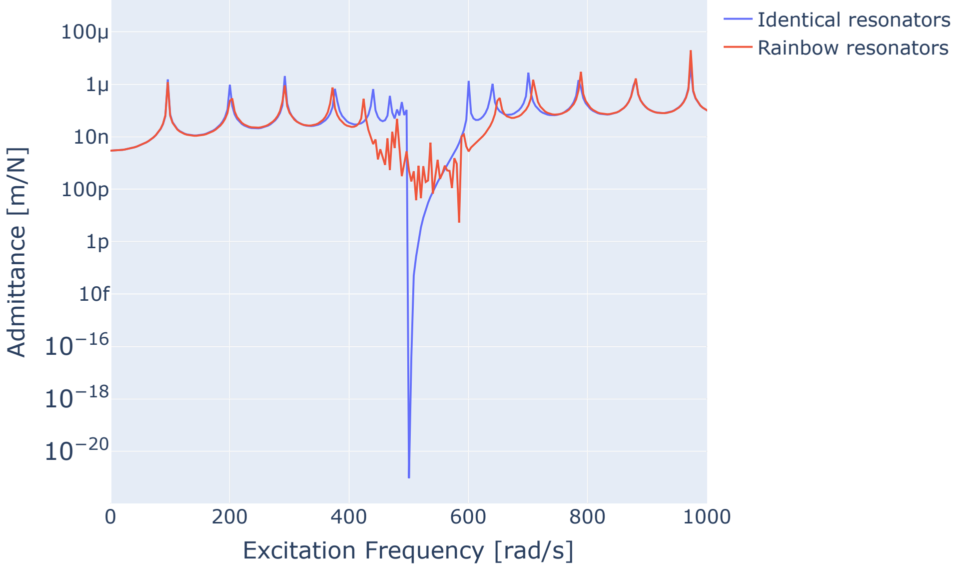

Figure 3.6 – Bandgap widening with rainbow resonators.

Several other developments seek to maximize the widening effects created by the resonator variability. An especially interesting strategy is presented by Fabro, Meng &

Chronopoulos (2021), in which a correlated disorder in the resonating cells' properties provided a significant increase in bandgap formation and overall vibration attenuation performance. This indicates that the natural variability generated by fabrication processes of these structures may incur in improved vibration attenuation behavior of the resulting system.

3.2 Rotordynamics

The interest in the study of rotors has been present since the invention of the wheel, and with increasing comprehensiveness and depth. With the invention of the steam engines and other types of high energy rotating machinery on the 18th century, a deeper understanding of the characteristics of rotors and the underlying phenomena determining their behavior became an absolute necessity for further technological development. With such development, the ability of rotor systems to transmit power and store huge amounts of energy in a reduced volume started to be explored. Higher energy led to higher speeds, higher masses, higher loads, and, unavoidably, bigger problems.

A rotor is always used as an intermediary. It is designed as an energy path through which the power will be guided from a source to a desired destination. Like an energy "pipeline". However, in all practical applications, this pipeline will have **"energy leaks"**. These leaks transform part of the stored rotational energy into other forms of mechanical energy that were not originally intended by design. One of the most harmful forms of mechanical energy fed by this energy leak mechanism is vibration, which can be divided into *lateral*, *torsional*, and *axial* modes. From these, the lateral modes of the rotor are of greatest concern (MUSZYNSKA, 2005), since they frequently are the lowest frequency modes, easily excited and with great damage potential. Torsional modes can often be quite harmful to rotating machinery. Their dynamics, however, are much simpler in most cases, yielding simpler, more representative models and with simpler problem-solving resources.

The technological demand has always been for higher energy intensity applications, i.e. bigger amounts of energy in reduced volumes. From a design perspective, the strength requirements in rotating machinery are usually related to the maximum torque. And, since power transmission in these systems happens through rotational motion, the inverse relationship between speed and torque led to the need for higher and higher rotational speeds. This trend leads directly to higher energy leaks and to the intensification of the problems associated with it. For these reasons, the study of ***rotordynamics*** has witnessed continuous research development and scientific production over the centuries.

The first scientific interest in the dynamics of rotating systems was recorded by Rankine's paper (RANKINE, 1869), in which an experimental approach was presented. The conclusions of Rankine's paper were, however, refuted by the first study that mathematically described a rotor system with mathematical rigor, which was presented by Jeffcott (1919).

Filippov (1895) presented a similar, but simpler, system years earlier.

In that work, Jeffcott (1919) presents the simple problem of an unbalanced, isotropic rotor supported by rigid bearings. From that, the author derives fundamental descriptions of a rotor system's behavior, introducing the notions of critical speed, high spot, heavy spot, and phase angle.

To begin understanding the particularities of rotating systems' dynamics, let us investigate a simple 2 DoF system that can be regarded as a rough representation of an isotropic rotor consisting of a slender, flexible shaft supported by rigid bearings and with a rigid disk attached at its mid span, as depicted in Figure 3.7. This system is explored by Muszynska (2005) in what the author calls a *modal approach*.

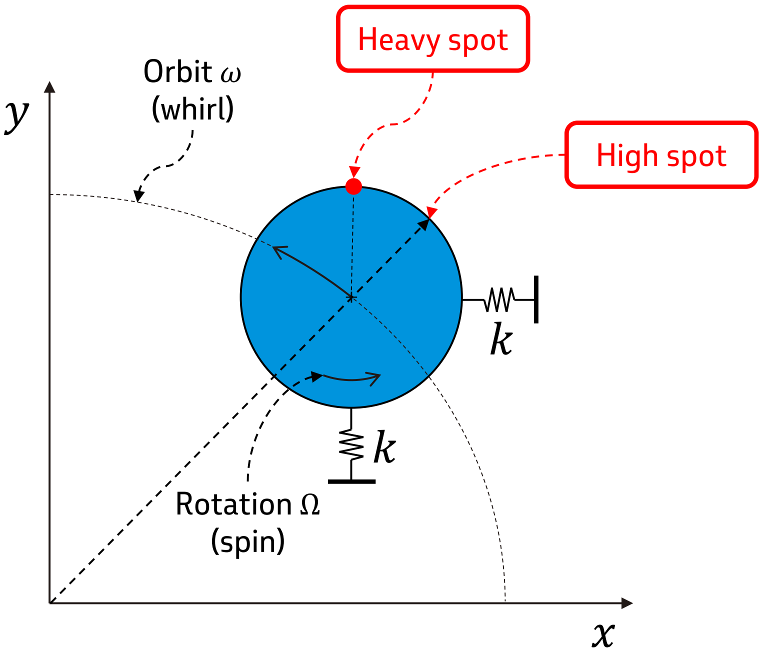

Figure 3.7 – Two degrees of freedom rotor model.

This model bears very little similarity to any real rotating machinery. However, it can help to describe the fundamental principles of rotordynamics in an easy and clear way. The system's formulation uses the x and y coordinates in a *modal sense*, as being the modal components of the first rotor natural mode having a frequency much lower than all other natural frequencies. Since we consider an isotropic system, these two orthogonal modal coordinates can be reduced to one *complex mode*.

If we consider an external excitation force having a rotating character, amplitude F and frequency ω, we can describe the system's motion as the set of non-homogeneous differential equations:

$$M\ddot{x} + C\dot{x} + Kx = F\cos\omega t + \delta, \tag{3.11}$$

$$M\ddot{y} + C\dot{y} + Ky = F\sin\omega t + \delta, \tag{3.12}$$

where M, C and K represent the mass, damping, and stiffness of the system and δ is the excitation phase angle.

In this case, the equations are uncoupled, which means that the system's response in each one of the two orthogonal directions will be represented by a sinusoidal waveform. Note that we can eliminate the time from the system's response representation by observing the x vs y behavior: this is called an *orbit plot* and it is illustrated in Figure 3.8.

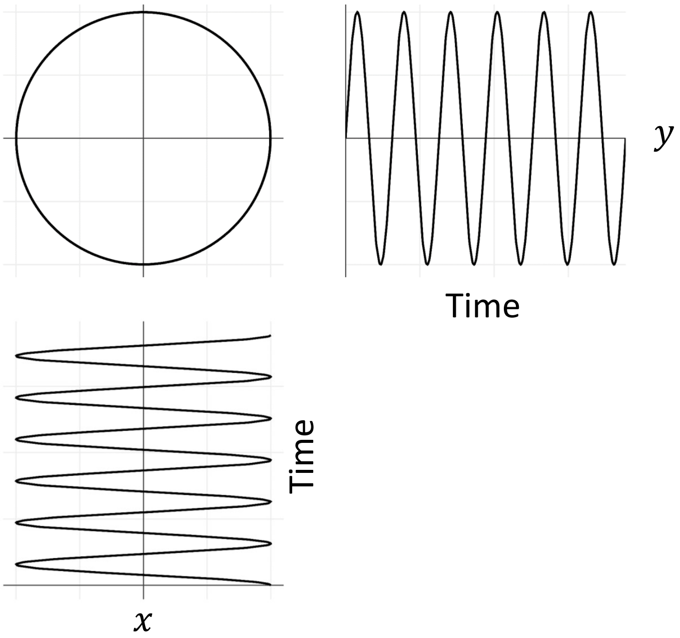

Figure 3.8 – Orbit representation as the composition of two orthogonal coordinates.

The rotor orbit, also sometimes referred to as rotor *whirl*, is the representation of the actual path of the rotor centerline, and the time remains only a parameter with which the direction of the orbit can be determined. By evaluating the path of the orbit as time progresses, it can be observed that the path can describe either a clockwise or a counter-clockwise orbit. Note that this provides no information on the rotor rotation and its direction. If, however, the rotation direction is previously known, the orbit path direction can be compared to it to determine if they are in the same direction, which is called a *forward* whirl, or in opposite directions, or *backward* whirl.

The system's equations of motion (Eqs. 3.11 and 3.12) are uncoupled and can easily be transformed by combining x and y coordinates in a new coordinate system defined by the two complex conjugate variables

$$z = \frac{x + jy}{2} \quad \text{and} \tag{3.13}$$

$$z^* = \frac{x - jy}{2}, \tag{3.14}$$

where the division by two is included to maintain unit consistency between both equations. Multiplying Eq. 3.12 by $j = \sqrt{-1}$ and then adding it to and subtracting it from Eq. 3.11 we easily obtain a new set of motion equations as

$$M\ddot{z} + C\dot{z} + Kz = \frac{F}{2}e^{j(\omega t + \delta)}, \tag{3.15}$$

$$M\ddot{z}^* + C\dot{z}^* + Kz^* = \frac{F}{2}e^{-j(\omega t + \delta)}. \tag{3.16}$$

The new set of equations is not only also decoupled, but it is also almost identical to the original one. These two can be referred to as *forward* mode and *backward* mode equations (MUSZYNSKA, 2005). This understanding is essential for understanding both the dynamics and the analyses of more complex rotor systems.

We should note that the expression presented in Equation 3.14 represents the backward *component*, not the *vector*. To obtain the complex representation of the backward rotating vector that forms the full precession orbit of a rotor, one should use the complex conjugate of the backward component $\mathbf{z}_b = \overline{z^*}$ to account for its reverse rotation direction. The forward rotating vector, on the other hand, is numerically identical to the complex representation of its component $\mathbf{z}_f = z$

An even simpler case can be considered where $\omega = \Omega$ and the only excitation source is the unbalance $F = Mr\Omega^2$, where r represents the distance between the rotor's center of mass and the rotation axis. The quantity $U = Mr$ is often referred to as *unbalance magnitude*. In this case, the excitation force will exclusively excite the forward mode and can be described as

$$M\ddot{z} + C\dot{z} + Kz = U\Omega^2 e^{j(\Omega t)}. \tag{3.17}$$

This system, which has become known as Jeffcott Rotor in its most simple representation, refers to the work of Jeffcott (1919).

Two definitions are very useful for both practical and theoretical purposes in the study of rotor systems: the concepts of *high spot* and *heavy spot*, both illustrated in Figure 3.7. The *high spot* is the point on the rotor's surface that is furthest away from its neutral axis, or equilibrium position. The *heavy spot* corresponds to the position of the imbalance if it is considered as an equivalent mass attached to the rotor's surface.

We can also describe the unbalance force in the complex representation that restores the original x and y coordinate system. From Eqs. 3.13 and 3.14 we can infer that $x = z^* + z$ and $y = j(z^* - z)$. With these relations, we can obtain the F^x_{unb} and F^y_{unb} components of a pure unbalance force excitation in complex notation as

$$F^x_{unb} = U\Omega^2 e^{j(\Omega t)} \quad ; \quad F^y_{unb} = -jU\Omega^2 e^{j(\Omega t)} = -jF^x_{unb}. \tag{3.18}$$

The complex representation of the physical entities in x and y coordinates can be very useful for two reasons: (1) it can be more straightforward to apply in the commonly used rotordynamic finite element models, and (2) vibration measurement in real industrial machinery is often conducted in 2 orthogonal directions and represented in terms of amplitude and phase of each, which can easily be translated to the complex notation.

However, to understand the overall behavior of the vibration, it is much simpler to explore the representation of Eq. 3.17, which suggests a solution in the form $z = Ae^{\Omega t+\phi}$, in which A is the vibration amplitude and ϕ is the phase angle. The Bode plots in Figure 3.9 show the behavior of the amplitude and phase angle of this system for different values of the damping factor ζ.

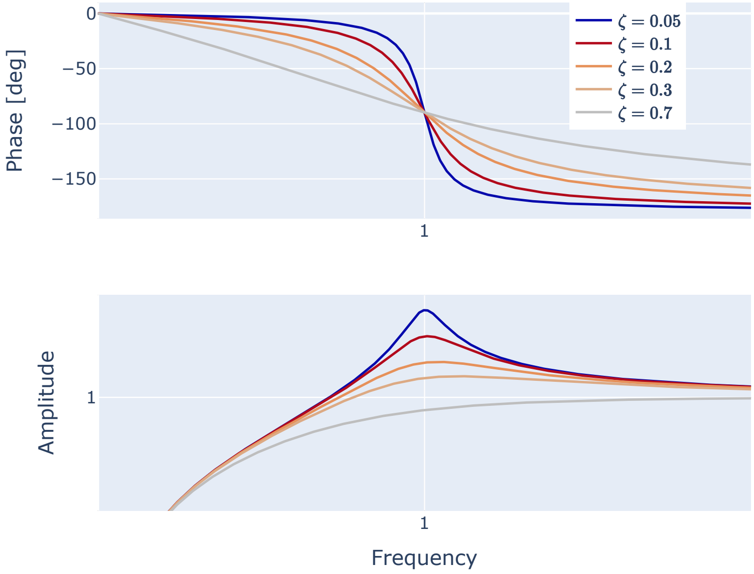

Figure 3.9 – Bode plots of an unbalanced Jeffcott Rotor for different values of damping factor ζ.

This response brings light to the concept of *critical speed*, which corresponds to the rotational speed $\Omega = \Omega_c$ that results in the maximum response amplitude value.

It is also of interest to investigate the amplitude behavior for high frequencies $\Omega >> \Omega_c$. The vibration amplitude is $A = \frac{U\Omega^2}{-M\Omega^2+jC+K}$, from which we can derive that

$$\lim_{\Omega\to\infty} A = \frac{U}{M} = r \tag{3.19}$$

where r is the unbalance offset, as previously defined. In other words, for frequencies much higher than the critical speed, the response amplitude tends to a constant value corresponding to the eccentricity between the rotor's center of rotation and center of mass.

Adding further complexity to our analysis and investigating other fundamental aspects of a rotor system, a simple 4 degrees of freedom system will be explored. The illustration in Figure 3.10 represents this system, which is a more complete representation of the Jeffcott Rotor model.

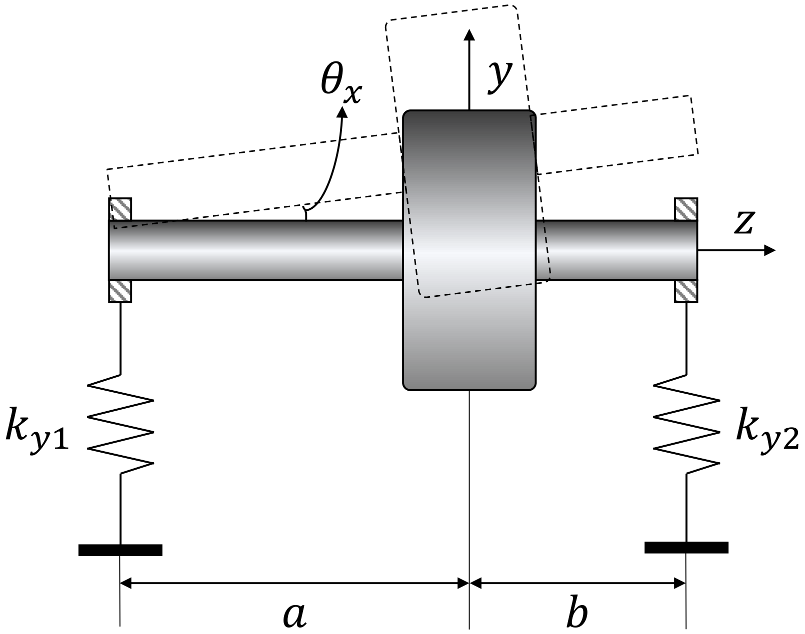

Figure 3.10 – Four degrees of freedom Jeffcott rotor.

This model considers a rigid, massless shaft supported by two elastic bearings represented by springs. The bearings are considered isotropic, i.e. they have the exact same elastic properties in both y and x directions ($k_{y1} = k_{y2} = k_{x1} = k_{x2}$). Attached to the rigid shaft is a rigid disk with mass m, moment of inertia about Oz axis $I_z = I_p$ - referred to as *polar* moment of inertia - and moments of inertia about Ox axes Oy identical $I_x = I_y = I_t$ - referred to as *transverse* moment of inertia. The disk-shaft system is then free to move in x, y, θ_x and θ_y directions, which is used as the system coordinates to derive its equations of motion, while maintaining a fixed angular speed $\dot{\theta}_z = \Omega$ which is referred to as *rotation speed.*

The lateral displacements of the disk's center of mass are considered as the system's x and y coordinates, since the rest of the shaft has no mass. It would also be possible to use the lateral displacements of both shaft ends to derive the system's equations of motion. However, this would be a more complicated way to reach the exact same description of the system's dynamics.

Applying Newton's second law of motion, one can obtain the system's equations of motion as

$$m\ddot{x} = -f_{x1} - f_{x2}, \tag{3.20}$$

$$m\ddot{x} = -f_{y1} - f_{y2}, \tag{3.21}$$

$$I_t\ddot{\theta}_x + I_p\Omega\dot{\theta}_y = -af_{y1} + bf_{y2} \quad \text{and} \tag{3.22}$$

$$I_t\ddot{\theta}_y - I_p\Omega\dot{\theta}_x = af_{x1} - bf_{x2}, \tag{3.23}$$

where f_{x1} denotes the elastic restoring force of the spring k_{x1}, and the other force variables follow the same logic. The components $I_p\Omega\dot{\theta}_x$ and $I_p\Omega\dot{\theta}_y$ correspond to the gyroscopic effects in both directions, and are one of the fundamental characteristics of rotor system dynamics.

The four force components of Eq. 3.23 can be described in terms of the stiffness coefficient and displacement variables as

$$f_{x1} = k_{x1}(x - a\sin(\theta_y)). \tag{3.24}$$

It is therefore clear that the system is intrinsically nonlinear, although rarely considered as such. Assuming that only small displacements take place, we can consider $\sin(\theta_y) \approx \theta_y$. Considering this linearized form for all 4 force components and substituting on the original equations of motion, one can then obtain the final form of the system's equation of motion:

$$m\ddot{x} + (k_{x1} + k_{x2})x + (-ak_{x1} + bk_{x2})\theta_y = 0, \tag{3.25}$$

$$m\ddot{y} + (k_{y1} + k_{y2})y + (ak_{y1} - bk_{y2})\theta_x = 0, \tag{3.26}$$

$$I_t\ddot{\theta}_x + I_p\Omega\dot{\theta}_y + (ak_{y1} - bk_{y2})y + (a^2k_{y1} - b^2k_{y2})\theta_x = 0 \quad \text{and} \tag{3.27}$$

$$I_t\ddot{\theta}_y - I_p\Omega\dot{\theta}_x + (-ak_{x1} + bk_{x2})x + (a^2k_{x1} - b^2k_{x2})\theta_y = 0. \tag{3.28}$$

Taking a closer look at these equations, we can see that there are elastic components that couple the first and fourth equations as well as the second and third equations. Furthermore, the gyroscopic components couple θ_x and θ_y components. Therefore, all equations are coupled and the complete system equation can be represented by

$$[\mathbf{M}]\ddot{\mathbf{x}} + ([\mathbf{C}] + \Omega[\mathbf{G}])\dot{\mathbf{x}} + [\mathbf{K}]\mathbf{x} = 0, \tag{3.29}$$

where [**M**], [**C**] and [**K**] are the mass, damping, and stiffness matrices, respectively. The matrix [**G**] is the gyroscopic matrix that appears multiplied by the shaft rotation speed Ω. Analyzing Eqs. 3.27 and 3.28, one can note that the matrix [**G**] is anti-symmetric. The vector $\mathbf{x}$ represents the displacements and is constructed as $\mathbf{x} = \{x\ y\ \theta_x\ \theta_y\}$.

The solution of Eq. 3.29 leads to an eigenvalue problem, the result of which is dependent on the value of Ω and reveals one of the most singular characteristics of rotor systems. By obtaining the natural frequencies - eigenvalues - of this system for different values of the speed Ω we can build what is commonly known as *Campbell Diagram* (CAMPBELL, 1924). Figure 3.11 shows an example of a Campbell Diagram for a typical Jeffcott rotor similar to that shown in Fig. 3.10, but considering a symmetric arrangement with $a = b$.

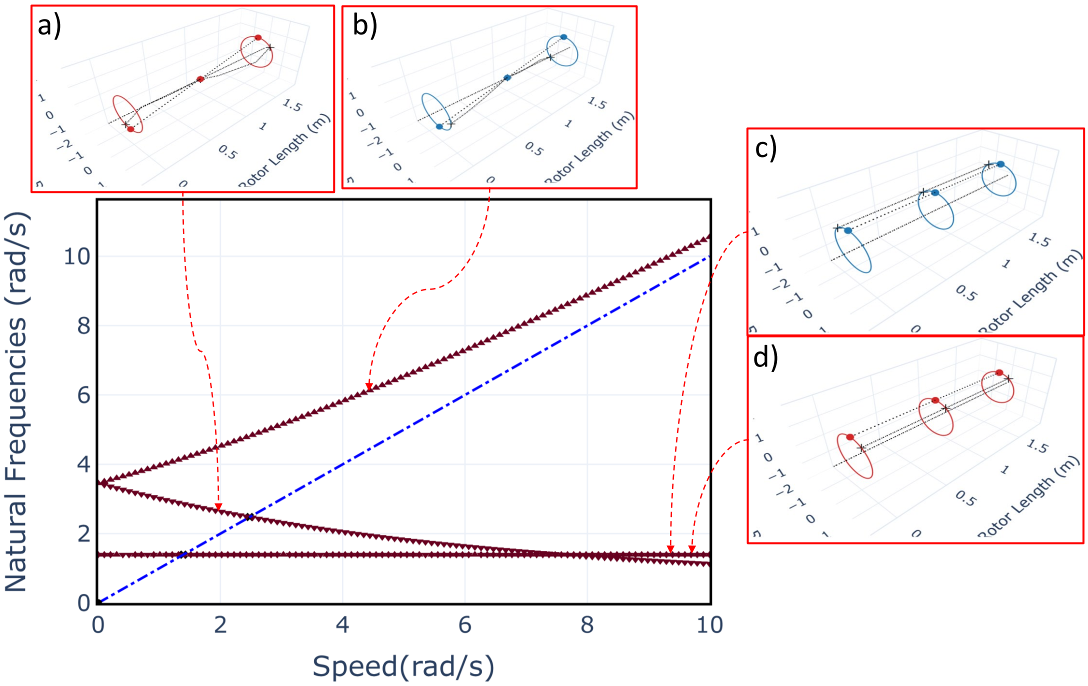

Figure 3.11 – Typical Campbell Diagram and mode shapes for a 4 DoF Jeffcott rotor. (a) Backward conical mode, (b) Forward conical mode, (c) Forward cylindrical mode and (d) Backward cylindrical mode.

Observe that two of the modes seem to be significantly more sensitive to the rotation speed, one of them increasing with speed and the other decreasing, which can be explained by the mode shapes' geometric characteristics. The modes most affected by the gyroscopic effects have a significant *tilt* motion to them, hence being called *conical* modes. The lower modes are dominated by almost purely lateral motion, with little or no tilt, hence being called *cylindrical* modes. Since the gyroscopic effects, present in Eqs. 3.27 and 3.28, are directly related to the θ_x and θ_y components, its effects will only be significant if the motion exhibits significant tilt displacements.

Focusing on another aspect on the same diagram, the mode shapes represented in blue correspond to forward whirl modes, while the red ones represent backward whirl modes. Then we can conclude that the gyroscopic effects introduced by the matrix $[\mathbf{G}]$ increase the value of the forward natural frequencies, and decrease the backward ones.

3.3 Numerical solution of nonlinear differential equations

This section will introduce some of the numerical methods that were employed to obtain the results presented in this thesis. Only less conventional methods will be presented here. The most commonly used methods, such as 4th order Runge-Kutta (RK4), will be omitted for brevity.

3.3.1 The Harmonic Balance Method

The Harmonic Balance Method (HBM) was first proposed and described in 1968 by Bailey in his PhD thesis (BAILY, 1968) as a technique to find steady-state periodic solutions for nonlinear circuit networks. The method proposes a periodic solution for nonlinear differential equations in the form of its Fourier Series. By formulating an error function, an optimization method is applied to find the Fourier coefficients by minimizing the error function.

Since then, many variations of the original method have been proposed and implemented, resulting in increasingly faster and more accurate frameworks. Many of them focus specifically on the application of the methods for nonlinear oscillators, such as Razzak (2016) and Mickens (2001). Other works focus on determining ways to have more accurate solutions even for high amplitude responses and describing methods for optimal truncation of the Fourier Series (HOSEN et al., 2012; ALAM; HAQUE; HOSSAIN, 2007).

A very useful OpenSource tool called Mousai has been developed and made available by Slater (2017). This Python-based software is capable of providing robust Harmonic Balance based results for a generic system given that you have a Python function F capable of providing $F(\mathbf{X}, t) = \dot{\mathbf{X}}$, where $\mathbf{X}$ is the state space vector that defines the studied system, $\dot{\mathbf{X}}$ is the states time derivative and t is time.

Detroux et al. (2015) presents in deep detail a Harmonic Balance framework for Bifurcation Analysis in Nonlinear Mechanical systems, which is quite adequate for the purposes of this thesis. The proposed procedure uses an Alternating Frequency/Time-Domain (AFT) technique to compute the nonlinear forces' harmonic components and build the Harmonic Balance problem. This procedure is used in this thesis and is described in further detail in this chapter.

The construction of the Harmonic Balance Method starts with the definition of the n-DoF system's equations of motion in the time-domain as

$$[\mathbf{M}]\ddot{\mathbf{x}} + [\mathbf{C}]\dot{\mathbf{x}} + [\mathbf{K}]\mathbf{x} = \mathbf{f}_{ext}(\omega, t) - \mathbf{f}_{nl}(\mathbf{x}, \dot{\mathbf{x}}) = \mathbf{f}(\mathbf{x}, \dot{\mathbf{x}}, \omega, t), \tag{3.30}$$

in which all nonlinear effects are considered as a distinct force component $\mathbf{f}_{nl}(\mathbf{x}, \dot{\mathbf{x}})$, the external excitation forces are represented by $\mathbf{f}_{ext}(\omega, t)$, $\mathbf{x}$ and $\dot{\mathbf{x}}$ are the state variables vectors and $[\mathbf{M}]$, $[\mathbf{C}]$ and $[\mathbf{K}]$ stand for the system's mass, damping and stiffness $n \times n$ matrices.

The time dependent elements in Equation 3.30 can then be approximated by their Fourier series truncated at N_H:

$$\mathbf{x}(t) = \mathbf{c}_0^x + \sum_{k=1}^{N_H} \left[\mathbf{s}_k^x \sin\left(\frac{k\omega t}{\nu}\right) + \mathbf{c}_k^x \cos\left(\frac{k\omega t}{\nu}\right) \right] \tag{3.31}$$

$$\mathbf{f}(t) = \mathbf{c}_0^f + \sum_{k=1}^{N_H} \left[\mathbf{s}_k^f \sin\left(\frac{k\omega t}{\nu}\right) + \mathbf{c}_k^f \cos\left(\frac{k\omega t}{\nu}\right) \right] \tag{3.32}$$

where the vectors denoted by $\mathbf{c}_k$ and $\mathbf{s}_k$ contain the Fourier coefficients of the k-th harmonic for all n DoFs of the system.

Substituting the expressions of Equations 3.32 and 3.31 into Equation 3.30 yields the fundamental equation that defines the Harmonic Balance Method problem

$$\mathbf{h}(\mathbf{z}, \omega) \equiv [\mathbf{A}](\omega)\mathbf{z} - \mathbf{b}(\mathbf{z}, \omega) = 0, \tag{3.33}$$

where $[\mathbf{A}]$ is the matrix $(2N_H + 1)n \times (2N_H + 1)n$ containing information on the linear dynamics of the system, while $\mathbf{b}$ is the vector containing the combined Fourier coefficients of external and nonlinear forces. The matrix $[\mathbf{A}]$ and the vectors $\mathbf{b}$ and $\mathbf{z}$ are expressed as

$$[\mathbf{A}] = \begin{bmatrix} \mathbf{K} & & & & & \\ & \mathbf{K} - \left(\frac{\omega}{\nu}\right)^2 \mathbf{M} & -\frac{\omega}{\nu}\mathbf{C} & & & \\ & \frac{\omega}{\nu}\mathbf{C} & \mathbf{K} - \left(\frac{\omega}{\nu}\right)^2 \mathbf{M} & & & \\ & & & \ddots & & \\ & & & & \mathbf{K} - \left(\frac{N_H\omega}{\nu}\right)^2 \mathbf{M} & -\frac{N_H\omega}{\nu}\mathbf{C} \\ & & & & \frac{N_H\omega}{\nu}\mathbf{C} & \mathbf{K} - \left(\frac{N_H\omega}{\nu}\right)^2 \mathbf{M} \end{bmatrix}, \tag{3.34}$$

$$\mathbf{z} = \begin{bmatrix} \mathbf{c}_0^x \\ \mathbf{s}_1^x \\ \mathbf{c}_1^x \\ \vdots \\ \mathbf{s}_{N_H}^x \\ \mathbf{c}_{N_H}^x \end{bmatrix} \quad \text{and} \quad \mathbf{b} = \begin{bmatrix} \mathbf{c}_0^f \\ \mathbf{s}_1^f \\ \mathbf{c}_1^f \\ \vdots \\ \mathbf{s}_{N_H}^f \\ \mathbf{c}_{N_H}^f \end{bmatrix}. \tag{3.35}$$

The Harmonic Balance Method is then reduced to the optimization problem of finding the $\mathbf{z}$ coefficients that lead to $\mathbf{h}(\mathbf{z},\omega) = 0$. It becomes clear that the choice of ω and ν, which ultimately define the frequency components considered in the search for a periodic solution, is also highly significant for fully defining the problem.

To find the roots of Equation 3.33, however, since $\mathbf{b}$ depends on $\mathbf{z}$, an iterative process is required, such as Newton-Raphson or Powell's methods. For this, at each step of the iteration, the computation of both $\mathbf{b}$ and $\partial\mathbf{h}/\partial\mathbf{z}$ is required.

For strongly nonlinear problems, the computation of $\mathbf{b}$ directly from the coefficients of $\mathbf{z}$, i.e., strictly in the frequency-domain, may prove to be a challenging and often impractical task. For this reason, most of the literature references suggest the use of an AFT technique to compute $\mathbf{b}$, which profits from the fast Fourier transform (FFT), following the sequence

$$\mathbf{z} \xrightarrow{\text{FFT}^{-1}} \mathbf{x}(t) \rightarrow \mathbf{f}(\dot{\mathbf{x}},\mathbf{x},\omega,t) \xrightarrow{\text{FFT}} \mathbf{b}(\mathbf{z},\omega). \tag{3.36}$$

Alternatively, instead of using the FFT, it is possible to write the inverse Direct Fourier Transform (DFT) as a linear operator $\mathbf{\Gamma}(\omega)$ (NARAYANAN; SEKAR, 1998; KIM; ROOK; SINGH, 2005). For this, it is necessary first to define an adequate time-domain discretisation to be used and build the expanded forms of $\tilde{\mathbf{f}}$ and $\tilde{\mathbf{x}}$ as

$$\tilde{\mathbf{f}} = \begin{bmatrix} f_1(t_1) \\ \vdots \\ f_1(t_N) \\ \vdots \\ f_n(t_1) \\ \vdots \\ f_1(t_N) \end{bmatrix} \quad ; \quad \tilde{\mathbf{x}} = \begin{bmatrix} x_1(t_1) \\ \vdots \\ x_1(t_N) \\ \vdots \\ x_n(t_1) \\ \vdots \\ x_1(t_N) \end{bmatrix}. \tag{3.37}$$

The time discretisation must be well-defined based on the frequency parameters ω and ν. To have optimal performance when applying the DFT, minimizing the calculation time and adequately presenting the highest frequencies harmonics considered, the time step $dt = t_{i+1} - t_i \quad \forall \quad i = 1,..,N$ must be set as

$$dt = \frac{\pi\nu}{\omega N_H}. \tag{3.38}$$

Similarly, the last time sample t_N must be set to correctly represent at least a full period of the lowest frequency harmonic $\frac{\omega}{\nu}$, eliminating leakage effects. This can be achieved by defining

$$t_N = \frac{2\pi\nu}{\omega} - dt. \tag{3.39}$$

Once these parameters have been correctly defined, the inverse Fourier transform can then be written as

$$\tilde{\mathbf{x}} = \mathbf{\Gamma}(\omega)\mathbf{z} \tag{3.40}$$

with the sparse linear operator $\mathbf{\Gamma}$ defined as

$$\mathbf{\Gamma}(\omega) = \begin{bmatrix} \mathbb{I}_n \otimes \begin{bmatrix} 1 \\ 1 \\ \vdots \\ 1 \end{bmatrix} & \mathbf{\Gamma}_1^h & \mathbf{\Gamma}_2^h & \dots & \mathbf{\Gamma}_{N_H}^h \end{bmatrix}, \tag{3.41}$$

where

$$\mathbf{\Gamma}_k^h = \begin{bmatrix} \mathbb{I}_n \otimes \begin{bmatrix} \sin(k\omega t_1) \\ \sin(k\omega t_2) \\ \vdots \\ \sin(k\omega t_N) \end{bmatrix} & \mathbb{I}_n \otimes \begin{bmatrix} \cos(k\omega t_1) \\ \cos(k\omega t_2) \\ \vdots \\ \cos(k\omega t_N) \end{bmatrix} \end{bmatrix}, \tag{3.42}$$

and $\otimes$ denotes the Kronecker product and $\mathbb{I}_n$ is the $n \times n$ identity matrix.

Once the inverse Fourier transform linear operator $\mathbf{\Gamma}$ is defined, we can then write the direct Fourier transform as

$$\mathbf{z} = \mathbf{\Gamma}^+(\omega)\tilde{\mathbf{x}}, \tag{3.43}$$

where $\mathbf{\Gamma}^+ = \mathbf{\Gamma}^T(\mathbf{\Gamma}\mathbf{\Gamma}^T)^{-1}$ represents the Moore-Penrose pseudoinverse of the $\mathbf{\Gamma}$ operator.

Once we have established these relations, the frequency-domain representation of the system's forces $\mathbf{b}$ can be easily computed as

$$\mathbf{b}(\mathbf{z}, \omega) = \mathbf{\Gamma}^+(\omega)\tilde{\mathbf{f}}. \tag{3.44}$$

Obtaining the partial derivatives of $\mathbf{h}(\mathbf{z}, \omega)$ in the form of the jacobian matrix $\mathbf{J}_\mathbf{z}$ is of the utmost importance for the efficient computation of the roots of equation 3.33 using iterative optimization procedures. This jacobian matrix can be defined as

$$\mathbf{J}_\mathbf{z} = \frac{\partial \mathbf{h}}{\partial \mathbf{z}} = \mathbf{A} - \frac{\partial \mathbf{b}}{\partial \mathbf{z}}. \tag{3.45}$$

The computation of $\partial \mathbf{b}/\partial \mathbf{z}$ can also be very challenging to derive analytically. Then it is possible to profit from the relations previously described to calculate these derivatives using the time-domain vectors $\tilde{\mathbf{f}}$ and $\tilde{\mathbf{f}}$, which are significantly easier to calculate.

$$\frac{\partial \mathbf{b}}{\partial \mathbf{z}} = \frac{\partial \mathbf{b}}{\partial \tilde{\mathbf{f}}} \frac{\partial \tilde{\mathbf{f}}}{\partial \tilde{\mathbf{x}}} \frac{\partial \tilde{\mathbf{x}}}{\partial \mathbf{z}} = \mathbf{\Gamma}^{+} \frac{\partial \tilde{\mathbf{f}}}{\partial \tilde{\mathbf{x}}} \mathbf{\Gamma} \tag{3.46}$$

The time-domain derivatives $\partial\tilde{\mathbf{f}}/\partial\tilde{\mathbf{x}}$ can be obtained analytically, which significantly reduces the computational cost of the calculation $\mathbf{J}_{\mathbf{z}}$.

3.3.2 Stability of periodic solutions in nonlinear systems

3.3.2.1 Floquet multipliers

There are different methods for evaluating the stability of a system's behavior. When the interest is to determine if a specific periodic solution is stable, calculating the Floquet Multipliers associated with this solution's orbit can be the easiest alternative. First introduced by G. Floquet in 1883 (FLOQUET, 1883) as a part of the study on differential equations with periodic coefficients, known as Floquet Theory, the Floquet Multipliers are a mathematical quantity that can reveal the asymptotic behavior of a given periodic solution of a known autonomous system.

As thoroughly described by Skubachevskii & Walther (2006) and Lust (2001), if we assume a certain nonlinear system defined by

$$x'(t) = f(x), \tag{3.47}$$

we can suppose that $y(t)$ is a periodic solution of Eq. 3.47, and $T > 0$ is the period of y. The behavior of solutions of this same equation with initial values close to the periodic orbit formed by $y(t)$ is determined by the *monodromy matrix* $\mathbf{M}$ defined as

$$\mathbf{M}(t_0) = \left.\frac{\partial \phi_T(x_0)}{\partial x_0}\right|_{x_0 = y(t_0)}, \tag{3.48}$$

where $\phi_T(x_0)$ denotes the solution of Eq. 3.47 at time T and starting from x_0 at time $t = t_0$.

As can be understood from Eq. 3.48, the monodromy matrix $\mathbf{M}(t_0)$ is a sort of gradient matrix that can describe how a small deviation $\boldsymbol{\varepsilon}(t)$ imposed on the periodic solution $y(t)$ in $t = t_0$ will evolve from $\boldsymbol{\varepsilon}(t_0)$ to $\boldsymbol{\varepsilon}(t_0 + T)$ in such a way that

$$\boldsymbol{\varepsilon}(t_0 + T) = \boldsymbol{\varepsilon}(t_0)\mathbf{M}(t_0). \tag{3.49}$$

It can be shown that, although $\mathbf{M}(t_0)$ is dependent on the value chosen for t_0, its eigenvalues are not. For this reason, we shall henceforth refer to $\mathbf{M}_0 = \mathbf{M}(0)$ as the monodromy matrix, which fully covers the purposes of this work.

The eigenvalues $\lambda \neq 0$ of the monodromy matrix $\mathbf{M}_0$ are called *Floquet Multipliers*. There will always be at least one eigenvalue $\lambda = 1$, called the *trivial Floquet Multiplier*, with associated eigenvector $\mathbf{u}_0 = f'(y(0))$. If all non trivial Floquet Multipliers are found to fall within the complex unit circle, the periodic solution y is stable, and exponentially attracts any other orbit close to ϕ_t. If any of the Floquet Multipliers are outside the complex unit circle, this solution is unstable.

The monodromy matrix can then be computed as the solution at time T if the variational equation

$$\frac{d\mathbf{M}_0(t)}{dt} = \left.\frac{\partial f(x)}{\partial x}\right|_{x=y(t)} \mathbf{M}(t) \quad , \quad \mathbf{M}_0(0) = \mathbb{I}. \tag{3.50}$$

The computation of Floquet Multipliers for each periodic solution obtained using the HBM approach enables one to evaluate the solution's stability and can be used as a criterion for selecting "acceptable" periodic solutions.

As an example, Figure 3.12 shows the Frequency Response plots of a multi-DoF nonlinear system obtained by both HBM and direct integration (RK4) procedures. The points indicated as Flagged (black points) correspond to situations where a periodic solution could not be found, and the points marked as Unstable (red x) are periodic solutions with at least one Floquet Multiplier greater than 1, therefore indicating unstable orbits.

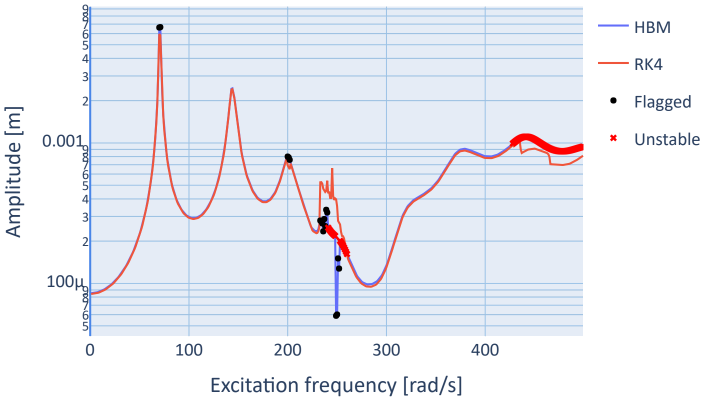

Figure 3.12 – Frequency Response obtained with both HBM and direct integration.

4 Rainbow gyroscopic disk metastructures for broadband vibration attenuation in rotors

In this chapter, we delve into the first stage of the exploration of rotating metastructures proposed in this thesis. A vibration control approach in rotating machinery is proposed based on the concept of locally resonant periodic and rainbow disk metastructures. The effects of periodic resonators are investigated in a first approach, and then rainbow arrangements are also studied to evaluate the possible improvements on vibration attenuation performance that have been reported in the literature. Unique effects arise from the application of this concept to a rotating structure as a result of the gyroscopic effects of the attached resonators. Section 4.1 presents the finite element model of a simple rotor, i.e., a spinning shaft supported by isotropic bearings at both ends. Moreover, two types of resonators are described. The first is based on the resonators' translational modes, while the second takes advantage of its rotational modes. The second approach is strongly influenced by the resonators' gyroscopic effects, thus its natural frequency depends on the rotation speed. The model was built using the software Ross, an open source Python based rotordynamics tool (TIMBÓ et al., 2020). The system's vibration response to forward and backward synchronous excitation is calculated and analysed. Section 4.1.1 presents the effects of translational resonators in the periodic and rainbow cases. The dynamic of this type of resonators is not influenced by the gyroscopic effect. Consequently, the metastructure presents a band of resonating modes unaffected by the rotation speed, and corresponding acoustic modes, i.e. resonators in-phase with the shaft, and optical modes, i.e. resonators out-of-phase with the shaft, at the same frequency band for both forward and backward modes. Section 4.1.2 presents a similar analysis for rotational resonators. In this case, the resonant modes are dependent on the rotation speed and they split in two frequency branches for backward and forward modes. Finally, section 4.3 presents final comments and concluding remarks.

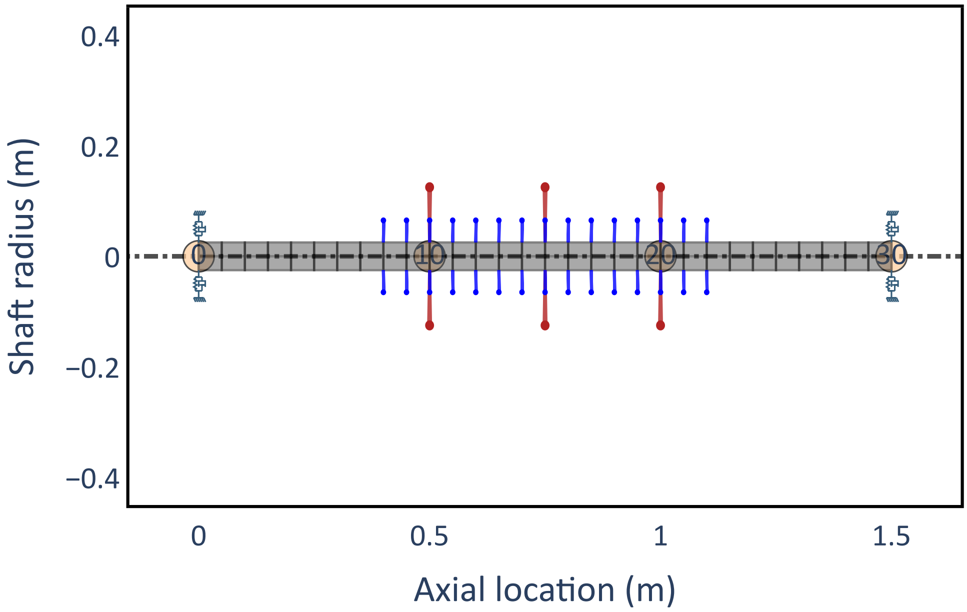

Figure 4.1 – Rotor FEM model of the shaft (grey), rigid axisymmetric disks (red), isotropic bearings (dark blue) and resonators (light blue), the bearings at the ends.

4.1 Rotor model

In this section, the physical model is presented, as depicted in Figure 4.1. It consists of a rotor (gray) supported by two isotropic bearings modeled as spring-dampers (dark blue), three rigid axisymmetric disks (red) representing impellers or other mechanical components commonly attached to rotors, and evenly distributed local resonators (light blue). The rotor's dynamic response is evaluated through Finite Element Method (FEM) simulations, based on ROSS - Rotordynamic OpenSource Software (TIMBÓ et al., 2020). Adaptations are introduced in the software to take into account the local resonators. The FEM model is built using 4 degrees of freedom Timoshenko beam elements. Every shaft element is identical, with aspect ratio $L/D = 0.5$. The local resonators are modeled as cylindrical elements with outer diameter $d_o = 140$ mm, inner diameter $d_i = 60$ mm and length $L = 40$ mm, as shown in Figure ??. The mass of the resonators, m_r, and transverse and polar moments of inertia, $I_{t_{\text{res}}}$ and $I_{p_{\text{res}}}$, respectively, are obtained from the proposed geometry. The vibration modes of interest of the resonators undergo two types of oscillation. The first is predominantly translational, i.e., the movement follows the x-direction in the local frame of reference, Fig. ??. In the second vibration mode of interest, named rotational, the oscillations are dominated by the rotations around the θ_y degree of freedom in the local frame of reference.

The equations of motion are given by

$$[\mathbf{M}]\ddot{\mathbf{x}} + ([\mathbf{C}] + \Omega[\mathbf{G}])\dot{\mathbf{x}} + [\mathbf{K}]\mathbf{x} = 0, \tag{4.1}$$

where $[\mathbf{M}]$, $[\mathbf{C}]$ and $[\mathbf{K}]$ are the mass, damping, and stiffness matrices, respectively. The matrix $[\mathbf{G}]$ is the gyroscopic matrix that appears multiplied by the shaft rotation speed Ω. The vector $\mathbf{x}$ represents the displacements and is constructed as $\mathbf{x} = \{\mathbf{x}_1 \ \ldots \ \mathbf{x}_n \ \ldots \ \mathbf{x}_{N+N_r}\}^T$, where N is the total number of shaft nodes, N_r is the number of resonators and $\mathbf{x}_n$ is the displacement vector of each individual shaft node and is described by $\mathbf{x}_n = \{x \ y \ \theta_x \ \theta_y\}$.

The $[\mathbf{M}]$, $[\mathbf{C}]$, $[\mathbf{G}]$, and $[\mathbf{K}]$ matrices are built by components that represent both the main shaft and the resonators. Figure 4.2 presents the composition of matrix $[\mathbf{K}]$, showing the coupling between shaft and resonators. In the representation, $\mathbf{O}_{M\times M}$ is a $M \times M$ zero matrix and $[\mathbf{K}_{\text{shaft}}]$ is the bare rotor stiffness matrix. The arrangement of all the other matrices of Equation 4.1 follows a similar idea.

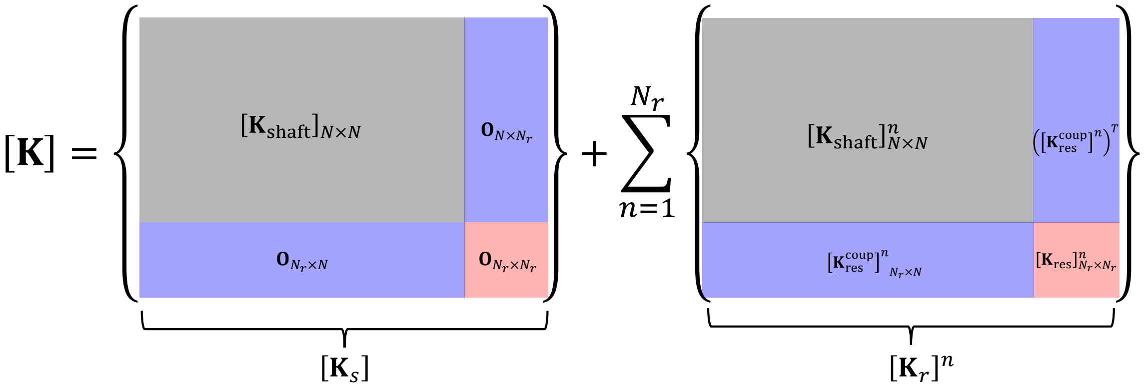

Figure 4.2 – Stiffness matrix arrangement in sparse representation.

Figure 4.2 shows $[\mathbf{K}_r]^n$ and $[\mathbf{K}_s]$ as sparse, $(N + N_r) \times (N + N_r)$ matrices. In addition, the n^{th} resonator element stiffness and damping matrices can also be represented by the 8×8 matrices as follows

$$[\mathbf{K}_r]^n = \begin{bmatrix} k_0 & 0 & 0 & 0 & -k_0 & 0 & 0 & 0 \\ 0 & k_0 & 0 & 0 & 0 & -k_0 & 0 & 0 \\ 0 & 0 & k_1 & 0 & 0 & 0 & -k_1 & 0 \\ 0 & 0 & 0 & k_1 & 0 & 0 & 0 & -k_1 \\ -k_0 & 0 & 0 & 0 & k_0 & 0 & 0 & 0 \\ 0 & -k_0 & 0 & 0 & 0 & k_0 & 0 & 0 \\ 0 & 0 & -k_1 & 0 & 0 & 0 & k_1 & 0 \\ 0 & 0 & 0 & -k_1 & 0 & 0 & 0 & k_1 \end{bmatrix} \quad \text{and} \quad [\mathbf{C}_r]^n = c_p [\mathbf{K}_r]^n \quad (4.2)$$

where k_0 and k_1 are, respectively, the translational and rotational stiffness values that connect the resonator to the shaft and c_p is a proportional damping coefficient. The stiffness coefficients are calculated to tune the resonators in the desired frequency, their values being a function of natural frequency, ω_0, and the rotational natural frequency, ω_1, as

$$k_0 = m_r \omega_0^2 \quad , \quad k_1 = I_{t_{\text{res}}} \omega_1^2. \tag{4.3}$$

Similar to the stiffness matrix, the mass and gyroscopic element matrices for the n^{th} resonators can be written as

$$[\mathbf{M}_r]^n = \begin{bmatrix} 0 & 0 & 0 & 0 & 0 & 0 & 0 & 0 \\ 0 & 0 & 0 & 0 & 0 & 0 & 0 & 0 \\ 0 & 0 & 0 & 0 & 0 & 0 & 0 & 0 \\ 0 & 0 & 0 & 0 & 0 & 0 & 0 & 0 \\ 0 & 0 & 0 & 0 & m_r & 0 & 0 & 0 \\ 0 & 0 & 0 & 0 & 0 & m_r & 0 & 0 \\ 0 & 0 & 0 & 0 & 0 & 0 & I_{t_{\text{res}}} & 0 \\ 0 & 0 & 0 & 0 & 0 & 0 & 0 & I_{t_{\text{res}}} \end{bmatrix} \quad \text{and} \quad [\mathbf{G}_r]^n = \begin{bmatrix} 0 & 0 & 0 & 0 & 0 & 0 & 0 & 0 \\ 0 & 0 & 0 & 0 & 0 & 0 & 0 & 0 \\ 0 & 0 & 0 & 0 & 0 & 0 & 0 & 0 \\ 0 & 0 & 0 & 0 & 0 & 0 & 0 & 0 \\ 0 & 0 & 0 & 0 & 0 & 0 & 0 & 0 \\ 0 & 0 & 0 & 0 & 0 & 0 & 0 & 0 \\ 0 & 0 & 0 & 0 & 0 & 0 & 0 & I_{p_{\text{res}}} \\ 0 & 0 & 0 & 0 & 0 & 0 & -I_{p_{\text{res}}} & 0 \end{bmatrix}. \tag{4.4}$$

This representation considers the convention of counter-clockwise (X to Y) rotation for speed Ω. It is important to note that the rotation speed Ω from Equation 4.1 multiplies the entire $[\mathbf{G}]$ matrix, which is composed of $[\mathbf{G}]_s$ and $[\mathbf{G}_r]^n$. Therefore, the same rotation speed is imposed both on the rotor main structure and on the resonators. In addition, from Equation 4.4 one observes that when $\Omega > 0$ the $[\mathbf{G}]$ matrix has the effect of coupling the angular velocity $\dot{\theta}_x$ to a moment M_y in the $-\theta_y$ direction and the angular velocity $\dot{\theta}_y$ creates a moment M_x in the θ_x direction.

For the rainbow metastructure, the mass of each resonator along the shaft follows a specific spatial profile. For this purpose, the $[\mathbf{M}_r]^n$ matrix of the n^{th} resonator element is multiplied by a factor ε_n given by

$$\varepsilon_n = 1 + 0.3 \left(\frac{2n}{N} - 1 \right)^m , \tag{4.5}$$

where N is the total number of resonators and $m = 1, 3, 5...$ is a variable that enables manipulation of the mass gradient distribution. This distribution imposes a variation of -30% to $+30\%$ on the chosen parameter while maintaining the average value for the whole array and its central element remains unchanged. Note that for the periodic case, all masses have identical values such that $\varepsilon_n = 1$.

Numerical simulations were performed with the values of the parameters summarised in Table 1. The parameters k_{xx}, k_{yy}, k_{xy} and k_{yx} represent the direct and cross-coupled stiffness coefficients of the rotor supports, c_{xx} and c_{yy} are the support's direct damping coefficients, and I_t and I_p are the transverse and polar inertia of the disk elements. Proportional damping was considered such that $c_p = 10^{-4}$ s.

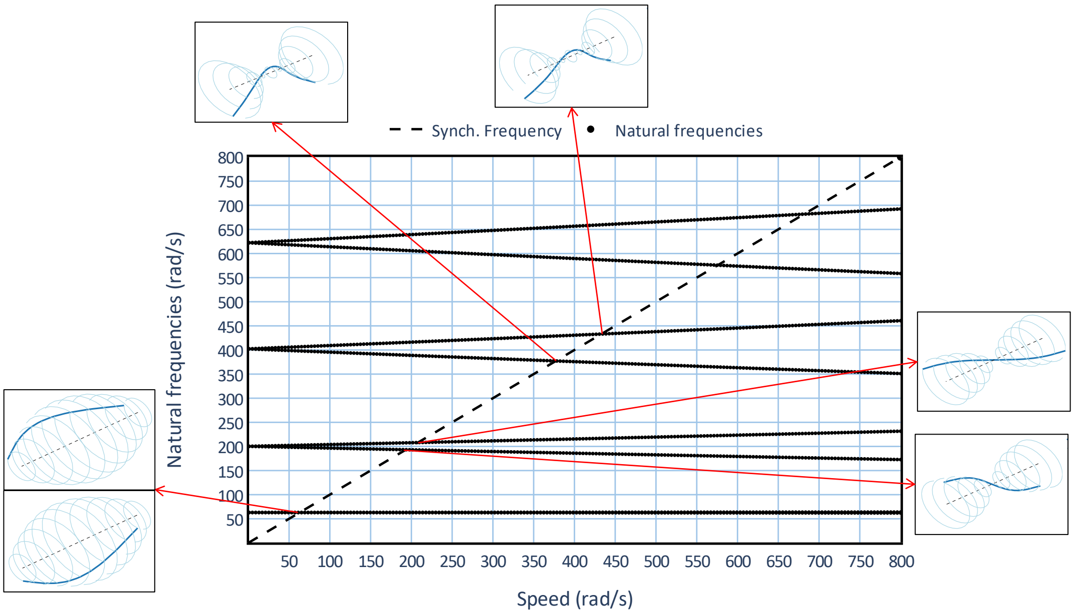

Figure 4.3 – Campbell Diagram and the mode shapes of the corresponding synchronous natural frequencies of the bare the rotor.

Diameter	50 mm	N^o of disks	3
N^o of Elements	30	Disk mass	32,59 kg
Length	1.5 m	I_t	1.78 kg.m^2
Mass	120 kg	I_p	0.33 kg.m^2
Material	Steel	$k_{xx} = k_{yy}$	9×10^6 N/m
$k_{xy} = k_{yx}$	0	$c_{xx} = c_{yy}$	500 Ns/m

Table 1 – FEM parameters, geometrical and material properties of the rotor model.

Figure 4.3 presents the Campbell Diagram of the rotor, assuming the resonators to be rigid lumped mass attachments, i.e., neglecting the dynamics of the resonators but including the effect of the added mass. The results are shown from 0 rad/s to 800 rad /s, so that the first 8 natural frequencies are considered, with steps of 4 rad/s. The points in which the dashed line intersects each of the modes are known as the system's critical speeds. They usually represent the occurrence of the maximum vibration amplitudes in a rotor system, for either forward or backward excitation. The synchronous 1× component is shown as a dashed black line. The first two modes occur close to 60 rad/s and are dominated by the rotor supports stiffness, the separation of its forward and backward components do not become clearly visible on the diagram. The second set of modes, starting at 200 rad/s, corresponds to the conical rigid body modes, which present significant amplitudes of the angular degrees of freedom and visible separation of forward and backward components. The remaining 4 modes are bending modes of the rotor shaft and also clearly show the separation between forward and backward modes. The separation between forward and backward modes is caused by the gyroscopic effect, which couples the angular velocity $\dot{\theta}_x$ with a moment M_y and the angular velocity $\dot{\theta}_y$ with a moment M_x.

The proposed approach aims to neutralize the first bending backward critical speed located around 377 rad/s. The bending mode is chosen because it tends to have a greater energy concentration in the shaft's bending motion when compared to the rigid body modes, which makes it a better target for rotational resonators. The backward mode was chosen because it allows the interactions between the shaft and the rotational resonators to be simpler and more easily understood. Although forward modes are usually of greater concern in practical applications, backward ones can also be relevant, especially in highly anisotropic rotor systems.

The performance of both translational and rotational resonators is evaluated. The effectiveness of bandgap formation with rotational resonators, which are those in which stiffness only k_1 is of concern, is limited compared to translational elements (SUN; DU; PAI, 2010). However, there are specific characteristics of rotational resonators that can be explored when considering rotor-like structures due to gyroscopic coupling (ATTARZADEH et al., 2019). In such structures, the system's equations of motion are a function of the rotation speed Ω and it contains components that couple the orthogonal angular directions.

4.1.1 Translational resonators

In this case, only the translational modes of the resonators are of concern. In order to attenuate the third backward critical speed, we consider $\omega_0 = 377$ rad/s. The rotational natural frequency of the resonator is $\omega_1 = 10\omega_0$, such that their motion can be considered as purely translational within the considered frequency band, while maintaining the same FEM model.

Figure 4.4 shows the Campbell Diagram for the periodic case and the rainbow resonators. For both cases, new branches appear on the diagram corresponding to the new vibration modes created with the attachment of the resonators. Note that the branches corresponding to the first two cylindrical modes and the last two elastic flexural modes remain unaltered. However, in the targeted region with a tuning frequency of $\omega_0 = 377$ rad/s there are more complex interactions. Additionally, the vibration modes corresponding to resonators natural frequency appear as horizontal branches, independent of the shaft's rotation speed. This is because this mode of the resonator is not affected by the gyroscopic coupling. It can also be seen that it creates side modes at the limits of the bandgap region. Figure 4.4 also presents a color scale that gives the spatially averaged amplification

$$A_{\text{avg}} = \frac{1}{N}\sum_{n=1}^{N} A_i, \tag{4.6}$$

and phase angle

$$\phi_{\text{avg}} = \frac{1}{N}\sum_{n=1}^{N} \phi_i, \tag{4.7}$$

between the N resonators and main structure, where $X^i_{\text{res}}/X^i_{\text{rotor}} = A_i e^{j\phi_i}$. In this definition, A_i and ϕ_i are scalar values and X^i_{res} and X^i_{rotor} are the translational eigenvector components corresponding to the i^{th} resonator and the rotor node to which it is attached. The amplification A_{avg} is saturated for better visualization of the region of interest. It is clear that the side modes are dominated by the shaft's vibration, while the resonator modes are dominated by the resonators' vibration.

The rainbow configuration is produced assuming $m = 1$ in Equation 4.5, and presents a similar behavior for the rigid body modes and the higher order modes. The modes dominated by the resonators are also constant with respect to the rotation speed, but they are distributed over a wider frequency range, following the mass spatial distribution. This has the effect of widening the bandgap region, as expected (FABRO et al., 2021). Moreover, in both cases the phase angle clearly shows the acoustic modes, where the rotor and the resonators vibrate in phase, and the optical modes at higher frequencies, where they vibrate out of phase (SUN; DU; PAI, 2010). Thus, it is clear that the local resonance effect is created due to the presence of natural modes of the resonators, which absorb mechanical energy and consequently attenuate vibration.

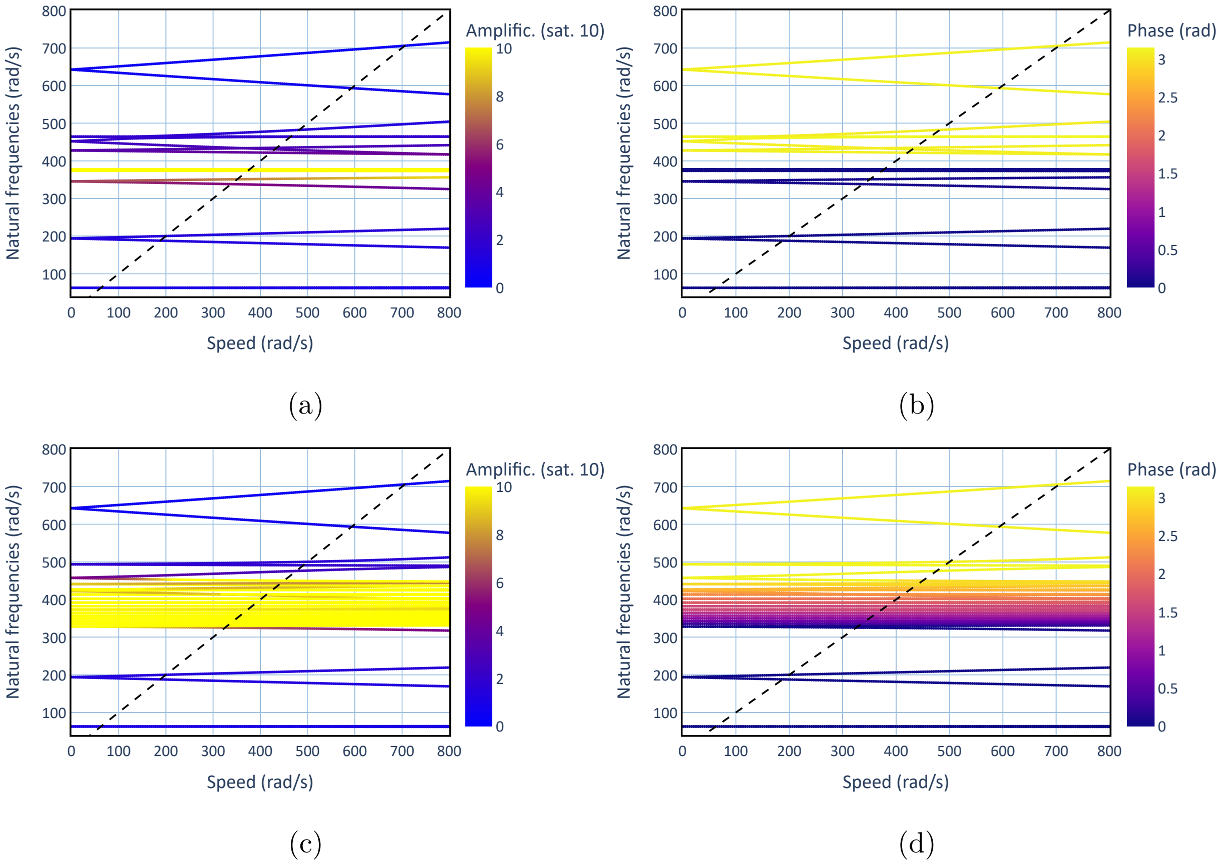

(a) (b)

(c) (d)

Figure 4.4 – Campbell diagrams with translational resonators tuned to 377 rad/s. (a) Periodic resonators and A_{avg} colorscale. (b) Periodic resonators and ϕ_{avg} colorscale. (c) Rainbow resonators and A_{avg} colorscale. (d) Rainbow resonators and ϕ_{avg} colorscale.

However, it is important to note that the performance enhancement effects of the rainbow configuration are not unlimited with respect to the gradation profile. The bandgap is widened by the effect of overlapping the smaller adjacent bandgaps. If individual bandgaps no longer have, or have very small overlapping regions, the bandgap widening effect will fade and the attenuation performance will be reduced .

4.1.1.1 Forced response

At this point, harmonic excitation is of concern. The system's steady-state forced response is obtained using its Transfer Matrix, $[\mathbf{H}_\omega]$, defined in complex form as

$$[\mathbf{H}_\omega] = (\mathrm{j}\omega\mathbb{I} - [\mathbf{A}])^{-1}, \tag{4.8}$$

where $\mathrm{j} = \sqrt{-1}$, ω is the excitation frequency, $\mathbb{I}$ is the identity matrix, and $[\mathbf{A}]$ is the system's state space matrix which satisfies

$$\dot{\mathbf{y}} = [\mathbf{A}]\mathbf{y} + \mathbf{B}, \tag{4.9}$$

where $\mathbf{y}$ is the state space vector and $\mathbf{B}$ is the excitation vector, thus, the steady-state response of the system to a harmonic excitation $\mathbf{B}_\omega$ can be obtained by

$$\mathbf{y}_\omega = [\mathbf{H}_\omega]\mathbf{B}_\omega. \tag{4.10}$$

Two different load cases are considered, each one consisting of forward and backward unitary rotating forces applied to the shaft's first node. The amplitude and phase of the orthogonal components of these forces can be written, in polar notation, as

$$F_{x_f} = 1\underline{/0^\circ} \quad \text{and} \quad F_{y_f} = 1\underline{/-90^\circ} \tag{4.11}$$

for the forward excitation case and as

$$F_{x_b} = 1\underline{/0^\circ} \quad \text{and} \quad F_{y_b} = 1\underline{/90^\circ} \tag{4.12}$$

for the backward excitation case.

Figure 4.5 shows the responses of the last node of the shaft, corresponding to the opposite end of the applied force. The response is shown in terms of the major axis M_{ax} of the node's translational orbit, which is the orbit's biggest diameter (MUSZYNSKA, 2005). These plots compare the response of the bare rotor, i.e. assuming rigid disks attachment, as a dashed black line, the rotor with periodic resonators as the blue dash-dotted line and with rainbow resonators assuming $m = 1$, Equation 4.5, as the solid red line. The system with rigid disk attachments was chosen as baseline for forced response visualization in order to isolate the attenuation effects only, since the added mass has the side-effect of also altering the position of the critical speeds. It can be clearly seen that the periodic and rainbow configurations can successfully attenuate the targeted vibration mode. The periodic case results in a shorter bandgap with stronger maximum attenuation, but with a strong contribution of the side modes. In contrast, the rainbow configuration leads to a wider bandgap but with smaller maximum attenuation, although with significant attenuation for practical applications. This effect is due to the distribution of the resonant modes along the frequency band, as shown in the Campbell diagram of Fig. 4.4. Differences in the bandgap due to forward and backward excitation are due to the different modes that are excited.

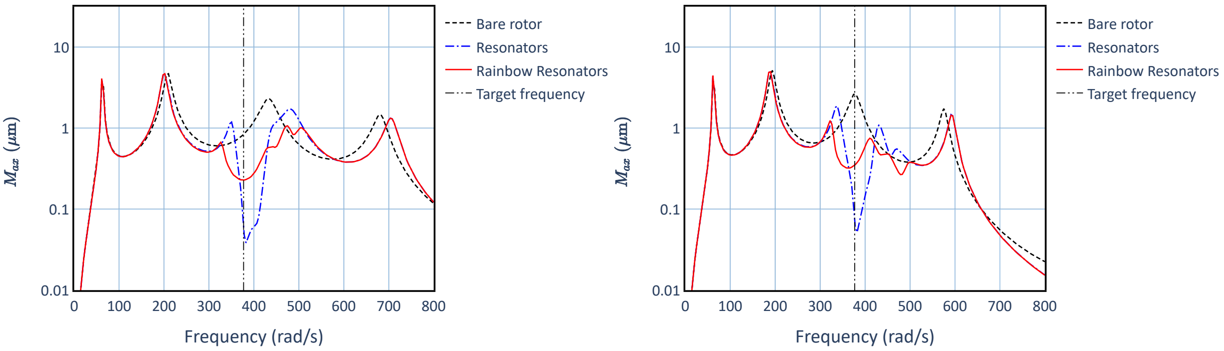

(a)

(b)

Figure 4.5 – Major axis response with translational resonators tuned to 377 rad/s. (a) Forward excitation. (b) Backward excitation.

From Figure 4.6 we can observe the deflected shapes of the main structure at one end for the bare rotor case and for the rotor with translational rainbow resonators, both subjected to backward excitation at the opposite end. The deflected shapes are highlighted at specific points, depicting the main structure in blue lines, and the resonators as red stems, and reveal the interaction between resonators and rotor. From the rainbow resonators it can be seen that the resonators on the edges are excited at the side frequencies and the resonators on rotor's the mid span are excited at the center of the attenuation band, following the resonators mistuning of the gradient profile. The modes at frequencies lower than the bandgap show the resonators vibrating in phase with structural vibration modes, i.e. acoustic modes, while the modes at higher frequencies present the resonators out of phase with the main structure, i.e. optical modes, as discussed in the previous section.

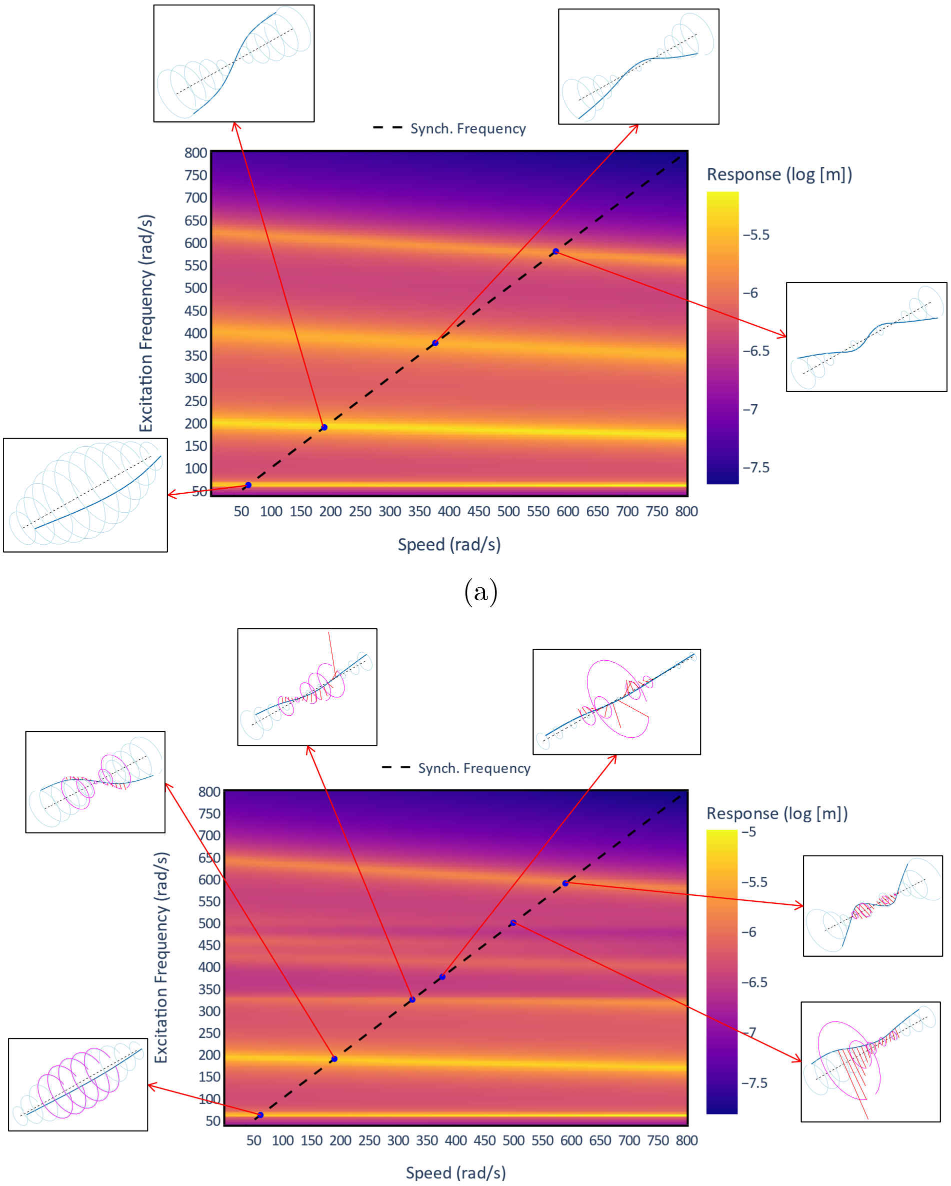

(a)

(b)

Figure 4.6 – Response amplitudes as a function of the frequency and rotation speed of the shaft due to backward excitation. (a) Bare rotor. (b) Translational rainbow resonators.

From the obtained results, it is evident that the translational resonator arrangement produces consistent, broadband vibration attenuation around the chosen tuning frequency. The spatial rainbow profile produced a significant increase in the attenuated frequency range, almost eliminating the effect of side modes occurring around the target frequency.

To further explore the mechanisms involved in generating the observed bandgaps, the deflected shape of the rotor and resonators at each frequency are investigated. Figure 4.7 presents the amplitude response along the rotor with and without the attached resonators for different rotation speeds. The shaft's deflected shape (blue line) and the resonators (red stems) can be compared to the rotor's deflected shape without the resonators (black dashed line). It highlights the strong attenuation effect the resonators provide close to the target frequency. Similarly, Figure 4.8 shows the deflected shapes for the case of rainbow resonators. In this case, different sections of the array of resonators are activated at each frequency, highlighting the rainbow effect, providing increased bandwidth for the attenuation effect.

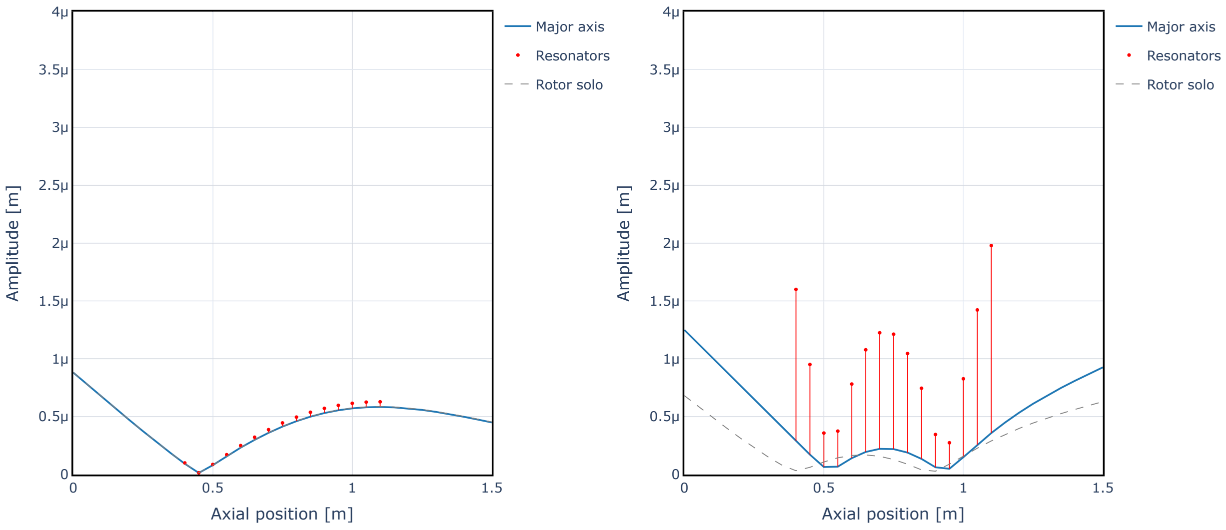

(a) $\Omega = 100$ rad/s (b) $\Omega = 340$ rad/s

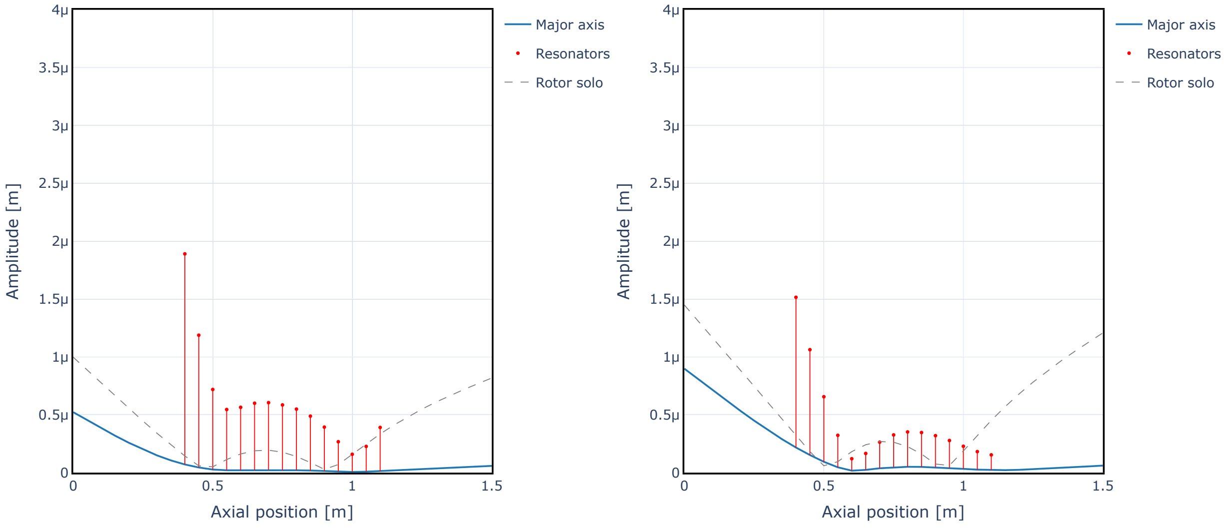

(c) $\Omega = 375$ rad/s (d) $\Omega = 400$ rad/s

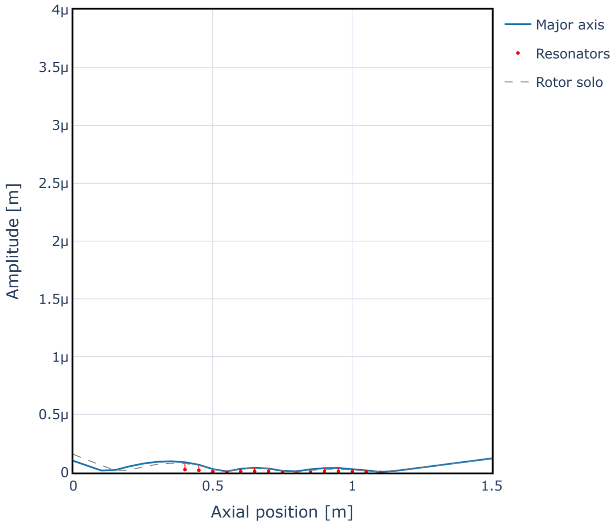

(e) $\Omega = 800$ rad/s

Figure 4.7 – Deflected shapes for periodic translational resonators tuned to 377 rad/s with forward excitation.

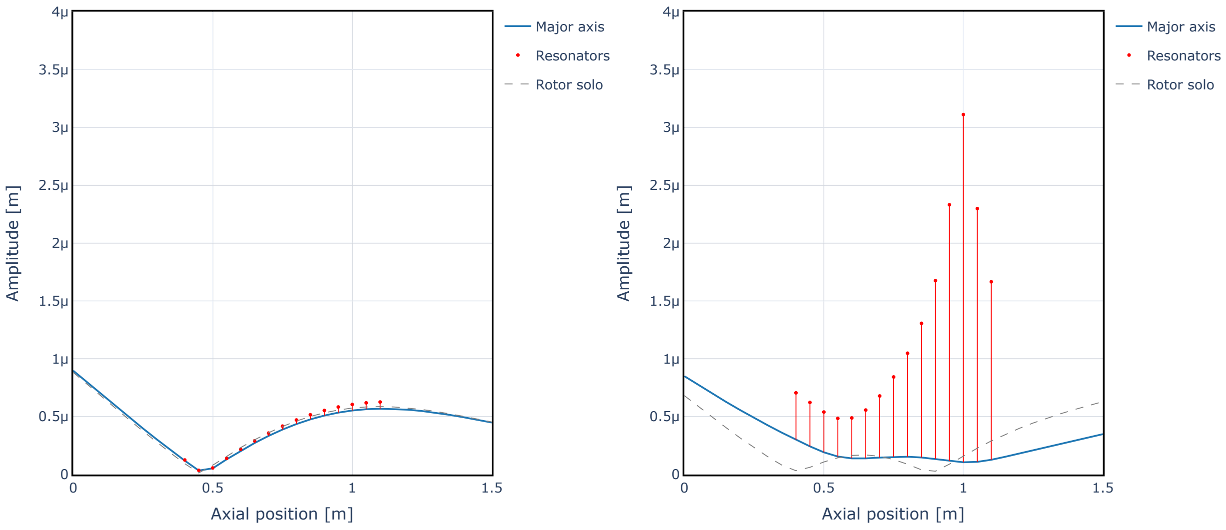

(a) $\Omega = 100$ rad/s (b) $\Omega = 340$ rad/s

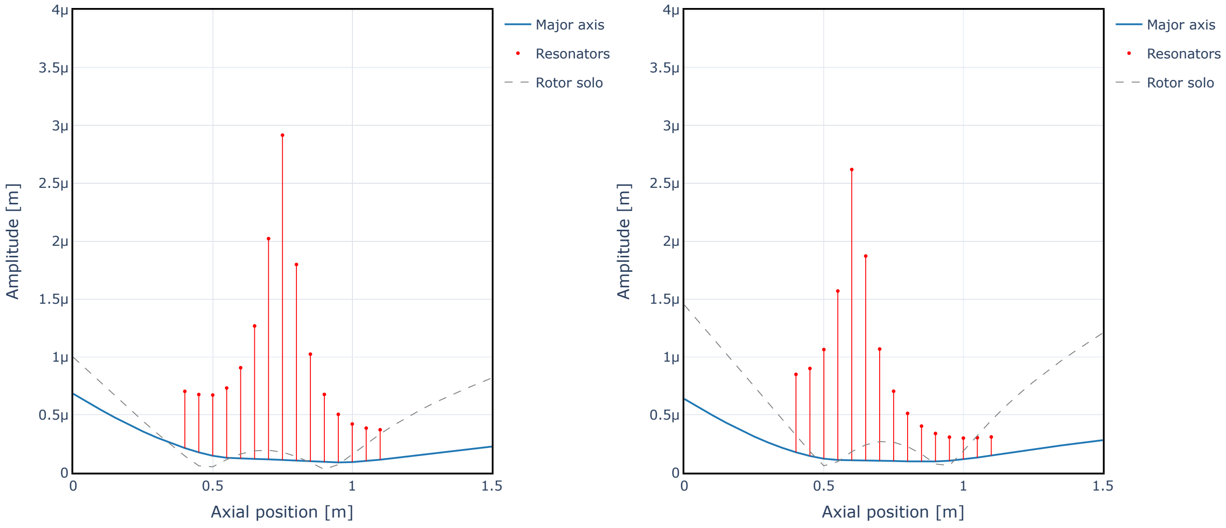

(c) $\Omega = 375$ rad/s (d) $\Omega = 400$ rad/s

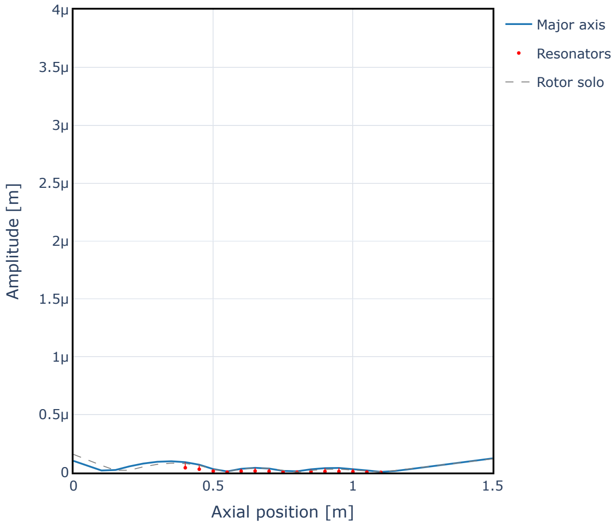

(e) $\Omega = 800$ rad/s

Figure 4.8 – Deflected shapes for translational rainbow resonators tuned to 377 rad/s with forward excitation.

4.1.2 Rotational resonators

In this section, only the rotational mode of the resonators is of concern. A similar approach is carried out to tune the resonators' rotational natural frequency to attenuate the targeted frequency range. Consequently, the resonators are designed such that $\omega_0 = 10\omega_1$ so that the translational mode of the resonator has negligible displacement in the frequency range of interest. In this case, the natural frequency of the resonators $\omega_n(\Omega)$ is a function of the rotation speed Ω. However, the tuning parameter ω_1, as defined in Equation 4.3, is the natural frequency of the resonator without gyroscopic effects $\omega_1 = \omega_n(0)$. To tune the resonators' natural frequency to a target synchronous frequency Ω_t, it is necessary to find ω_1 such that $\omega_n(\Omega)$ satisfies

$$\omega_n(\Omega_t) = \Omega_t. \tag{4.13}$$

The equation of motion of a single rotational resonator attached to the ground by a stiffness κ_t is given by

$$\begin{bmatrix} I_{t_{\mathrm{res}}} & 0 \\ 0 & I_{t_{\mathrm{res}}} \end{bmatrix} \ddot{\mathbf{x}} + \Omega \begin{bmatrix} 0 & I_{p_{\mathrm{res}}} \\ -I_{p_{\mathrm{res}}} & 0 \end{bmatrix} \Omega \dot{\mathbf{x}} + \begin{bmatrix} \kappa_t & 0 \\ 0 & \kappa_t \end{bmatrix} \mathbf{x} = 0, \tag{4.14}$$

from which it is possible to derive the characteristic polynomial equation as

$$\kappa_t^2 - 2I_{t_{\mathrm{res}}}\kappa_t\omega_n^2 + I_{t_{\mathrm{res}}}^2\omega_n^4 - I_{p_{\mathrm{res}}}^2\omega_n^2\Omega^2 = 0. \tag{4.15}$$

By solving this equation, an analytical expression for the roots of ω_n is obtained as

$$\omega_n(\Omega) = \frac{2I_{t_{\mathrm{res}}}\kappa_t + I_{p_{\mathrm{res}}}^2\Omega^2 \pm \sqrt{4I_{t_{\mathrm{res}}}\kappa_t I_{p_{\mathrm{res}}}^2\Omega^2 + I_{p_{\mathrm{res}}}^4\Omega^4}}{2I_{t_{\mathrm{res}}}^2}. \tag{4.16}$$

Thus, it becomes clear that the gyroscopic effects split each pair of eigenvalues into two separate values, where the plus and minus signs yield the forward and backward eigenvalues, respectively.

Combining Equations 4.13 and 4.16, and considering $\sqrt{\kappa_t/I_{t_{\mathrm{res}}}} = \omega_1$, with some algebraic manipulation, we obtain a polynomial in the variable ω_1 that leads to the synchronous tuning condition as

$$\left(\alpha^2 - 2\right)\Omega_t^2 \pm \alpha\Omega_t\sqrt{4\omega_1^2 + \alpha^2\Omega_t^2} + 2\omega_1^2 = 0, \tag{4.17}$$

where $\alpha = I_{p_{\mathrm{res}}}/I_{t_{\mathrm{res}}}$ is the inertia ratio. Thus, the tuning parameter, ω_1, is only a function of the target frequency Ω_t and α. For the target frequency of $\Omega_t = 377$ rad/s we must set the rotational resonators to $\omega_1 = 634.4$ rad/s to satisfy Equation 4.17 using the backward modes of the resonators.

Figure 4.9 presents the Campbell diagram for both periodic and rainbow cases. In this case, some important differences are found in the interaction of the branches related to the rotational resonators, compared to the previous case, with translational resonators. In the periodic case, the resonators backward branch starts at $\omega_1 = 634.4$ rad/s and reaches the target at $\Omega_t = 377$ rad/s, as designed. It is clear from the amplification color scale, defined as in the previous section, that this branch is dominated by the resonators vibration, yellow, while the other forward and backward branches are dominated by the vibration in the rotor, similar to the previous case. However, from the phase color scale it can be noticed that only the backward modes are out of phase at frequencies higher than the bandgap, i.e. optical modes, while all the forward modes in this frequency region are in phase with the resonators, i.e. acoustic modes. It reveals that both optical and acoustic modes coexist in the same frequency band due to the gyroscopic effects in the resonators, unlike the previous case with translational resonators. This result shows that only the backward modes will be attenuated by the interaction with this branch. In addition, the side modes are well defined along the synchronous 1× dashed line, and they follow the gyroscopic effect for other rotation speeds. Notice that for frequencies higher than the synchronous frequency, the lower branch of the side modes are dominated by the resonators vibration. Similarly, the case with rainbow resonators shows the same coexistence of optical and acoustic modes at higher frequencies. The same rainbow effect is observed, consequently widening the attenuation band.

4.1.2.1 Forced response

In this section, response due to concentrated harmonic excitation is of concern. The same loading arrangement described in Section 4.1.1 is considered, and responses to forward and backward excitation are presented in Figures 4.10a and 4.10b, respectively. In this case, the rainbow resonator arrangement also considers $m = 1$ in Equation 4.5, for mass spatial profile. The response is also shown in terms of the major axis M_{ax} of the node's translational orbit. Figure 4.10a presents the amplitude of the response as a function of frequency due to forward excitation. Note that both periodic and rainbow metamaterial configurations do not provide any attenuation effect in this case. This is due to the lack of interaction of the backward branches of the resonators with the forward branches related to the rotor forward vibration modes, as shown in Fig. 4.9. Only the forward modes are excited due to the forward excitation; thus no attenuation is obtained. This complete independence between forward and backward motion occurs only because of the perfectly isotropic nature of the model considered. In real systems, in which some anisotropy is always present, the forward and backward motions would not be fully uncoupled, and the rotor's forward motion would also be affected by the backward modes of the resonators. Since the purpose of this investigation is mostly phenomenological, as the nature of each separate phenomenon is of greatest concern, no anisotropy was considered.

Figure 4.10b shows the amplitude of the response due to the backward excitation.

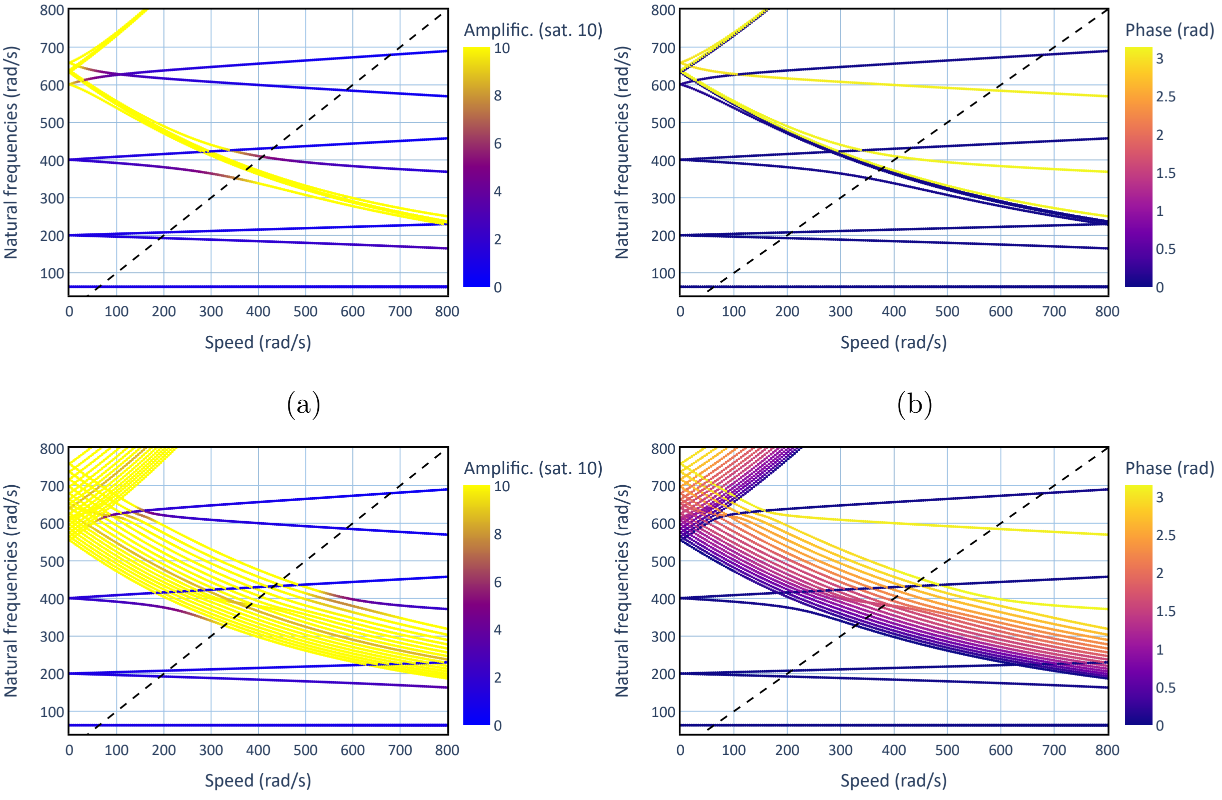

(a) (b)

(c) (d)

Figure 4.9 – Campbell diagrams with rotational resonators tuned to 634.4 rad/s. (a) Periodic resonators and A_{avg} colorscale. (b) Periodic resonators and ϕ_{avg} colorscale. (c) Rainbow resonators and A_{avg} colorscale. (d) Rainbow resonators and ϕ_{avg} colorscale.

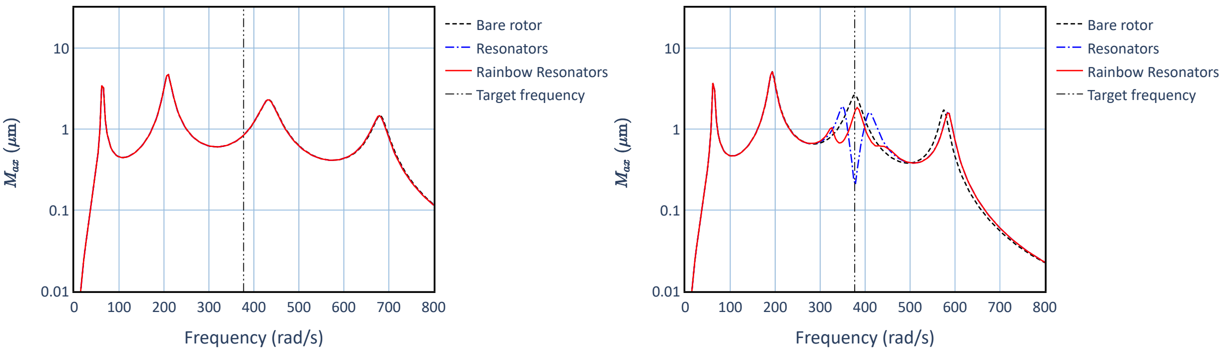

(a) (b)

Figure 4.10 – Amplitude of the frequency response with rotational resonators tuned to 634.4 rad/s. (a) Forward excitation. (b) Backward excitation.

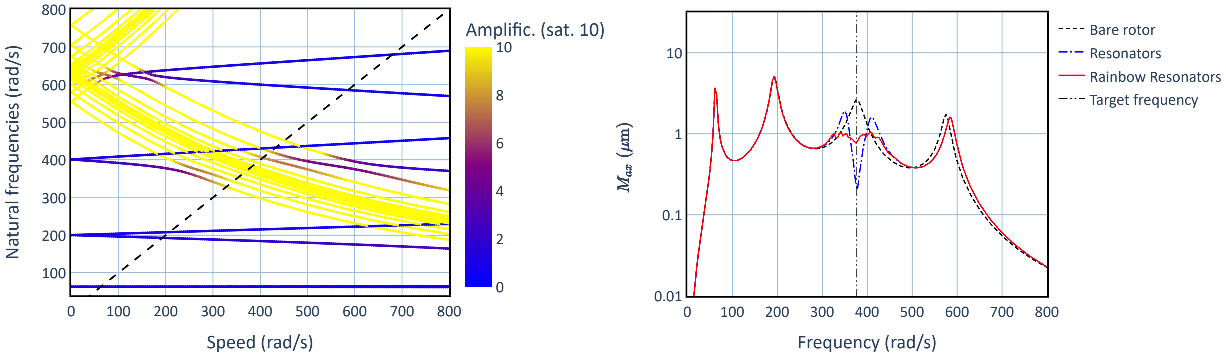

(a) (b)

Figure 4.11 – Campbell diagram (a) and the amplitude of the frequency response to backward excitation (b) with rotational resonators tuned to $634.4rad/s$ and $m = 3$.

In this case, the backward branches of the resonators interact with the backward flexural vibration modes of the rotor, which are excited by the imposed forcing. Consequently, both the periodic and rainbow metastructures yield vibration attenuation. Similarly to the previous case with translational resonators, the periodic case presents high attenuation but a narrow bandgap with vibration amplification at the side modes. On the other hand, the rainbow rotational resonators do not create an effective attenuation around the central frequency of 377 rad/s with this proposed arrangement although slightly reducing the amplification due to resonances.

Increasing the mass gradient distribution exponent to $m = 3$, a significantly improved attenuation performance is observed, as shown in Figure 4.11b, and the resonators are able to neutralize even the side modes on both sides of the target frequency of 377 rad/s. Thus, mass gradient distribution plays an important role in the attenuation performance of the rainbow resonators and optimization strategies can be proposed (MENG et al., 2020c).

Figure 4.12 shows the frequency response of the main structure subjected to excitation at the opposite end. The rotor with no resonators and the rotor with rotational rainbow resonators are considered. Similarly to the case with translational resonators, the deflected shapes are shown at specific frequencies, highlighting the interaction between resonators and rotor. For the case with rainbow resonators, it can also be seen that the resonators at the edge are excited at the side frequencies and the resonators at the middle span are excited at the center of the attenuation band, following the resonators mistuning of the gradient profile. The modes at frequencies lower than the bandgap show the metastructure excited at its acoustic modes, while the the response at higher frequencies reveals the metastructure's optical modes.

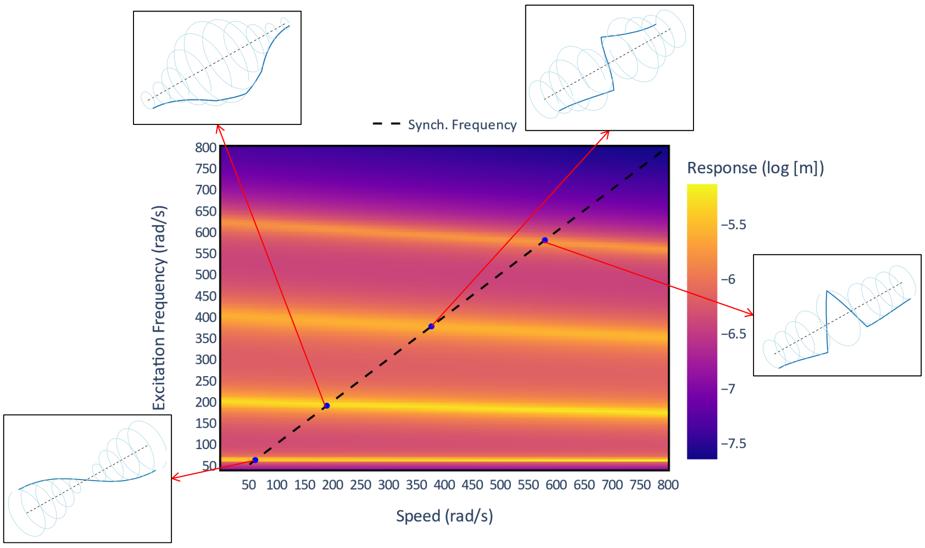

(a) Bare rotor.

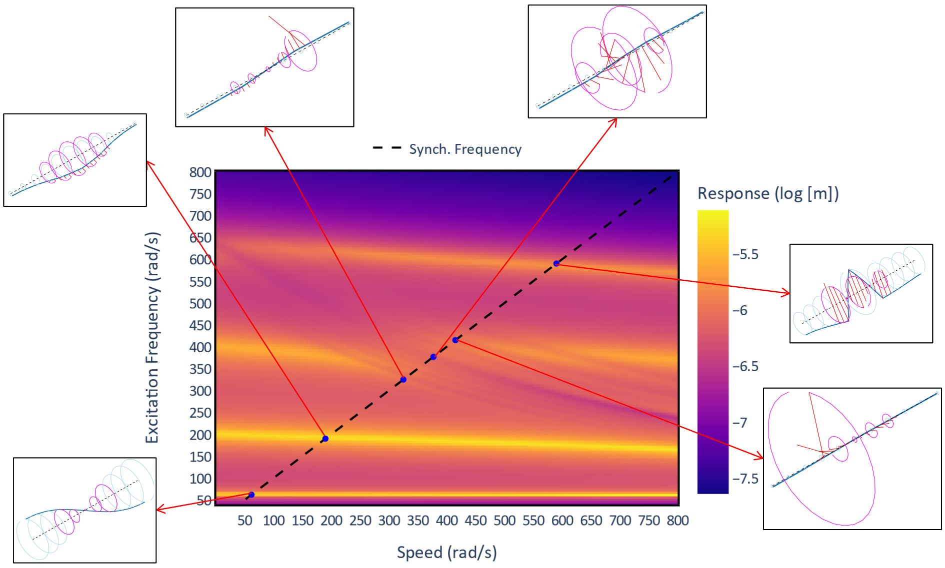

(b) rotational rainbow resonators.

Figure 4.12 – Response amplitudes as a function of the frequency and rotation speed of the shaft due to backward excitation.

Figures 4.13 and 4.14 show the deflected shape of the rotor and the rainbow resonators at different rotation speeds for forward and backward excitation, respectively. Figure 4.13 highlights that the resonator modes are not excited for the forward excitation. Moreover, the deflected shapes are very similar for the bare rotor, with effectively no attenuation. However, in Figure 4.14, it is clear that the modes of the resonators are excited at the bandgap region and that they provide a large attenuation effect compared to the deflected shapes. Moreover, it is evident that the gradient profile is excited differently at each rotation speed. This is similar to the results found for the translational resonators.

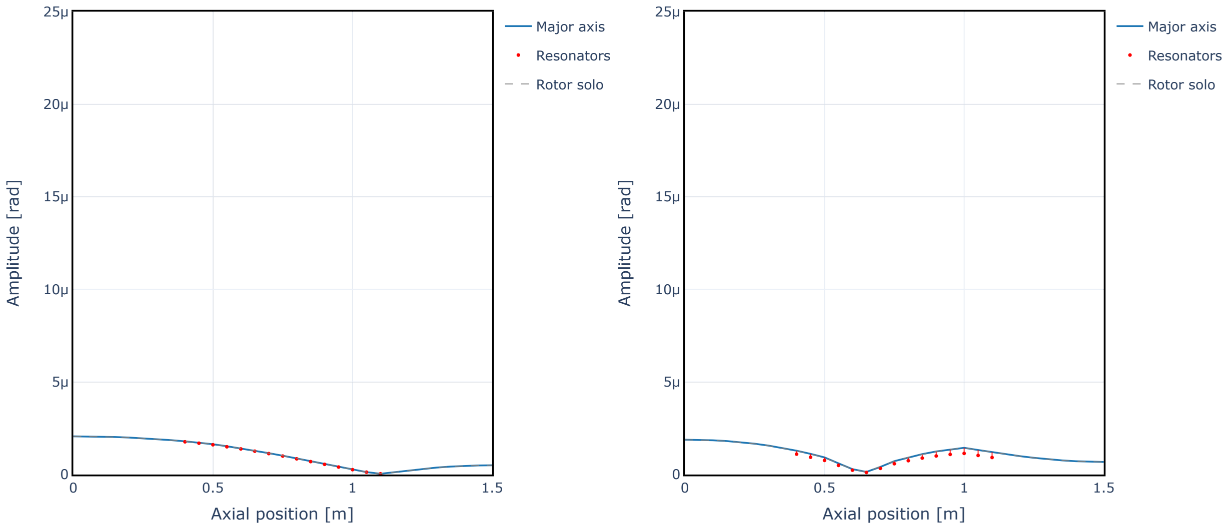

(a) $\Omega = 100 rad/s$ (b) $\Omega = 340 rad/s$

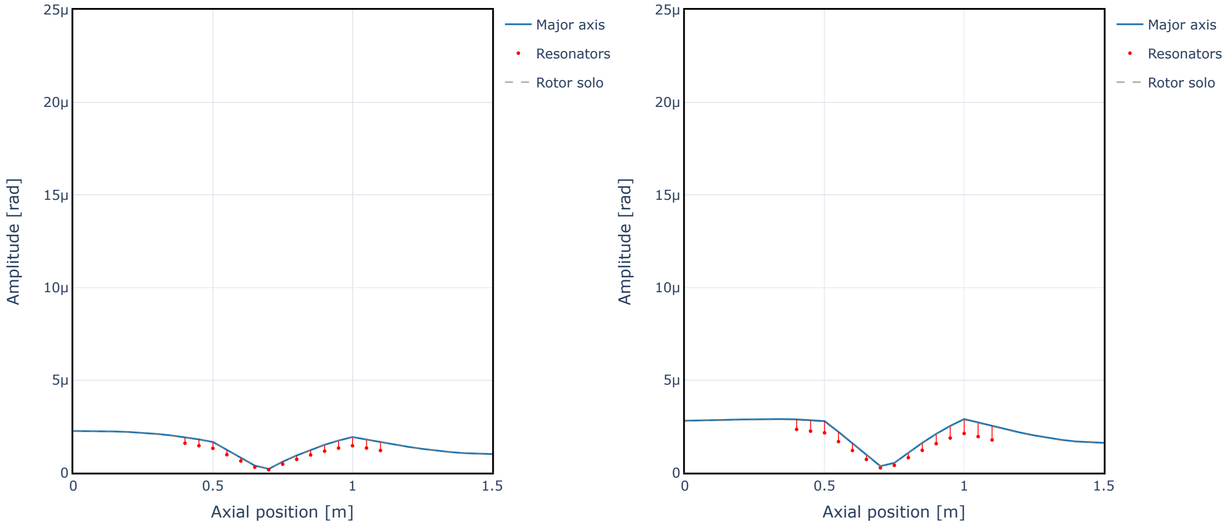

(c) $\Omega = 375 rad/s$ (d) $\Omega = 400 rad/s$

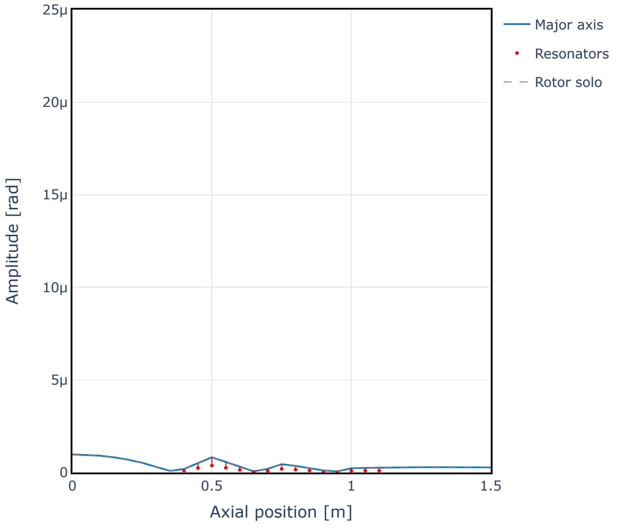

(e) $\Omega = 800 rad/s$

Figure 4.13 – Deflected shapes for rotational rainbow resonators tuned to $634.4 rad/s$ with forward excitation.

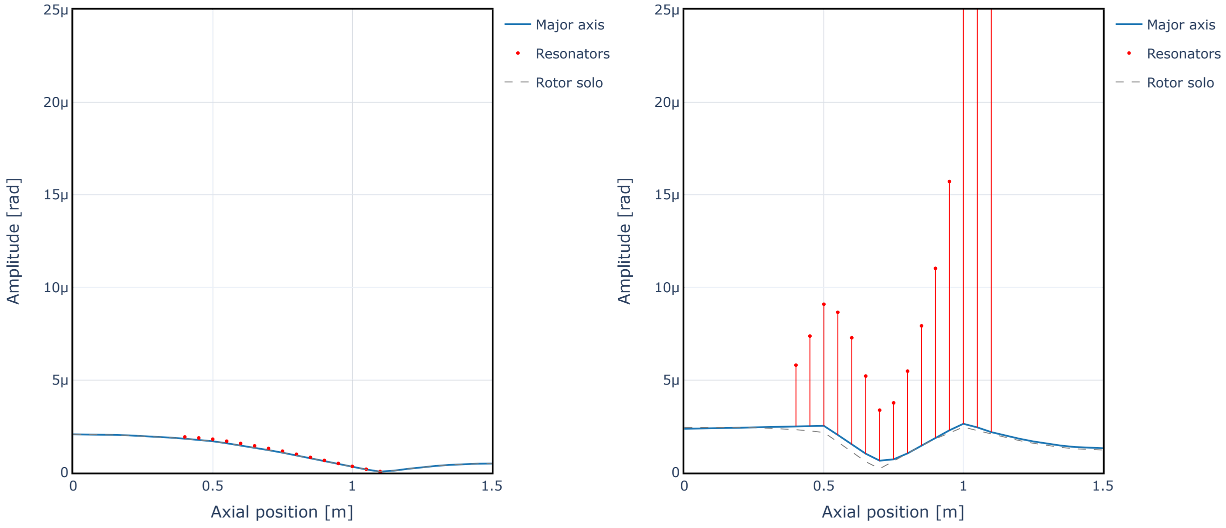

(a) $\Omega = 100rad/s$ (b) $\Omega = 340rad/s$

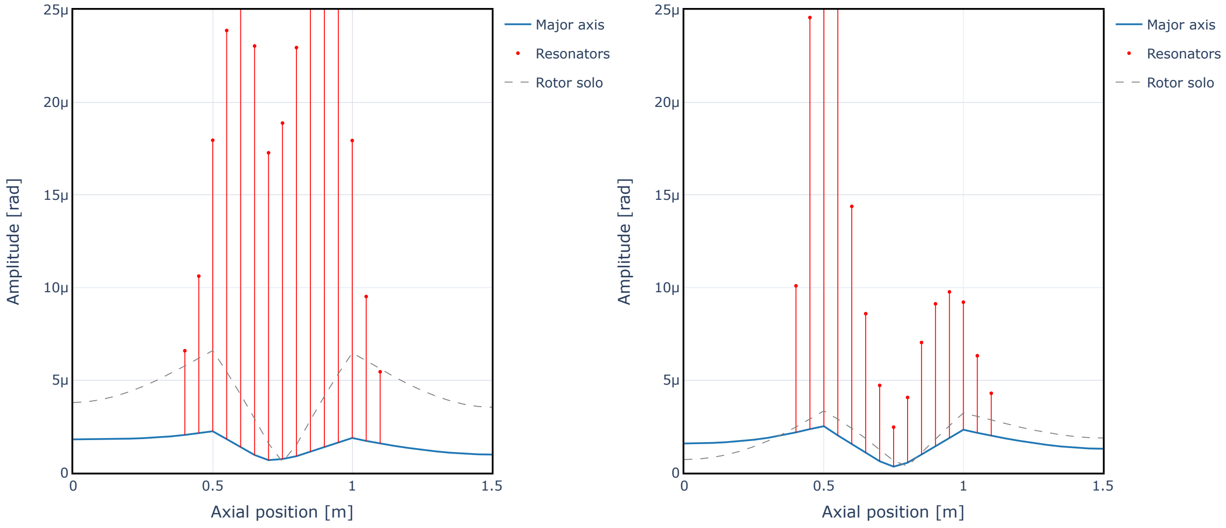

(c) $\Omega = 375rad/s$ (d) $\Omega = 400rad/s$

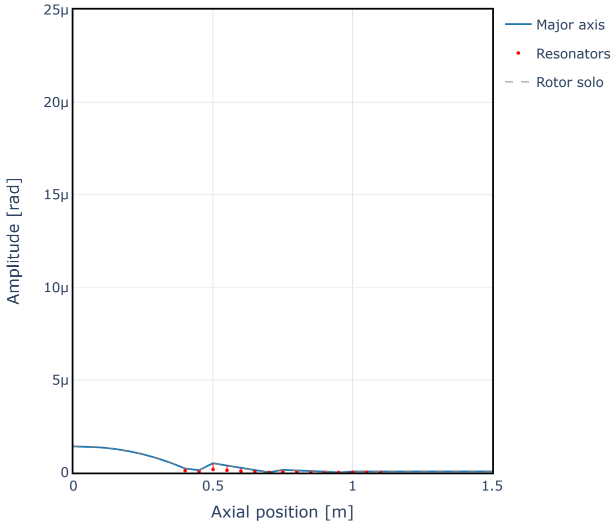

(e) $\Omega = 800rad/s$

Figure 4.14 – Deflected shapes for rotational rainbow resonators tuned to 634.4 rad/s with backward excitation.

Figure 4.15 shows the spatially averaged amplification factor A_{avg} and phase angle ϕ_{avg}, applying the definition of Equations 4.6 and 4.7 to the deflected shapes obtained from backward excitation instead of the eigenvectors, as previously presented. It is clear that the amplification factor follows the branch related to the rotational resonators with a sharp change for the periodic metastructure configuration. In the case of rainbow resonators arrangement, a smoother transition is observed given the several branches created by this configuration for both A_{avg} and ϕ_{avg}. Similar behavior can be observed in Figure 4.16 for the forward excitation case, with the amplification and phase shift regions following the forward modes in this case.

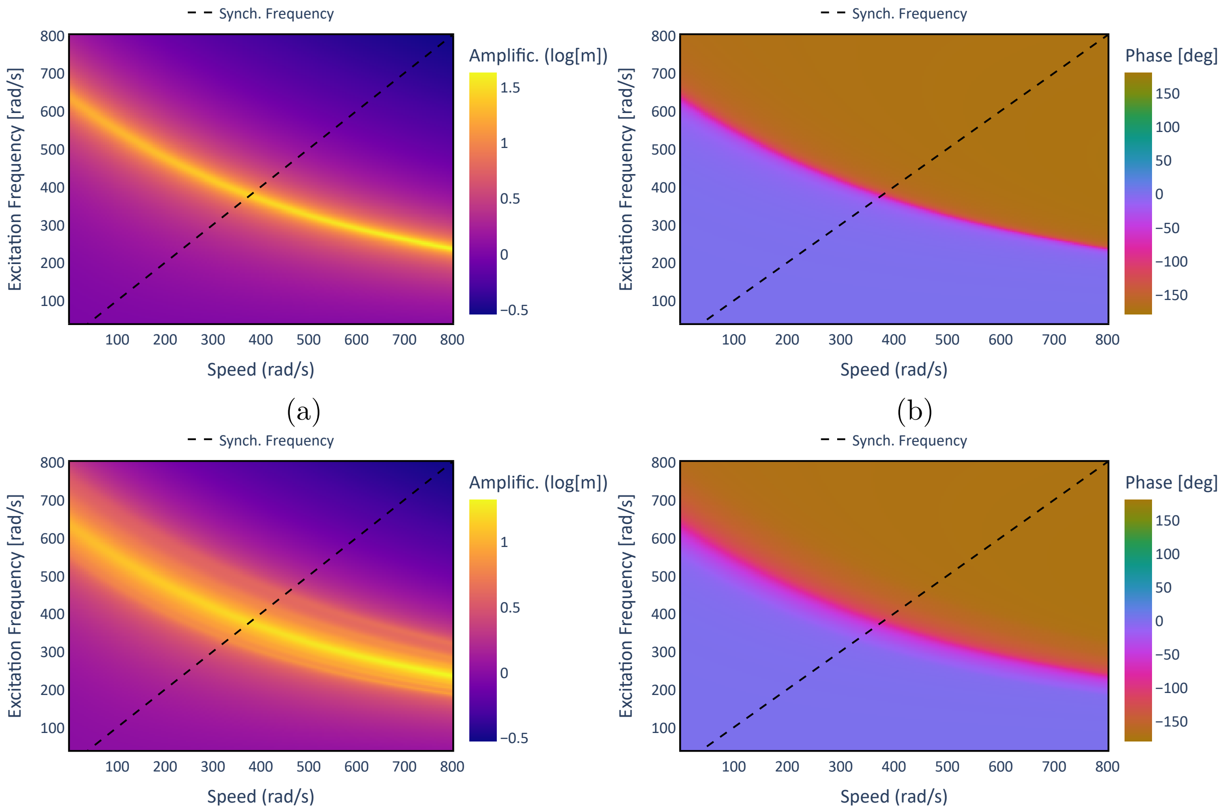

(a) (b)

(c) (d)

Figure 4.15 – Spatially averaged amplification and phase angle with rotational resonators tuned to 634.4 rad/s subject to backward excitation. (a) Periodic resonators and A_{avg} colorscale. (b) Periodic resonators and ϕ_{avg} colorscale. (c) Rainbow resonators and A_{avg} colorscale. (d) Rainbow resonators and ϕ_{avg} colorscale.

Summarizing, the results presented in this section reveal that, on the frequency range of interest, only the backward vibration is affected by the rotational resonators, while the forward whirl behavior remains unaffected when the excitation is applied. The resonators are then unaffected by forward excitation, while they can strongly restrict the vibration transmissibility with backward excitations. The opposite result can be achieved by tuning the forward mode of the resonators to a specific desired frequency.

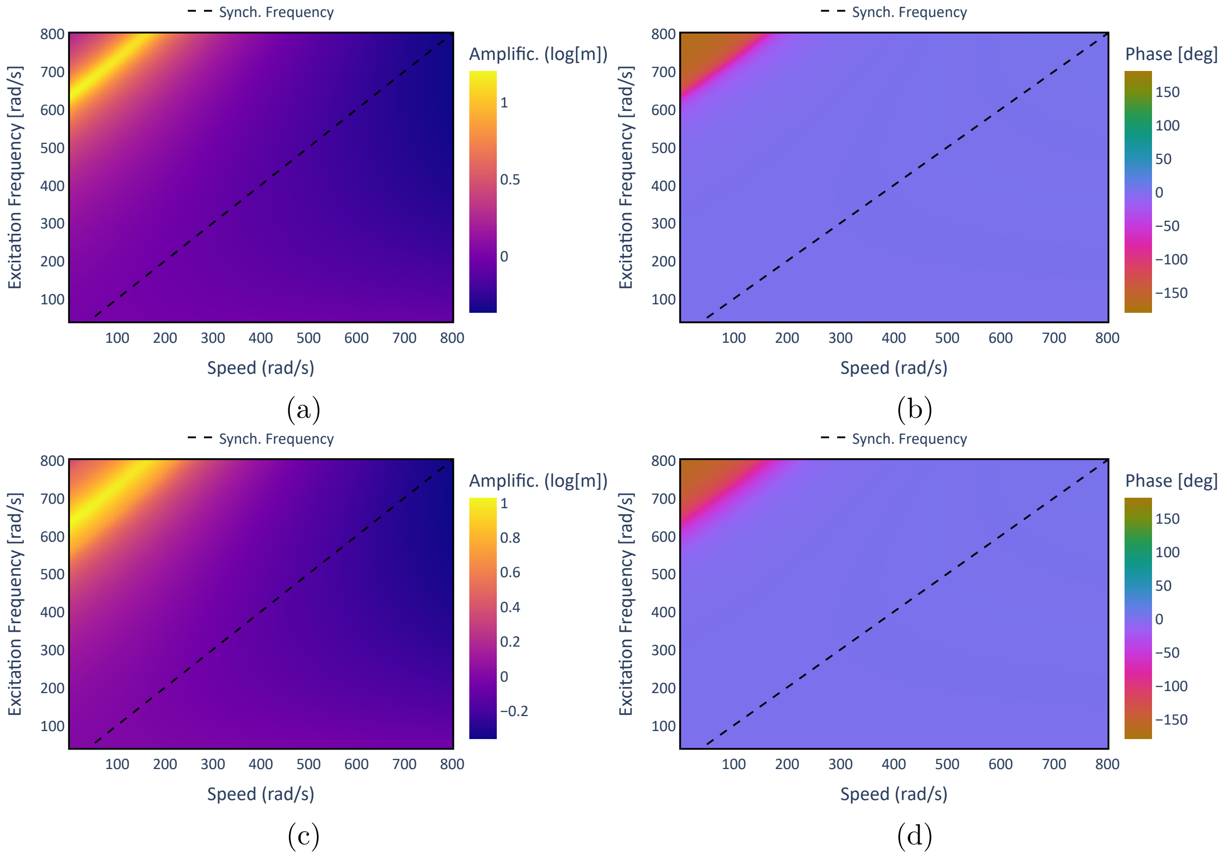

(a) (b) (c) (d)

Figure 4.16 – Spatially averaged amplification and phase angle with rotational resonators tuned to 634.4 rad/s subject to forward excitation. (a) Periodic resonators and A_{avg} colorscale. (b) Periodic resonators and ϕ_{avg} colorscale. (c) Rainbow resonators and A_{avg} colorscale. (d) Rainbow resonators and ϕ_{avg} colorscale.

4.2 Turboexpander Application

One of the most important challenges for the application of metastructures to industrial rotating machinery lies in the fact that the free space around the rotor is rarely available in such equipment. Industrial compressors and pumps are usually designed to be as compact as possible, leaning towards the most cost-effective and energy efficient solutions.

However, some exceptions may be good potential candidates for an initial proof of concept. Turboexpanders and pinion rotors of integrally-geared compressors are some examples. These types of machines have their flow elements mounted on the shaft ends instead of on the midspan. This usually leaves some room for additional components to be mounted on the shaft and allowed to freely move in the radial direction. In the case of integrally geared machines, this space is still somewhat limited due to the gear, which usually locates in the shaft center. However, in turboexpanders, the central portion of the shaft is often free of major functional components.

To explore this concept and provide some insight into how an application of this concept to a real machine could look like, a typical model of a turboexpander will be

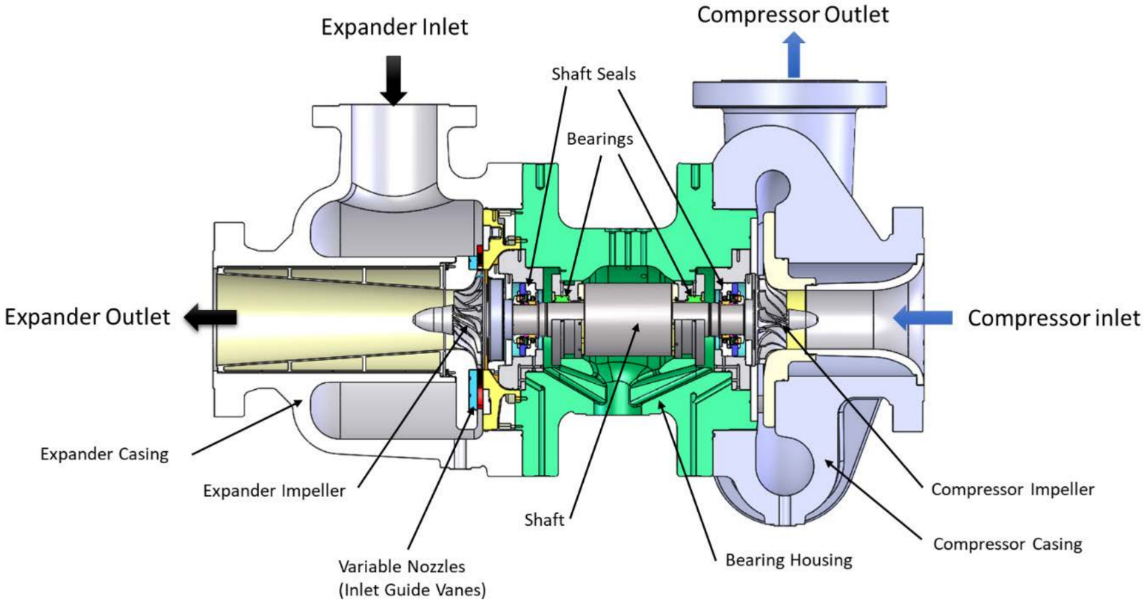

Figure 4.17 – Typical turboexpander-compressor showing key parts (API Std 617, 2022). Reproduced courtesy of the American Petroleum Institute.

used. Figure 4.17 presents a cross-sectional schematic drawing of a typical turboexpander-compressor with its key parts indicated.

Figure 4.18 shows the rotor model built on Ross. The components in red are the parts that are mounted on the shaft, modeled as lumped inertia elements, and the blue elements represent the linear resonators located on the free midspan portion of the shaft. The large spring-damper elements represent the radial bearings. The smaller elements located at the ends of the shaft are concentrated cross-coupling stiffness elements that were imposed to represent the impellers' destabilizing forces. A fixed value of 1.2×10^6 N/m pure cross-coupling was applied, which is a value around 10 times lower than the radial bearings direct stiffness components, which is typical for this type of high speed machine.

The bearings were modeled as tilting pad oil-lubricated bearings using MAXBRG software (HE, 2003) considering the geometry and oil parameters shown in Table 2. Geometric parameters represent typical values for a lightweight, high speed machine. The bearing loads for both bearings were considered equal for simplicity, considering that each would have slightly asymmetric load distributions due to a combination of gravity and impeller pressure profile.

Journal Diameter	44.45 mm	N^o of pads	4
Diametral clearance	0.111 mm	Pivot arrangement	Load between pads
Pad arc length	72 °	Pad axial length	19.1 mm
Pad thickness	10 mm	Pivot type	Rocker back
Pad preload	0.25	Pad offset	0.5
Oil type	ISO VG 32	Oil supply temp.	45 °C
Pad material	316 SS	Bearing load	455 N

Table 2 – Radial bearing input data for calculation of dynamic force coefficients.

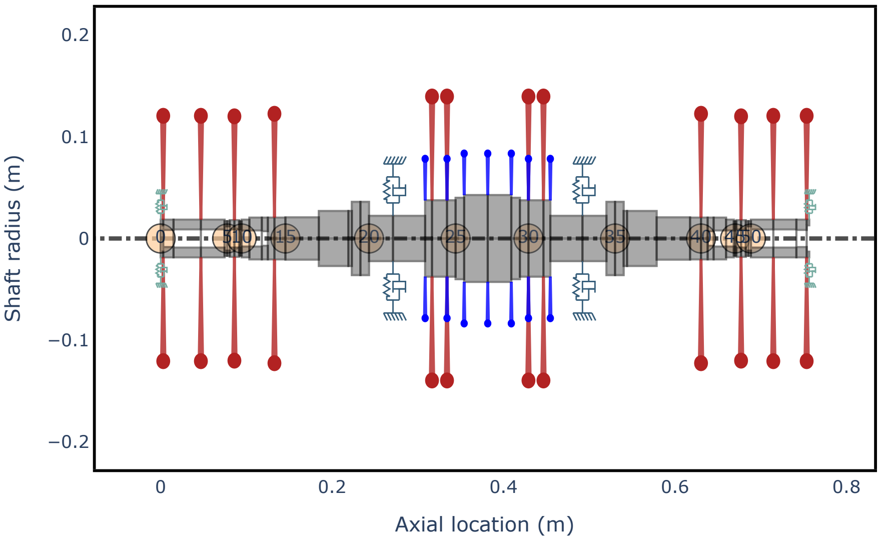

Figure 4.18 – Turboexpander compressor rotor model.

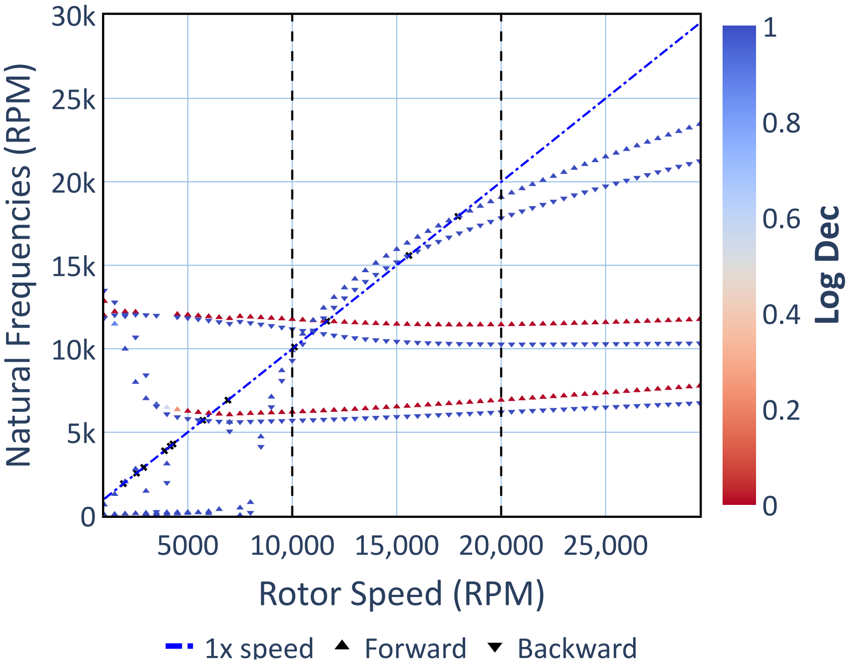

Figure 4.19 – Campbell diagram of the turboexpander-compressor before application of resonators.

The operating speed range of the turboexpander was evaluated between 10,000 and 20,000 rpm, which is typical for this type of machinery. The Campbell diagram for the rotor's original design, without resonators, is presented in Figure 4.19. It reveals three potentially harmful critical speeds at 5,715 rpm, 11,652 rpm, and 17,929 rpm. It is important to note that these critical speeds correspond to forward whirling natural frequencies, which can be significantly amplified by any unbalance forces.

The lowest critical speed is outside the operating speed range, with a separation margin of more than 70%. According to API Std 617, this critical speed would still have to be subjected to a stability analysis. However, this step will not be explored in this work because it would not be directly related to the application of the metastructure concept.

The second and third lowest critical speeds are within the operating speed range, and thus will have to be evaluated to ensure that their effects would not create harmful vibrations during the turboexpander operation. In further investigation of the modal parameters, it was possible to determine that the second critical speed has a damping ratio of 0.001, while the damping ratio of the third critical speed is 0.51, i.e., it has a negligible contribution to turboexpander vibration.

The high damping ratio of the third critical speed translates into an Amplification Factor (AF) of 0.98, significantly lower than the API Std 617 limit of 2.5 for considering it as a concern for rotor response amplification. Therefore, this critical speed may be ignored even if it is located within the operating speed range.

However, the second critical speed presents a strong potential for rotordynamic instability, with strong amplification - $AF > 300$. This means that, in the engineering design process of this machine, this critical speed would have to be addressed somehow. The following discussions will explore the concept of using linear periodic and graded resonators to achieve the neutralization of this specific critical speed. For this example, only translational resonators are applied. Table 3 shows the design parameters of the resonators.

Inner diameter	90 mm	Outer diameter	150 mm
Thickness	15 mm	Mass	1.32 kg

Table 3 – Resonator parameters.

To correctly tune the resonators to attenuate the desired critical speed, it is necessary to first consider the impact the added inertia to the bare turboexpander rotor. For this purpose, a new Campbell Diagram is built for the original rotor with incorporated resonators as added inertia elements. The result is shown in Figure 4.20. The addition of resonators has slightly shifted the second and third natural frequencies, and now the critical speed that presents low damping characteristics is located at $12,094$ rpm with a damping ratio of 0.03. Although a significant increase in damping ratio has been observed after the addition of the disks, the critical speed is still a concern, since it still has $AF = 16.6$ and is located within the operating speed range. Furthermore, one should note that the increase in damping ratio cannot be directly attributed to the addition of the disks, but to the underlying change in mode shape that allows a more efficient activation of the radial bearings damping properties.

The resonators are then tuned to the frequency of $12,094$ rpm, using only its translational DoFs. To evaluate the attenuation performance of the final metastructure configuration, two separate excitation conditions are considered:

1. Midspan unbalance, $4U$ unbalance magnitude.

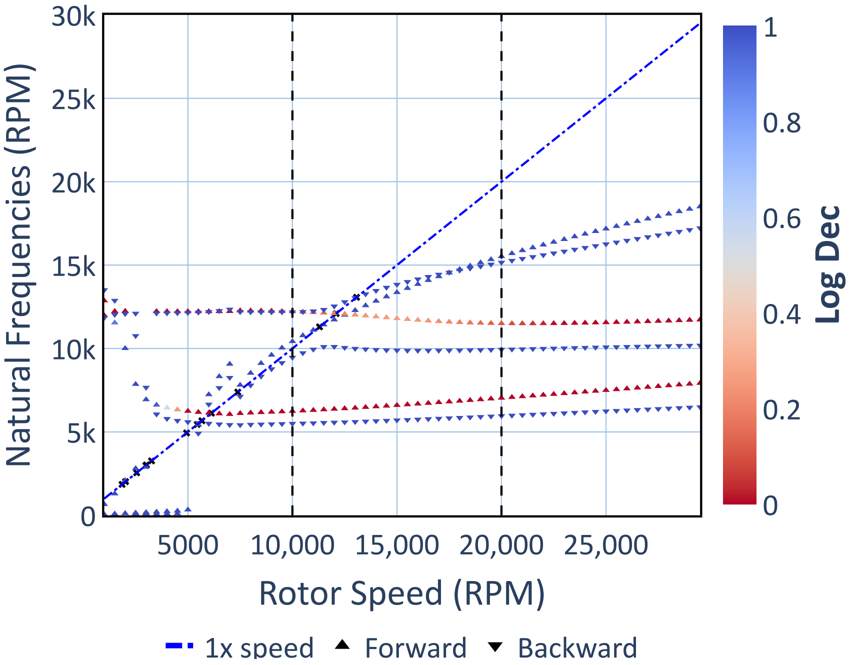

Figure 4.20 – Campbell diagram of the turboexpander-compressor before application of resonators.

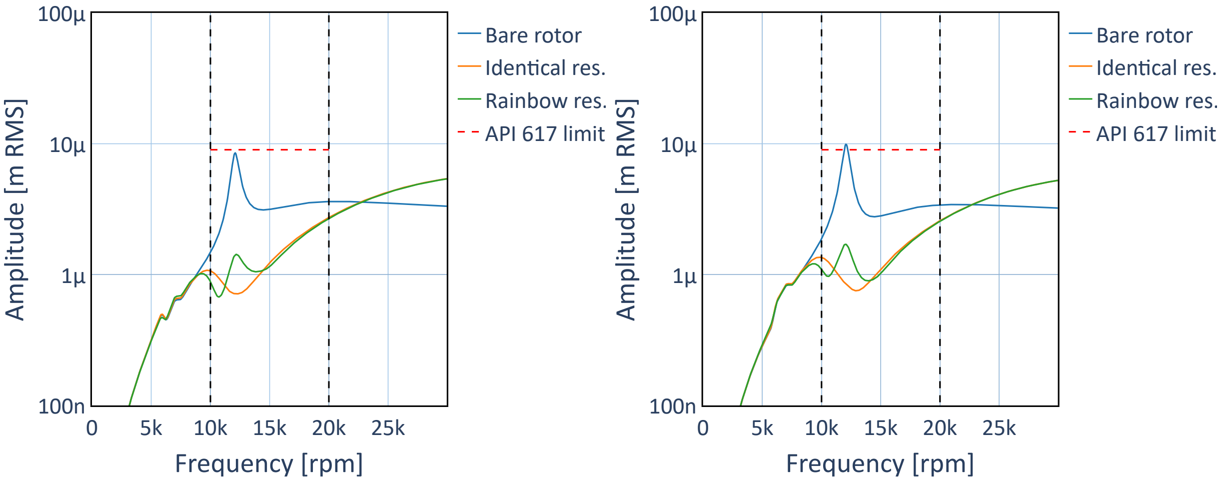

(a)

(b)

Figure 4.21 – Unbalance responses plots for turboexpander compressor with midspan unbalance. (a) Left side bearing and (b) right side bearing.

2. Rotor impeller unbalance, $4U$ unbalance magnitude.

The unbalance magnitude is defined in terms of U, which is the maximum allowable residual rotor unbalance as defined in API Std 617.

Figure 4.21 shows the vibration results at the bearing nodes for 3 cases: without resonators, with periodic resonators, and with rainbow resonators. The rainbow distribution was applied following the expression of Eq. 4.5 with $m = 1$. Only the X-direction amplitude is shown, since the system's isotropy results in similar amplitude in orthogonal directions.

The vibrations of the bare rotor, while still showing amplitude levels below the allowable limits of API Std 617, still indicates the clear presence of a lightly damped

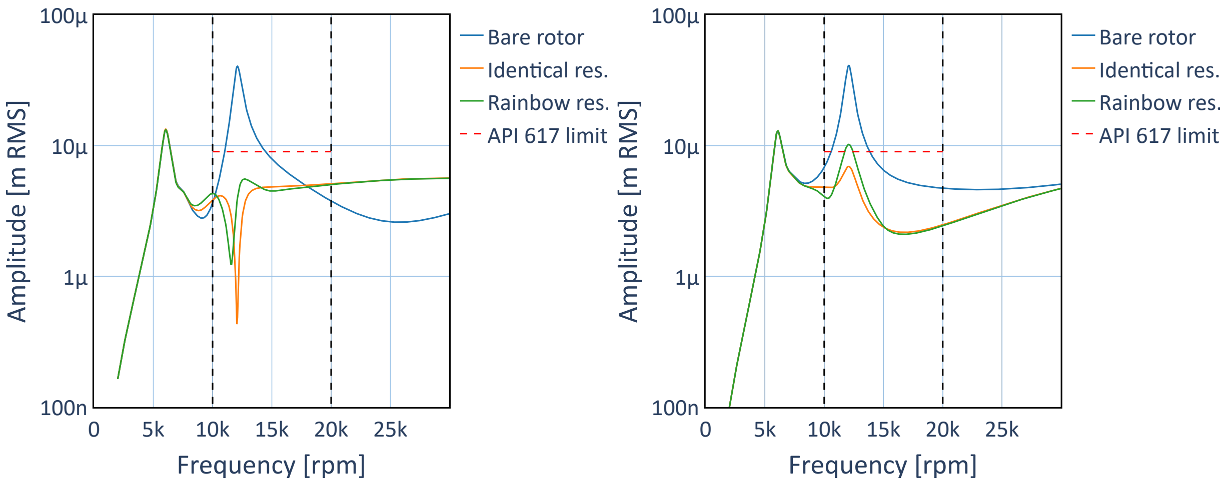

(a) (b)

Figure 4.22 – Unbalance responses plots for turboexpander compressor with left side impeller unbalance. (a) Left side bearing and (b) right side bearing.

critical speed within the operating speed range, which would incur in an unacceptable rotordynamic design. With the addition of the linear resonators, this critical speed is neutralized, with a substantial reduction in overall vibration amplitudes. The periodic resonators show a slightly narrower attenuation range, but provide a more consistent attenuation performance across the entire operating speed range if compared to the rainbow arrangement.

Figure 4.22 shows the vibration results at the bearing nodes for the same 3 cases. In this case, the excitation of the lowest critical speed is clearly visible around 6000 rpm, but outside the operating range. The second lowest natural frequency also shows a stronger response, going over the API Std 617 allowable amplitudes. With the addition of the linear resonators, a dramatic decrease in vibration amplitudes is observed in both responses. The rainbow resonators arrangement, however, still would not comply with the allowable vibration requirements.

Therefore, in this case, the periodic arrangement of linear resonators would be a preferable option to control the effects of the second critical speed within the operating speed range when compared to the rainbow arrangement. This is mainly due to the fact that the places available for the addition of resonators are not the optimal locations to attenuate the second critical speed.

Figure 4.23 shows a 2-D representation of the mode shape of the target natural frequency, from which it becomes clear that the resonators are placed at nodes with relatively little modal activation. Therefore, the spatial distribution of the resonators is not optimized (MENG et al., 2020c), which leads to limited attenuation performance of the resonator. Consequently, the attenuation magnitude plays a more important role than the attenuation bandwidth in this specific case, which makes the identical resonators a more adequate choice.

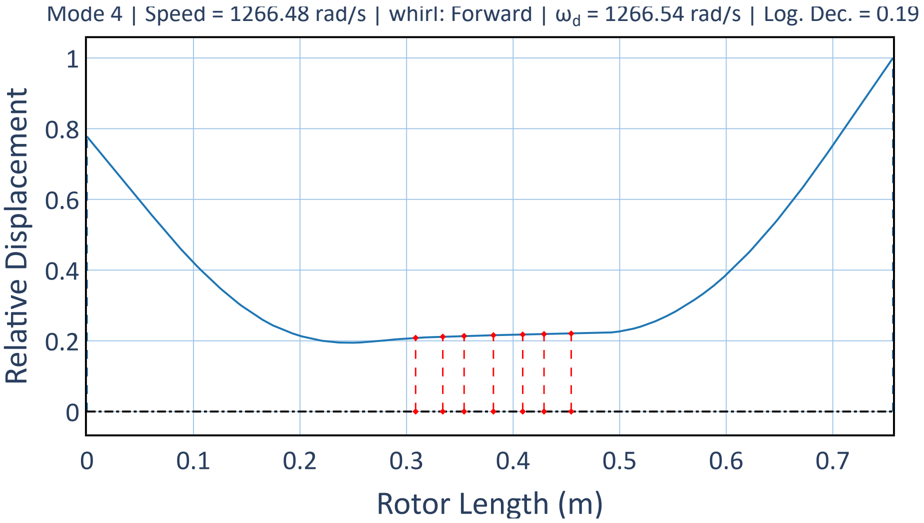

Figure 4.23 – Mode shape of the target natural frequency. Red dashed lines indicate the position of the resonators.

Stepping beyond the standard industry practices for rotodynamic design, we can assess the system's behavior from a broader perspective. By evaluating the system's nonsynchronous response, the behavior of its natural frequencies in different rotating speeds is observable. A purely forward excitation with 1 N amplitude was applied to the left side impeller and the following analyzes were obtained from the response to the right side impeller.

Figure 4.24 compares the response heatmaps of the bare rotor with the cases with identical and rainbow resonators. As expected, the vibration attenuation effect goes beyond the synchronous region shown in Figures 4.22 and 4.21. The high amplification lines in Figure 4.24a match the natural frequency lines of Figure 4.20. These lines appear strongly attenuated in a wide frequency range in Figures 4.24b and 4.24c. This indicates that the resonators have a wide damping-like effect on the rotor natural frequencies, which can be a useful tool for adding damping to the rotor in this type of machine.

A similar result is presented in Figure 4.25, but with a backward excitation. The backward modes are clearly strongly damped to begin with, as is usual in rotating machines with dominant sources of cross-coupling. This type of destabilizing forces are usually related to aerodynamic phenomena generated by the machine's rotation and, as such, tend to destabilize the forward modes while stabilizing the backward modes (MUSZYNSKA, 2005). Therefore, in this case, the resonators have no significant effect and actually seem to slightly increase the system's response for some conditions. However, this is not a concern since the backward modes are seldom regarded as a concern in engineering applications.

To provide a parallel with the results shown in section 4.1.2, the averaged amplification and phase maps are shown for the turboexpander model in Figure 4.26. A similar behavior is observed, with a visible widening of the frequency range in which the resonators are more strongly activated. It can be seen that the translational resonators attenuation band is not affected by the rotation speed. This effect is expected, as discussed

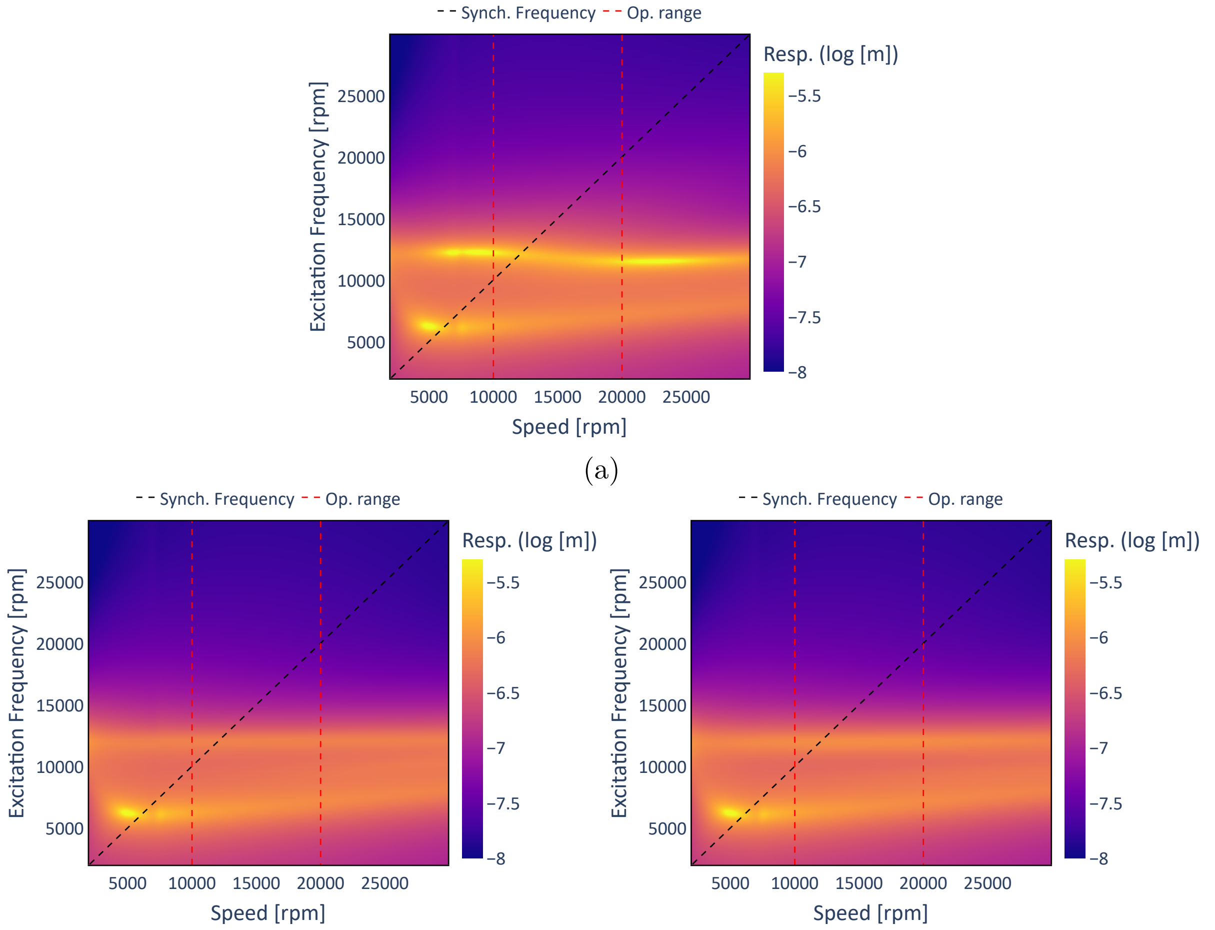

(a)

(b)

(c)

Figure 4.24 – Response heatmap for unitary forward excitation. (a) Bare rotor, (b) rotor with identical resonators and (c) rainbow resonators.

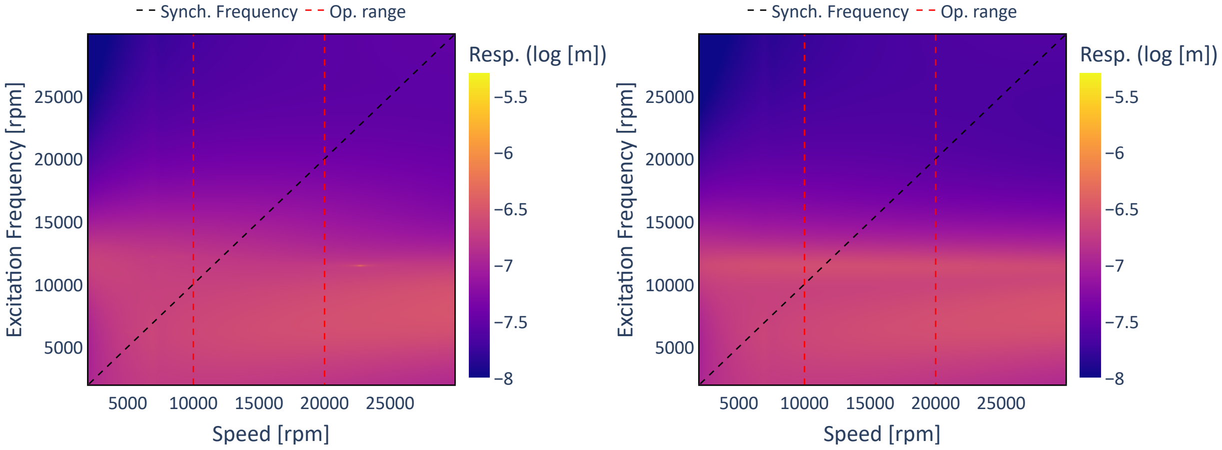

(a)

(b)

Figure 4.25 – Response heatmap for unitary backward excitation. (a) Bare rotor and (b) rotor with identical resonators.

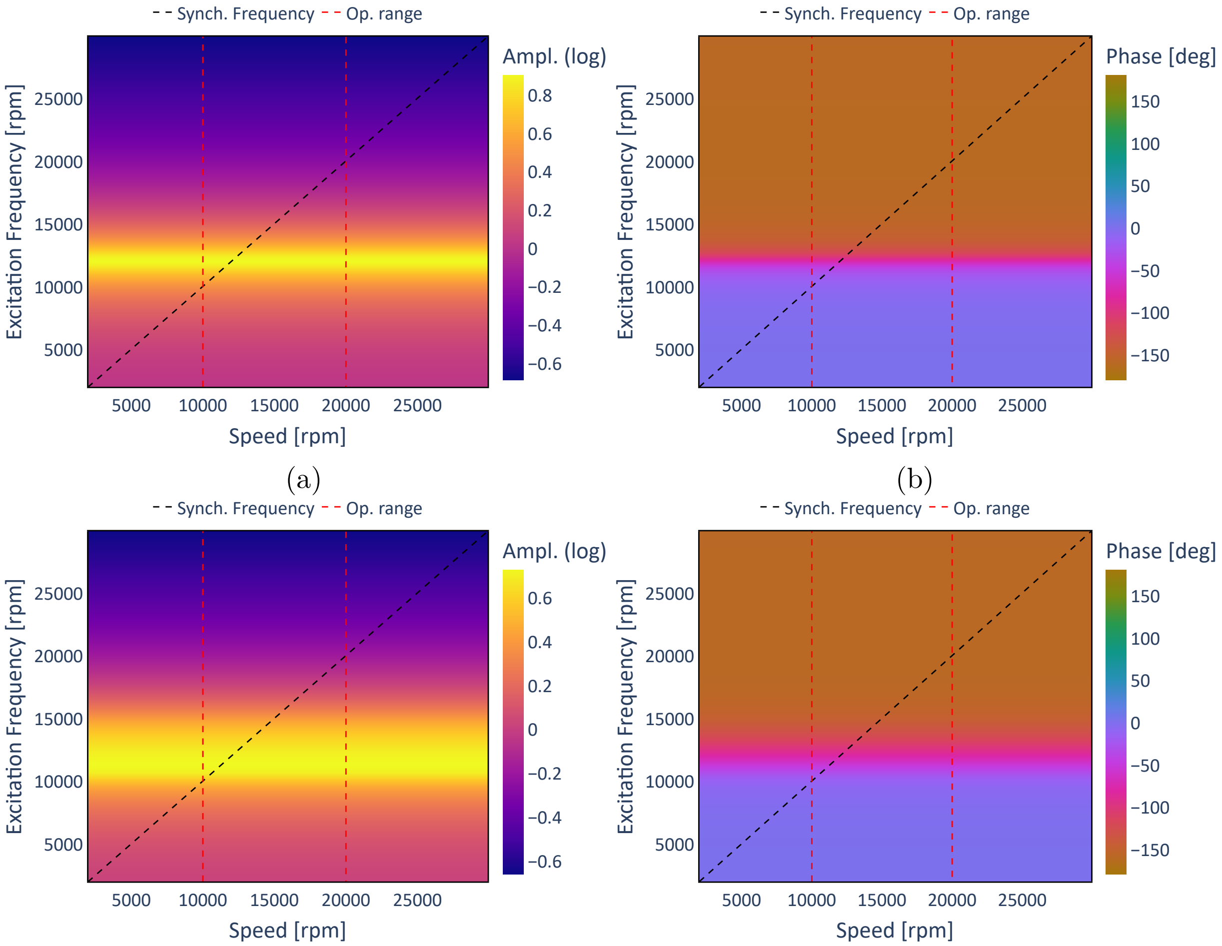

(a) (b) (c) (d)

Figure 4.26 – Averaged amplification and phase angle maps for identical (a-b) and rainbow resonators (c-d).

and demonstrated in previous sections, because the translational resonators' dynamics is unaffected by the gyroscopic effects.

4.3 Final Remarks

This chapter investigated the extension of periodic locally resonant metastructures to rotors in an effort to explore their potential vibration attenuation capabilities and particular phenomena associated with rotating motion. Two different resonator configurations were used for this purpose: translational and rotational resonators.

The highlights and main findings are summarized below.

- Translational resonators provide strong attenuation of both the backward and forward modes.
- Rotational resonators require tuning to a specific whirl direction, either forward or backward, providing vibration attenuation for one of them.

- In both cases, the mass gradation of the resonators provided a significant widening of the attenuation bandwidth.
- Polarization phenomenon was found for the rotational resonator case, as the resonators, tuned to the backward whirl modes, were invisible to forward excitations close to the tuning frequency range.
- The coexistence of acoustic and optical modes was observed in certain frequency ranges for rotation resonators.
- Spatially averaged amplification and phase angle maps were proposed and applied as a useful tool for visual interpretation of the overall behavior of the system.
- The application of translational resonators to a real turbomachinery model demonstrated that the concept can be a powerful design tool for rotors with low damping.

These initial findings provide an exciting and promising doorway to the potential applications and particular phenomena that can be unraveled in further exploration of rotational metastructures. The following chapter will provide further insight by gradually introducing new aspects with increasing complexity in the evaluations.

5 Bandgap formation and chaos in periodic lattices with graded bi-stable resonators

In this chapter, a second step is taken in building the thesis concept. Here we explore the nonlinear phenomena and chaotic behavior as a vibration attenuation performance enhancer for periodic structures. For this purpose, we present an arrangement of a 1-D periodic lattice with bi-stable Duffing oscillator attachments, showing the effects of excitation magnitude and mass gradation on the bandgap. An investigation of the bandgap formation mechanisms considering energy and spectral approaches is also developed. This simple arrangement allows us to thoroughly investigate and understand the mechanisms involved in nonlinear bandgap formation.

5.1 System Description

The schematic drawing shown in Figure 5.1 depicts the periodic chain N_0 DOF 1-D with periodically attached nonlinear resonators considered in this study. The mass of each resonator is represented by $m_n = m_0$, $n = 1..N_1$, being m_0 a reference mass value. The linear elastic elements that connect the chain elements are identical, with stiffness k_0, and are also considered a linear viscous damping c_0 between each element.

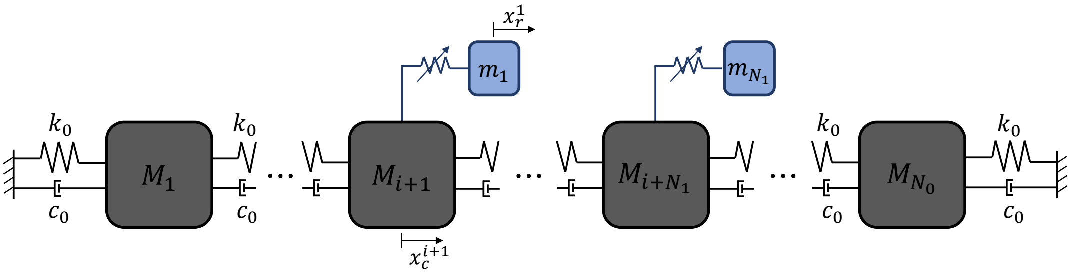

Figure 5.1 – 1-D chain arrangement used for the simulations in this chapter.

The system's equation of motion in homogeneous form can be described as

$$[\mathbf{M}]\ddot{\mathbf{x}} + [\mathbf{C}]\dot{\mathbf{x}} + [\mathbf{K}]\mathbf{x} + \mathbf{f}_{nl}(\mathbf{x}) = 0 \qquad ; \qquad \mathbf{x} = \begin{Bmatrix} \mathbf{x}_c \\ \mathbf{x}_r \end{Bmatrix}, \tag{5.1}$$

in which $[\mathbf{M}]$, $[\mathbf{C}]$ and $[\mathbf{K}]$ are the system's linear mass, damping, and stiffness matrices, respectively, $\mathbf{f}_{nl}(\mathbf{x})$ is a vector representing the nonlinear effects, and $\mathbf{x}_c$ and $\mathbf{x}_r$ are the displacement vectors for the chain and resonators, respectively.

The behavior of nonlinear resonators, composed of a lumped mass and a nonlinear elastic element, is described by the Duffing equation (KANAMARU, 2008). This type of oscillator is one of the most widely used in studies of nonlinear mechanical structures due to its mathematical simplicity and richness in dynamic behavior. Another advantage of this oscillator is that it can be reproduced in real experimental setups, as shown in recent works (XIA; RUZZENE; ERTURK, 2020). Thus, the equation of motion of each resonator is described by

$$m_n \ddot{x}_r^n + \delta \dot{\tilde{x}}_n + \beta \tilde{x}_n + \alpha \tilde{x}_n^3 = 0 \tag{5.2}$$

where $\tilde{x}_n = x_r^n - x_c^{i+n}$ is the relative displacement between each resonator and the chain element to which it is attached, x_r^n and x_c^{i+n} being individual components of the vectors $\mathbf{x}_r$ and $\mathbf{x}_c$. Note that the terms related to the coefficients m_n, δ and β are linear and can be included in the linear matrices described in Equation 5.1. The only nonlinear term in Equation 5.2 is $\alpha\tilde{x}_n^3$, which is included in the nonlinear force vector $\mathbf{f}_{nl}(\mathbf{x})$.

The restoring force of the conservative system is given by $F_r(x) = -\beta x - \alpha x^3$. Considering the special situation where $\beta < 0$ and $\alpha > 0$, the equation describes a bi-stable oscillator, which is the case explored in this study. From the non-zero positive root of the expression of the restoring force, we obtain the value of the stable equilibrium position $x_0 = \sqrt{\frac{-\beta}{\alpha}}$. By integrating the restoring force expression it's possible to obtain an expression for the oscillator's potential energy $U_p(x) = \frac{1}{2}\beta x^2 + \frac{1}{4}\alpha x^4$. As a result, the oscillator has 3 equilibrium conditions, two of them stable at $x = x_0$ and $x = -x_0$ - also referred to as potential wells - and the third an unstable equilibrium condition at $x = 0$.

Further exploring the restoring force expression, it is possible to calculate its derivative to obtain the value of the local linearized stiffness $k_{lin}(x_0)$ of the Duffing oscillator around its stable equilibrium position as

$$k_{lin}(x_0) = -\left.\frac{dF_r}{dx}\right|_{x_0=\sqrt{\frac{-\beta}{\alpha}}} = \left.(\beta + 3\alpha x^2)\right|_{x_0=\sqrt{\frac{-\beta}{\alpha}}} = -2\beta. \tag{5.3}$$

The linearized natural frequency of the resonators is defined in terms of the reference mass, m_0, as $\omega_0 = \sqrt{\frac{k_{lin}(x_0)}{m_0}}$, which enables one to obtain the parameters of the Duffing equation in terms of physical quantities such as $\beta = -\frac{\omega_0^2 m_0}{2}$ and $\alpha = -\frac{\beta}{x_0^2}$. Thus, it is possible to evaluate the direct comparison with an analogous purely linear resonator of stiffness $k = -2\beta$.

For the configuration with graded mass distribution, a linear gradation is applied using $f_m(m_0)$ as

$$m_n = f_m(m_0) = m_0\left(0.6\frac{n-1}{N_1-1} + 0.7\right) \quad ; \quad n = 1..N_1. \tag{5.4}$$

5.2 Results

In this section, numerical results are presented and discussed. First, the case of identical resonators is considered. Subsequently, the graded configuration is investigated. In all simulations, a 20 Degree of Freedom (DOF) chain is considered, $N_0 = 20$, with identical mass elements, $M_n = 5$ kg, and a linear stiffness coefficient of $k_0 = \frac{80}{d}kN/m$, where d is the distance between the chain elements, fixed at $d = 0.05m$. A linear viscous damping is also considered between each two consecutive elements of the chain, being $c_0 = 2 \times 10^{-4}k_0$. Concerning the resonators, the reference natural frequency is fixed at $\omega_0 = 250$ rad/s, and the dissipative term of the Duffing Equation is $\delta = -8 \times 10^{-4}\beta$. For the analysis, 10 resonators are considered, $N_1 = 10$, positioned at $i+1$, being the first resonator attached at $i+1 = 6$, each with a mass of $m_n = m_0 = 2.5kg$.

The solution to Eq. 3.50 was determined with a direct integration approach using 4th order Runge-Kutta method. The Frequency Response plots shown henceforth were obtained using HBM as a standard. A direct integration method, Runge-Kutta 4th order, is only applied when the HBM is not able to find a valid periodic solution or if the solution found is shown to be unstable.

Identical Resonators

At first, identical resonators are of concern, and a harmonic excitation is applied to the leftmost element of the chain. The frequency response for different excitation amplitudes, at 1000 N, 3000 N, 6000 N, and 9000 N, is shown in Figure 5.2 in terms of the RMS displacement of the rightmost element, opposite the point where the excitation is applied. The chain with linear resonators presents a great attenuation band between 220 rad/s and 400 rad/s. At frequency $\omega_0 = 250$, there is the maximum attenuation of the linear resonator. However, it is important to highlight that this maximum amplitude value has no practical physical meaning. As the excitation amplitude increases, the effect of the resonators' nonlinearities becomes more pronounced. Notice that for excitation amplitudes at 1000 N and 3000 N, the nonlinear resonator has the effect of degrading the attenuation performance. Furthermore, as these nonlinear effects manifest themselves with greater strength, at 6000 N and 9000 N, the chain response tends to exhibit a flat profile, with neutralization of all natural frequencies, except for the first one, i.e., there is a significant widening of the attenuation band at the cost of a great reduction of the total attenuation.

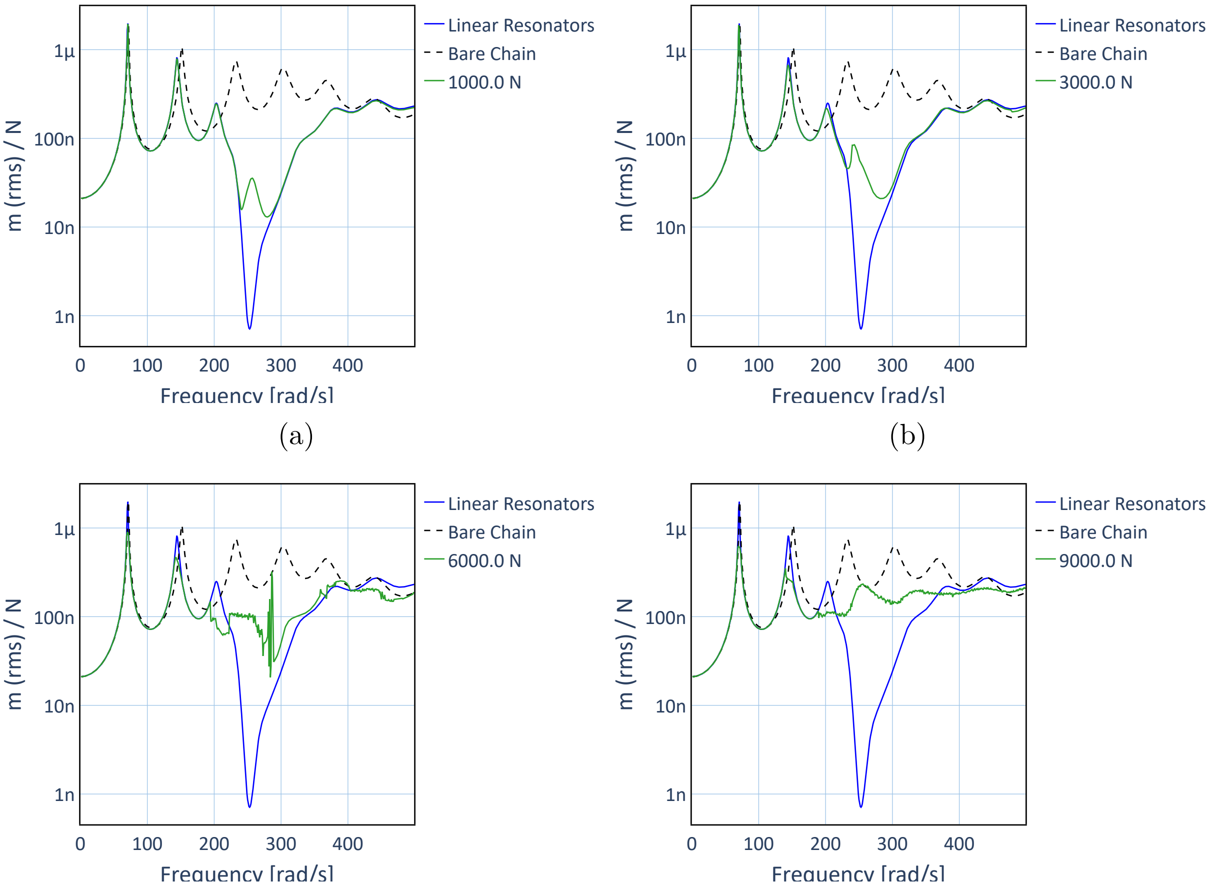

(a) (b) (c) (d)

Figure 5.2 – Frequency Response plots comparing the system's response for different excitation amplitudes: (a) 1000 N, (b) 3000 N, (c) 6000 N and (d) 9000 N.

It is possible to notice that, although the excitation applied is purely harmonic, the nonlinear system may exhibit multi-harmonic or broadband response. This is indicated in the Bifurcation Diagrams shown in Figure 5.3. These diagrams consider the displacement of the last chain element. It is clear that the broadening of the attenuation band is caused by the chaotic response of the resonators. This effect is known as energy dispersion and has been explored to achieve ultra-low and ultra-broad band attenuation in nonlinear periodic metamaterials (FANG et al., 2016; FANG et al., 2017).

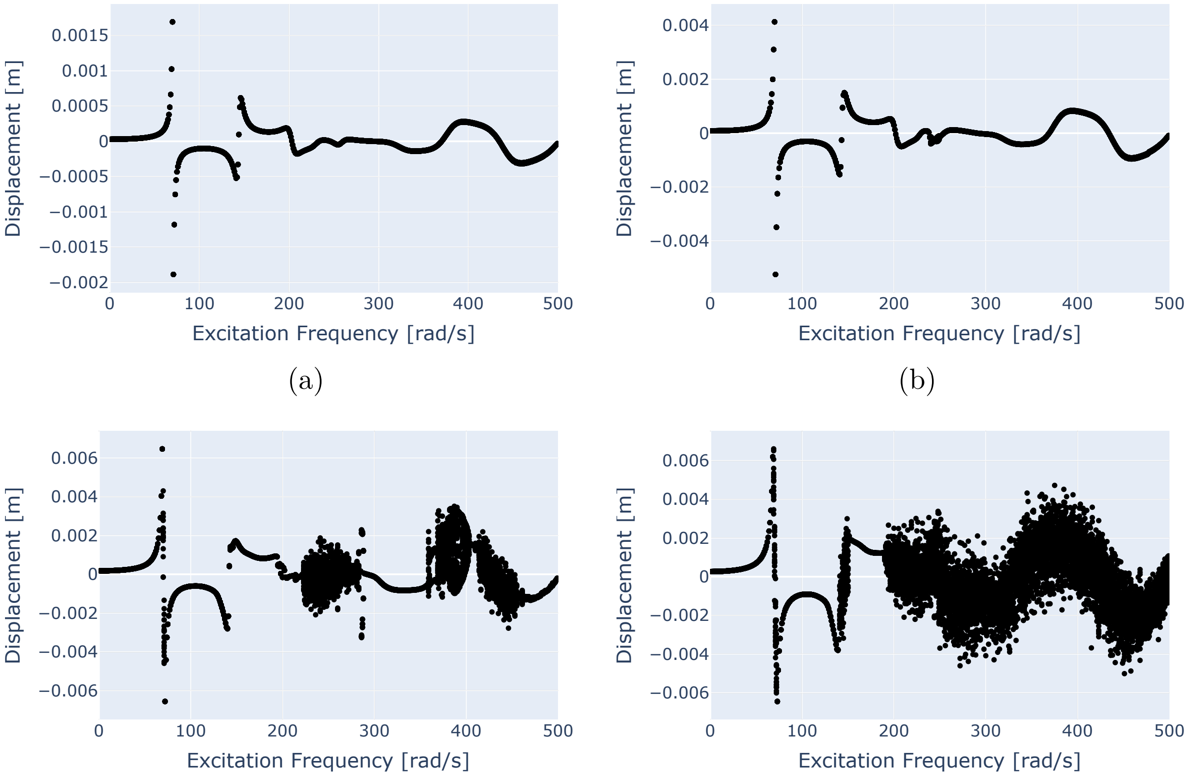

(a) (b) (c) (d)

Figure 5.3 – Bifurcation Diagrams for different excitation amplitudes: (a) 1000 N, (b) 3000 N, (c) 6000 N, (d) 9000 N.

To better understand the underlying phenomena occurring on the system, especially at the chaotic behavior, we can analyze the frequency content of the system's response. For that, the system's steady state response was considered, and the Direct Fourier Transform (DFT) was calculated for each excitation frequency condition. The results are organized in heatmaps and presented in Figure 5.4. It is possible to visualize the frequency content in the response (Y axis) as a function of the harmonic excitation frequency (X axis). Hann windowing was applied to reduce leakage effects, which can play a major role especially in the inter-harmonic spaces of periodic behavior.

Figure 5.4 shows a richer frequency distribution of the system's response as the excitation amplitude increases. For these plots, the response was obtained using the direct integration method for all cases. The spectral heatmaps make clear that different patterns of dynamic behavior emerge for different excitation conditions. In some conditions, multi-harmonic periodic behavior appears to dominate the system's response. In other frequency regions, a seemingly chaotic broadband response becomes present, where the first natural frequencies of the base chain, located between 70 and 140 Hz, seem to be constantly excited.

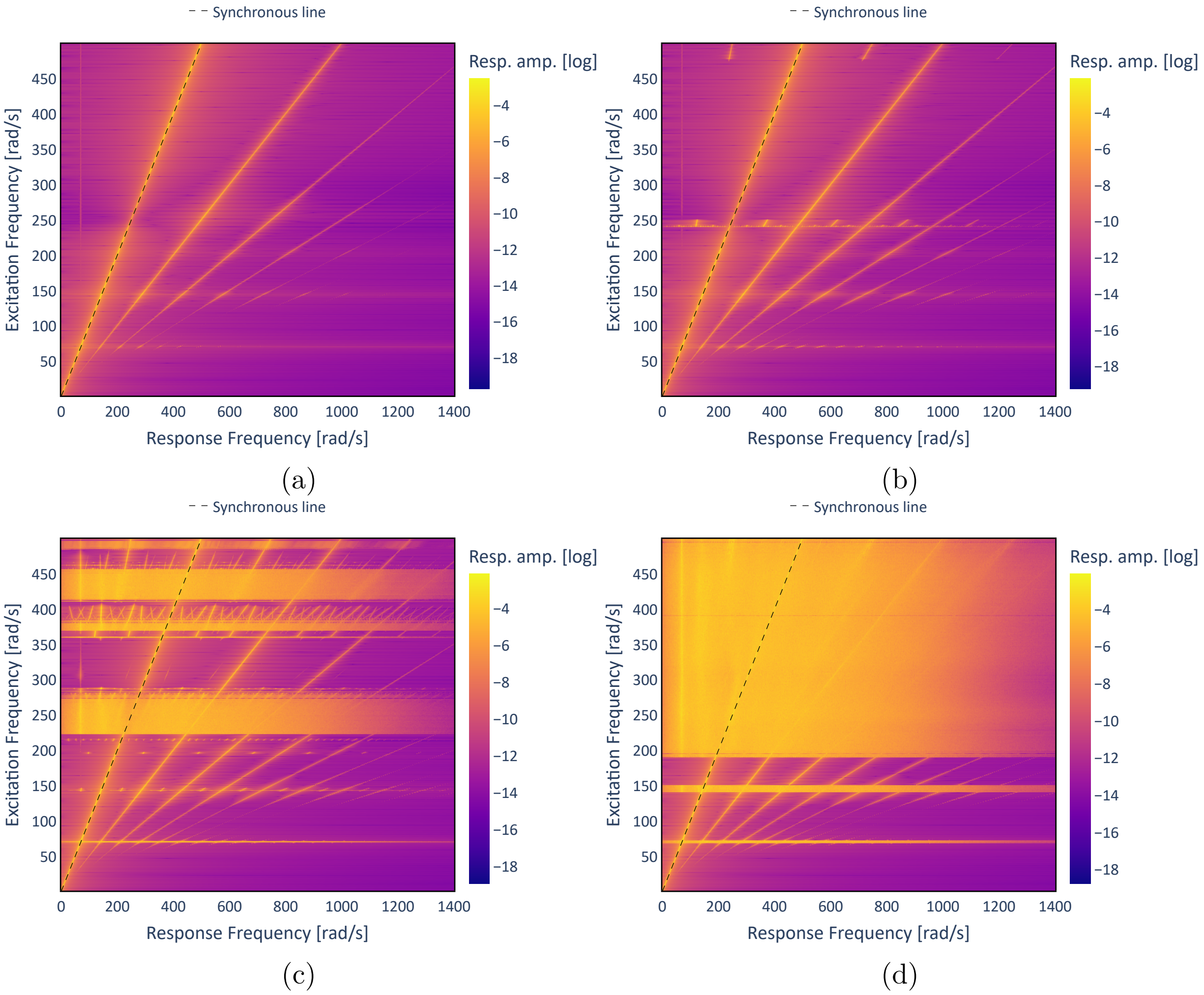

(a) (b) (c) (d)

Figure 5.4 – Frequency Response heatmap of the system for different excitation amplitudes: (a) 1000 N, (b) 3000 N, (c) 6000 N and (d) 9000 N.

To investigate the interaction mechanisms in each of these frequency regions with different behavior patterns, the amplification and phase difference between the base structure and the resonators are investigated. As described by Brandão et al. (BRANDÃO; de Paula; FABRO, 2022), we can evaluate the interaction between resonators and base structure using the spatial average of the amplification, defined as

$$A_{\text{avg}} = \frac{1}{N_1} \sum_{n=1}^{N_1} A_i, \tag{5.5}$$

and phase difference, defined as

$$\phi_{\text{avg}} = \frac{1}{N_1} \sum_{n=1}^{N_1} \phi_i, \tag{5.6}$$

between the N_1 resonators and main structure.

To apply this concept to the system's response, $X^i_{\text{res}}/X^i_{\text{chain}} = A_i e^{j\phi_i}$, where X^i_{res} and X^i_{chain} are the complex amplitudes of each frequency component corresponding to the i^{th} resonator and the chain node to which it is attached. These spatial averages are shown for different excitation amplitudes in Figure 5.5 for 1 kN, Figure 5.6 for 6 kN and Figure 5.7 for 9 kN. The amplification patterns observed in Figures 5.5 to 5.7 show that when periodic motion is dominant, the attenuation mechanism is similar to those observed in linear systems, i.e., the phase difference between resonators and base structure are responsible for the vibration attenuation. This is very clear in Figure 5.5b with the phase difference jumping from 0 to 180 degrees at $\omega_0 = 250$ Hz. For the non-periodic response, however, something entirely different takes place, with seemingly randomized relative phase and broad spread of the frequency content.

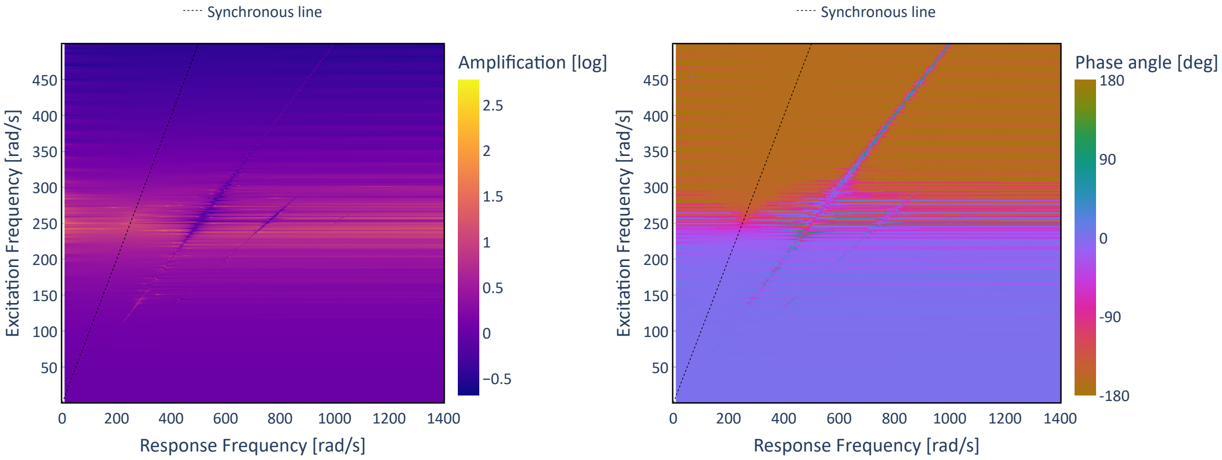

(a) (b)

Figure 5.5 – Spatially averaged amplification (a) and relative phase (b) between base chain and resonators for excitation amplitude of 1000 N.

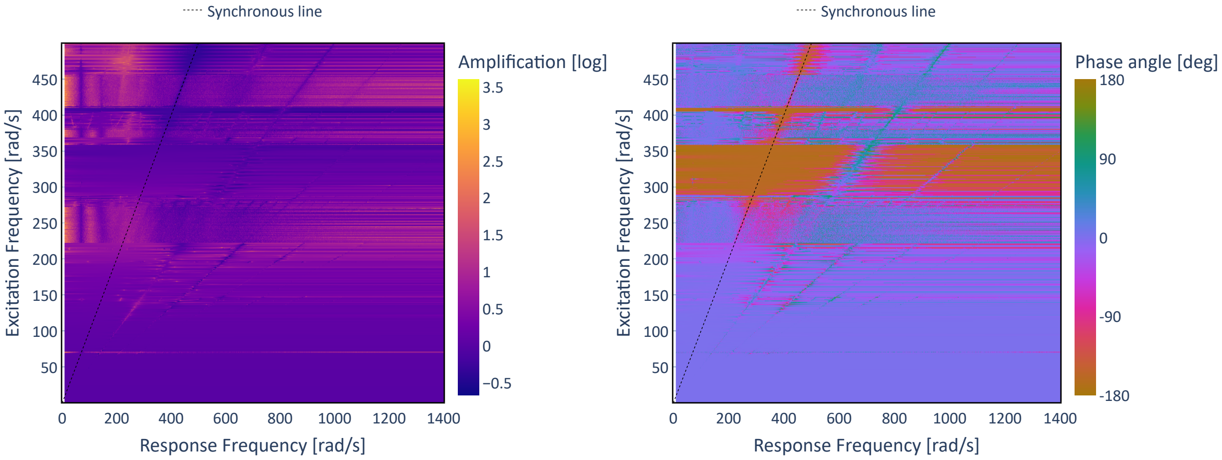

(a) (b)

Figure 5.6 – Spatially averaged amplification (a) and relative phase (b) between base chain and resonators for excitation amplitude of 6000 N.

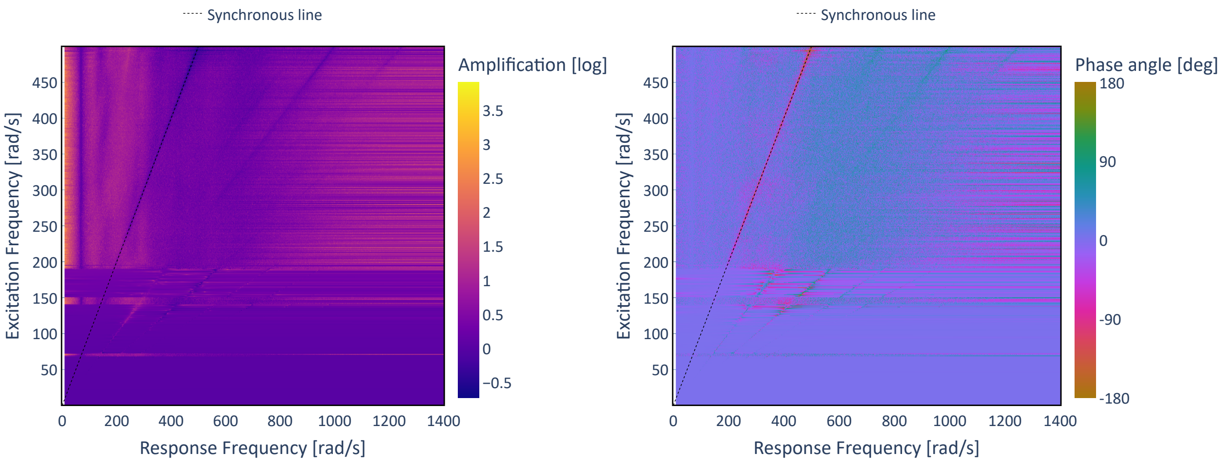

(a) (b)

Figure 5.7 – Spatially averaged amplification (a) and relative phase (b) between base chain and resonators for excitation amplitude of 9000 N.

For a better understanding of the energy distribution during these different dynamic patterns, it is useful to investigate the spatial distribution of vibrations throughout the system. Figure 5.8 shows the RMS vibration of each DOF in the system at both the chain and the resonators. It shows that when conditions indicate chaotic behavior, significantly higher vibration energy is directed to the resonators, as expected due to the energy dispersion (FANG et al., 2016; FANG et al., 2017).

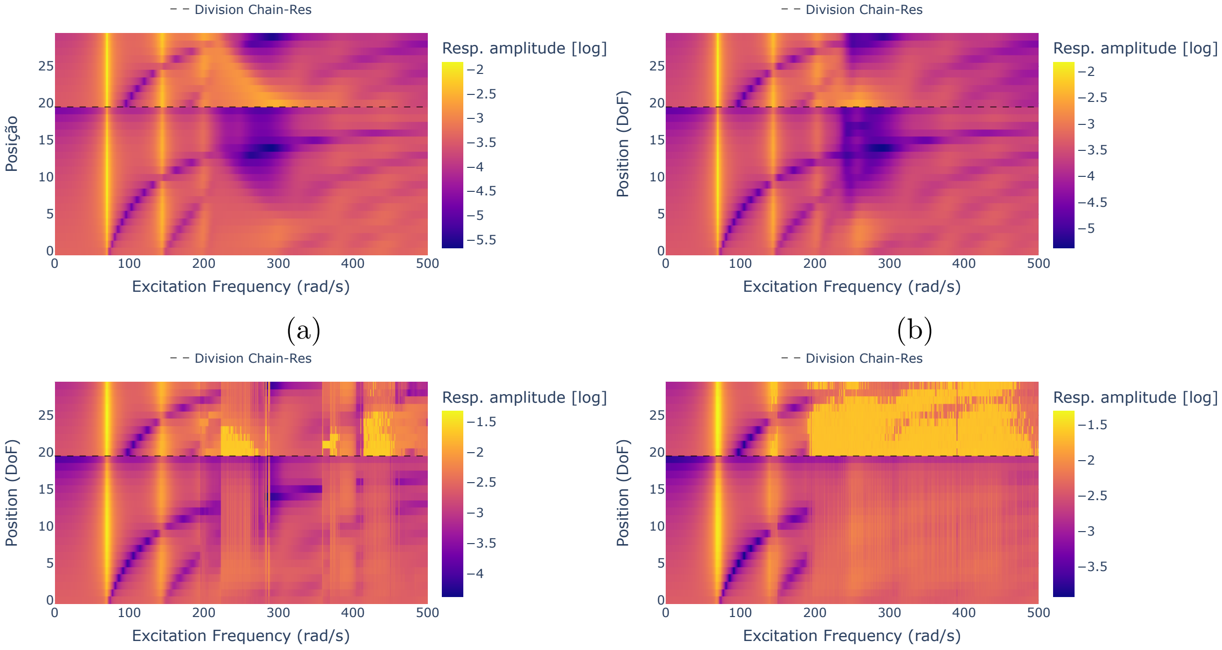

(a) (b) (c) (d)

Figure 5.8 – Spatial distribution of vibration for the linear system (a) and for the non linear system with different excitation amplitudes: (b) 1000 N, (c) 6000 N and (d) 9000 N.

Summarizing, these results show that the vibration attenuation mechanism in the presence of chaos is related to the amount of mechanical energy being directed towards the resonators in a much broader spectrum than the harmonic excitation frequency; i.e. it spreads the injected energy from one time scale towards several different time scales, thus reducing the maximum amplitudes of response. This is unlike the play of forces and relative phase angles that generate phase cancelation and, consequently, vibration attenuation in linear systems. In other words, conversion of a harmonic excitation to a broadband response has the effect of reducing the mechanical impedance of the resonators, thus increasing the effective impedance of the base structure.

Graded Resonators

In this section, the configuration with a graded array of resonators is investigated. The frequency response for different excitation amplitudes is shown in Figure 5.9. Similarly to the results presented in the previous section, these plots indicate the RMS displacement of the rightmost element, opposite to the point where the excitation is applied. In the linear case, the graded configuration of the resonators is responsible for a widening of the attenuation band compared to the periodic case, with a decrease in maximum attenuation performance (MENG et al., 2020d). The presence of amplitude peak in the bandgap can be caused by the localized vibration mode due to the presence of a local critical section (FABRO et al., 2021). Unlike the periodic case, the effect of the nonlinear resonator is negligible for the lowest 1000 N excitation amplitude. However, a similar broadband attenuation is achieved for increasing excitation amplitude, similar to the periodic case.

In general, the behavior of the system is quite similar to that of the periodic system, as shown in the corresponding bifurcation diagrams in Figure 5.10. However, the onset of chaotic behavior on frequencies other than the tuned frequency (250 Hz) seems to occur sooner on the graded resonator system. This difference is highlighted in Figure 5.11, which presents the frequency response heatmaps obtained from the classification configuration.

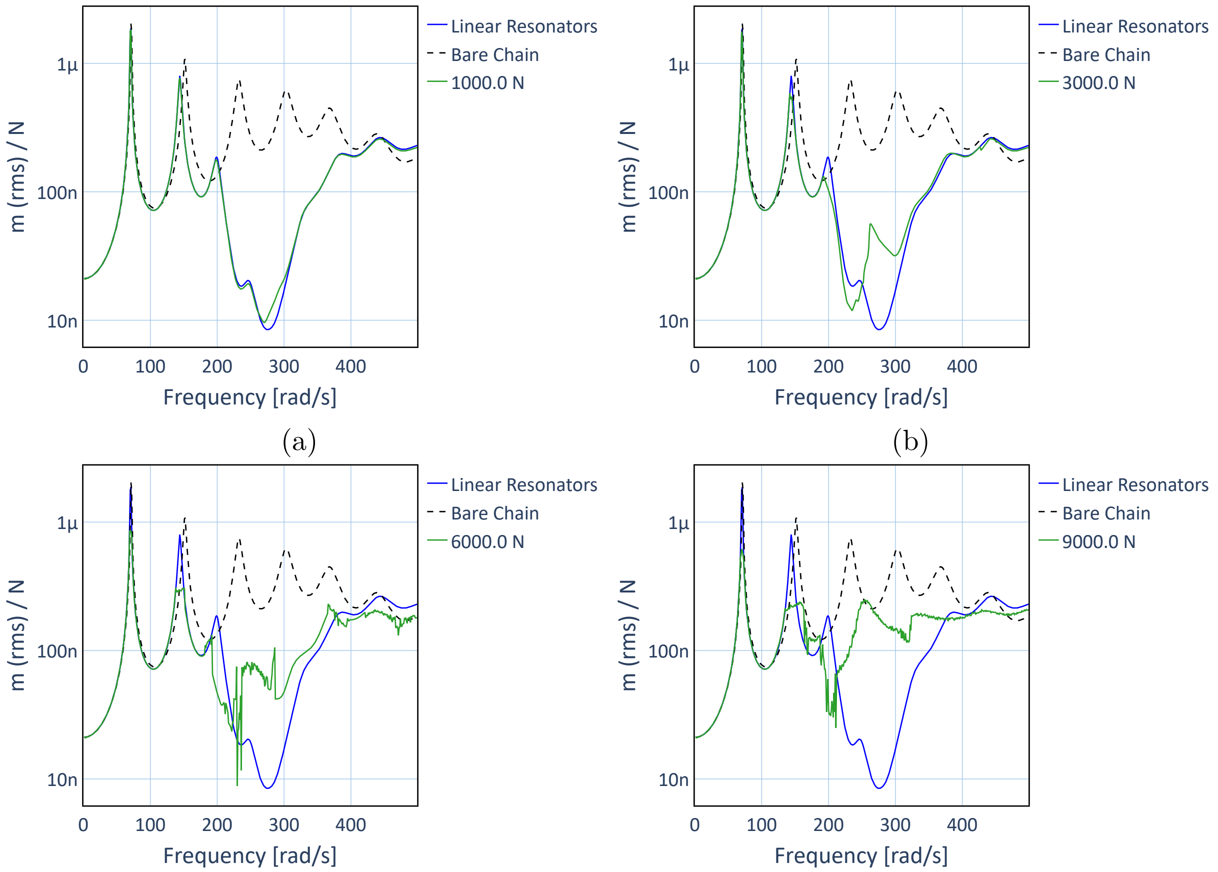

(a) (b)

(c) (d)

Figure 5.9 – Frequency Response plots comparing the system's response with graded resonators and with different excitation amplitudes: (a) 1000 N, (b) 3000 N, (c) 6000 N and (d) 9000 N.

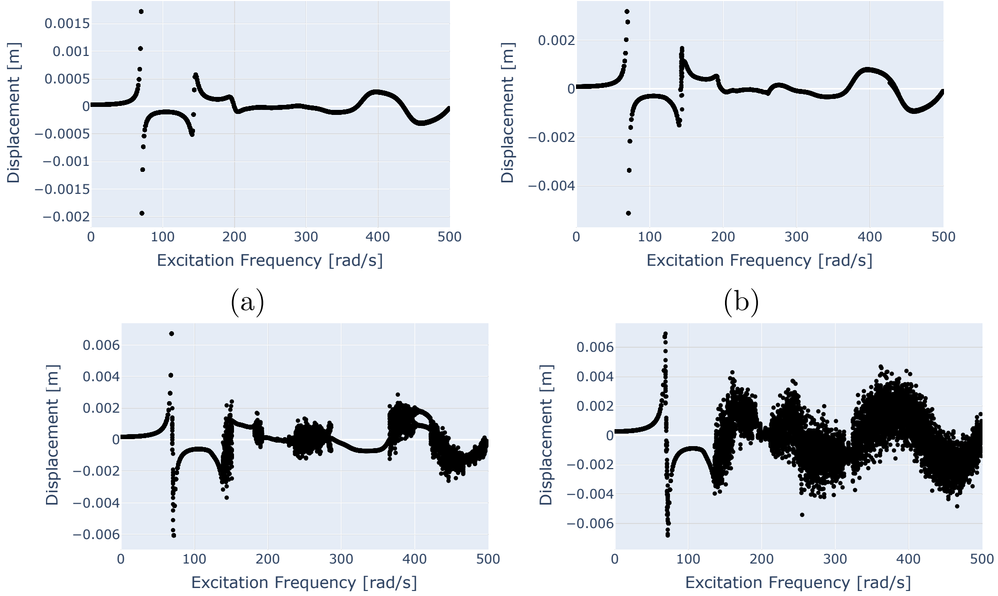

(a) (b)

(c) (d)

Figure 5.10 – Bifurcation Diagrams for different excitation amplitudes with graded resonators: (a) 1000 N, (b) 3000 N, (c) 6000 N, (d) 9000 N.

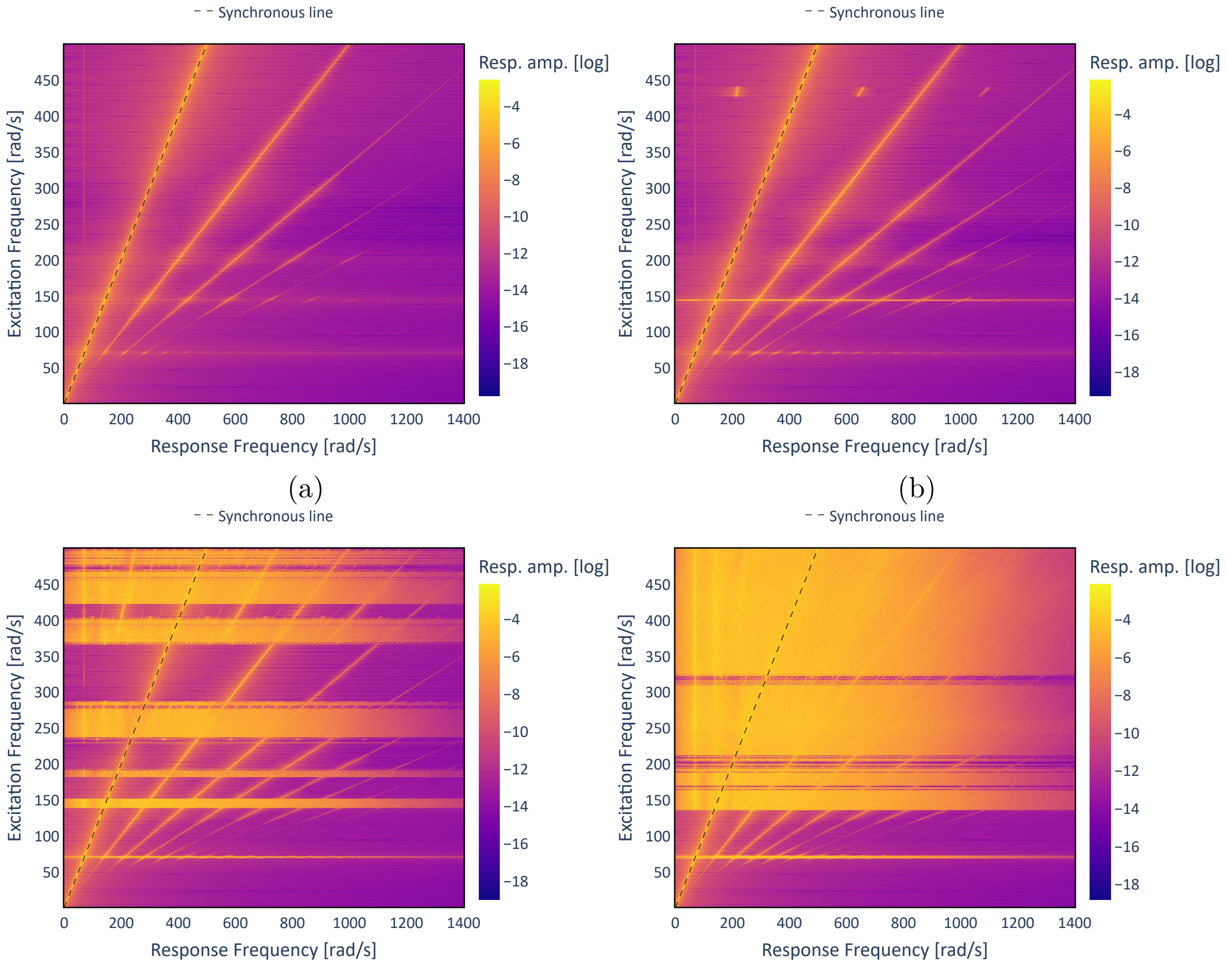

(a) (b)

(c) (d)

Figure 5.11 – Frequency Response heatmap of the system with graded resonators for different excitation amplitudes: (a) 1000 N, (b) 3000 N, (c) 6000 N and (d) 9000 N.

By comparing Figures 5.4c and 5.11c, it can be seen that the chaotic band around 250 Hz seems to be narrower, while at other frequency bands, such as 140 Hz, 190 Hz and above 350 Hz, it seems to have broader manifestation of chaos. This explains the more consistent flattening of the resonance peaks observed in Figure 5.9d. Consequently, the graded configuration has the effect of further widening the attenuation band.

Figures 5.12 to 5.14, present the spatially averaged amplification and relative phase between the base chain and the graded resonators for excitation amplitude of 1000 N, 3000 N and 6000 N, respectively. They provide similar conclusions as those reached for the periodic system, i.e., the phase is responsible for the attenuation mechanism for periodic motion while the randomized phase indicates a broadband energy distribution at the chaotic response.

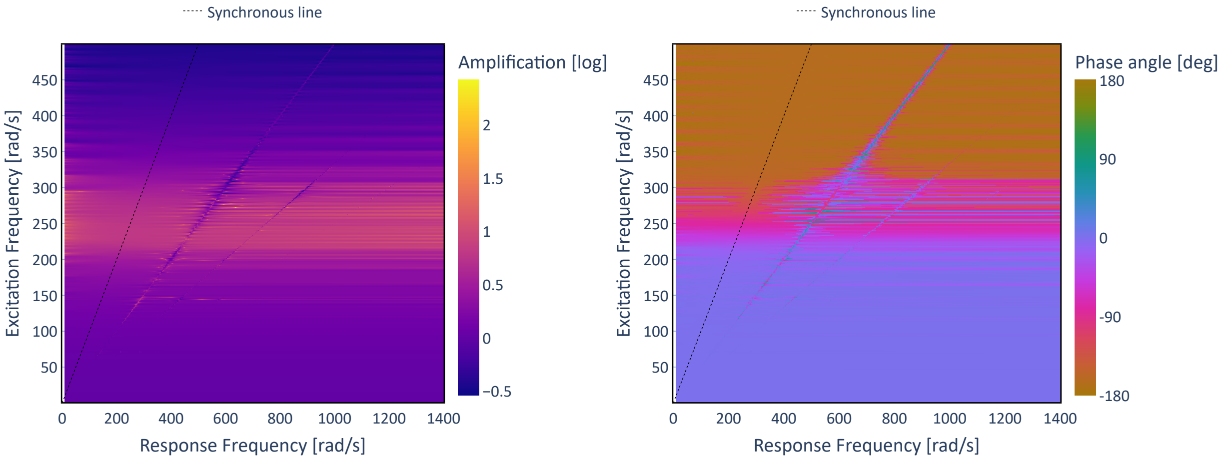

(a) (b)

Figure 5.12 – Spatially averaged amplification (a) and relative phase (b) between base chain and graded resonators for excitation amplitude of 1000 N.

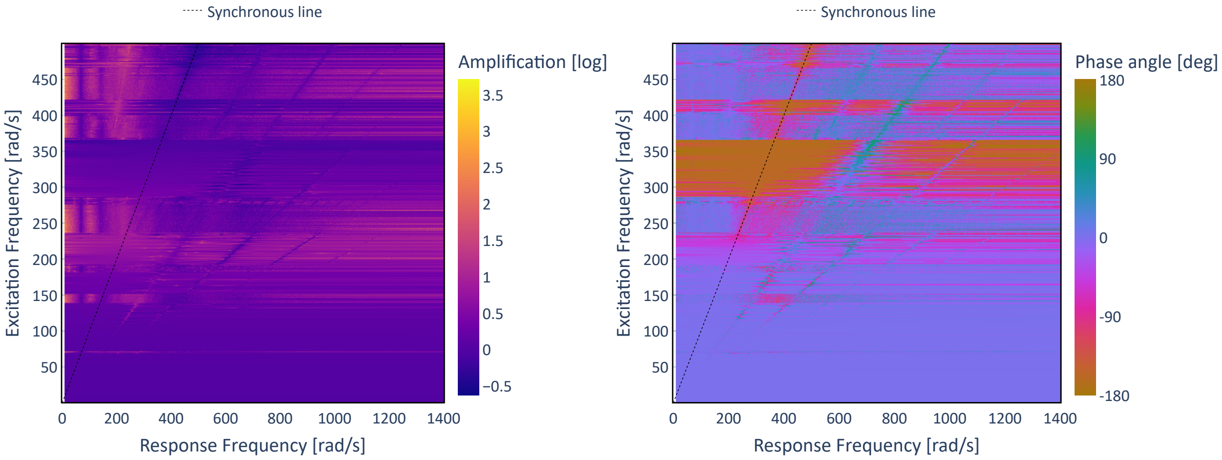

(a) (b)

Figure 5.13 – Spatially averaged amplification (a) and relative phase (b) between base chain and graded resonators for excitation amplitude of 6000 N.

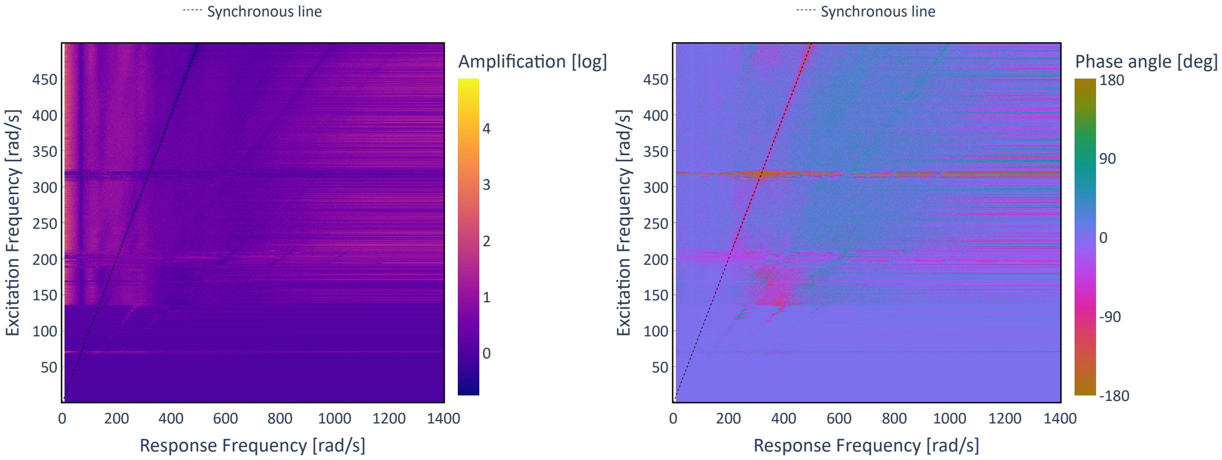

(a) (b)

Figure 5.14 – Spatially averaged amplification (a) and relative phase (b) between base chain and graded resonators for excitation amplitude of 9000 N.

The spatial distribution of the vibration amplitudes, shown in Figure 5.15, reveals the effects observed on the previous result from the activation of different sections of the resonator array in different frequencies. A similar conclusion is also presented in (BRANDÃO; de Paula; FABRO, 2022). In the nonlinear case, this effect is also extended to the mechanisms previously described in the previous section, which explains the chaotic bandgap widening due to the graded configuration.

The effective impedance of different sections of the array is significantly decreased in certain frequencies, thus reducing the overall energy circulating within the base structure.

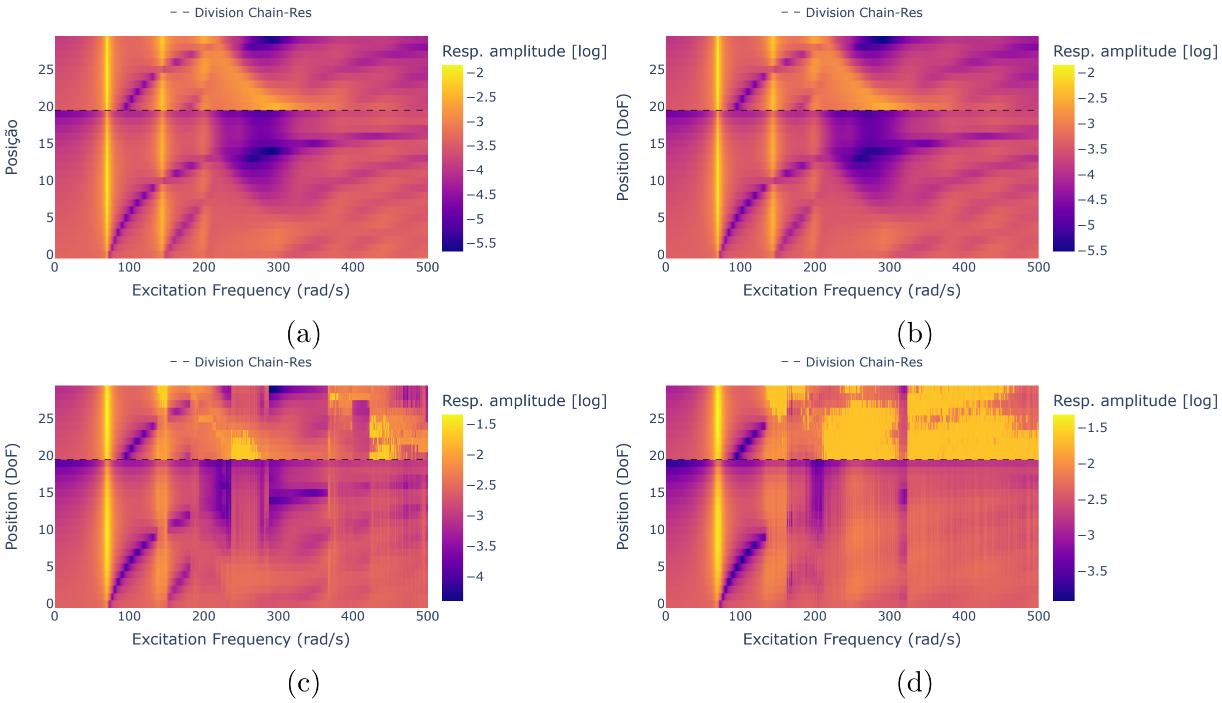

(a) (b) (c) (d)

Figure 5.15 – Spatial distribution of vibration with graded resonators for the linear system (a) and for the non linear system with different excitation amplitudes: (b) 1000 N, (c) 6000 N and (d) 9000 N.

5.3 Final Remarks

In this second phase of the thesis' investigation, we provided an introduction to the exploration of graded nonlinear metastructures. A simple 1-D periodic lattice system with bi-stable oscillators was used to allow a phenomenological exploration of its behavior. This approach established a baseline for the phenomena that can be expected to occur and also provided a set of tools to search for these same patterns in other systems.

The highlights and main findings are summarized below.

- Broadband vibration attenuation is obtained with the proposed arrangement and is associated with the system's chaotic response.
- The vibration attenuation behavior is strongly amplitude-dependent.

- The spatially averaged amplitude and phase angle maps revealed that the vibration attenuation mechanisms are fundamentally different than those in linear resonators.
- Upon the onset of chaotic behavior, the phase angle maps appear to assume a randomized distribution, with no clear, well-defined pattern as previously observed with linear resonators.
- The mechanical energy input is spread from a single harmonic to a broader spectrum, from one time scale towards several different time scales.
- The wider frequency range activation results in a decrease of the effective impedance of the oscillator array, while increasing that of the base structure.
- The graded arrangement of oscillators increases the overall vibration attenuation bandwidth by anticipating the onset of chaotic behavior.

We have now completed the exploration of two separate avenues of understanding for periodic metastructures in chapters 4 and 5. However, these two lines are yet to meet, and in this intersection, potentially synergetic effects may still be discovered.

6 Nonlinear Gyroscopic Metastructures

The discussions presented in this chapter aim towards the combination of concepts introduced in the previous sections in a final step to consolidate the complete picture of this thesis. A numerical setup of rotating mestastructures with nonlinear periodic resonators is developed to analyze the influence of chaotic behavior on these systems and its effects on the overall vibration attenuation performance. The rotating system presented in chapter 4 and evaluated in (BRANDÃO; de Paula; FABRO, 2022) is extended to incorporate the concept of bistable resonators described in chapter 5 as proposed by (BRANDÃO; de Paula; FABRO, 2024), which have shown significant vibration attenuation benefits. Part of the content of this chapter has been published in (BRANDÃO; de Paula; FABRO, 2025).

The main original contributions presented in this chapter are:

- The introduction of a novel *Modally Matched Distribution* (MMD) concept for oscillator positioning, with enhanced attenuation bandwidth;
- Investigation of dissimilar phase angle behavior of forward and backward whirl components;
- Detailed analysis of chaotic attenuation mechanisms in rotating systems under different excitation conditions (forward, backward, and unbalance);
- A tuning strategy to mitigate adverse effects of nonlinearity in the post-bandgap region.

6.1 System Description

In this section, the physical model used in the analyses is presented. The schematic physical configuration of the system is shown in Figure 6.1. It consists of a rotor (gray) supported by two isotropic bearings on its shaft ends modeled as spring-damper elements (green), three rigid axisymmetric disks (red) representing impellers or other mechanical components commonly attached to rotors, and evenly distributed local oscillators (blue).

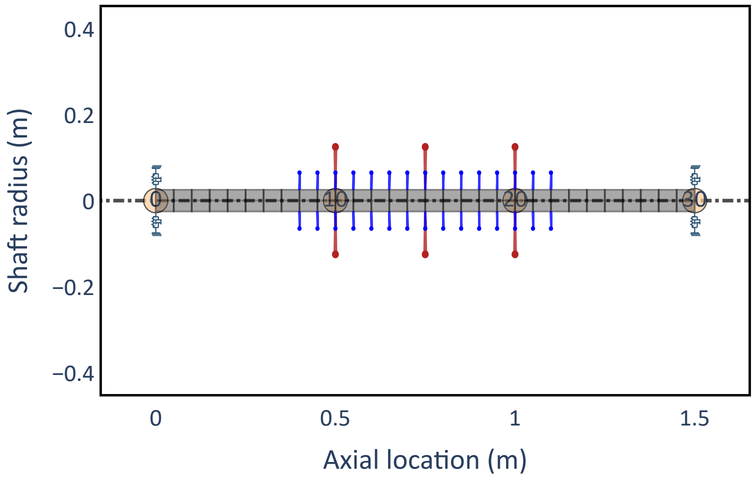

Figure 6.1 – Rotor FEM model of the shaft (grey), rigid axisymmetric disks (red), isotropic bearings (green) and oscillators (blue) and the bearings at the shaft ends.

The dynamic response of the rotor is evaluated through simulations using the finite element method (FEM), based on ROSS - Rotordynamic Open Source Software (TIMBÓ et al., 2020). The ROSS FEM model is built with 4 degrees of freedom, employing rotating Timoshenko beam elements. Adaptations are introduced in the software formulation to account for local oscillators as described in the sequence. The FEM model is built using 4 degrees of freedom Timoshenko beam elements. Every shaft element is identical, with aspect ratio $L/D = 1$ and diameter $D = 50$ mm. The total length of the rotor is 1.5 m.

Each disk oscillator is coupled to its corresponding main shaft node in the X and Y directions, as illustrated in Figure 6.2. The disks are modeled as rigid cylindrical elements with outer diameter $d_o = 140$ mm, inner diameter $d_i = 60$ mm, and length $L = 40$ mm. The mass of the resonators, m_r, and transverse and polar moments of inertia, $I_{t_{\text{osc}}}$ and $I_{p_{\text{osc}}}$, respectively, are obtained from the proposed geometry.

This approach is similar to that proposed by (BRANDÃO; de Paula; FABRO, 2022), with modifications to incorporate nonlinear spring elements. To allow a gradual understanding of the complex behaviors emerging from this system, a simplified configuration is considered, where nonlinear springs are present only in the X direction.

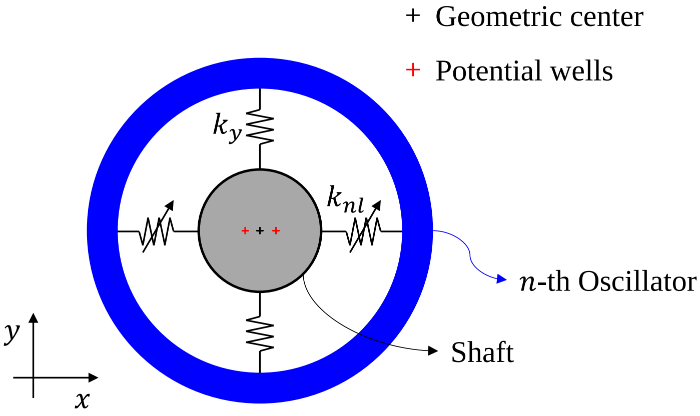

Figure 6.2 – Nonlinear oscillator and rotor attachment on X-Y plane projection.

The equations of motion are given by:

$$[\mathbf{M}]\ddot{\mathbf{x}} + ([\mathbf{C}] + \Omega[\mathbf{G}])\,\dot{\mathbf{x}} + \left([\mathbf{K}_s] + \sum_{n=1}^{N_o}[\mathbf{K}_o]^n\right)\mathbf{x} + \sum_{n=1}^{N_o}\mathbf{f}_{nl}^n(\mathbf{x},\dot{\mathbf{x}}) = 0, \tag{6.1}$$

where $[\mathbf{M}]$ and $[\mathbf{C}]$ are the mass and damping matrices, respectively. The matrix $[\mathbf{K}_s]$ represents the bare shaft stiffness matrix and $[\mathbf{K}_o]^n$ represents the linear stiffness components - k_y - of the n-th oscillator. The matrix $[\mathbf{G}]$ is the gyroscopic matrix that appears multiplied by the shaft rotation speed Ω. The vector $\mathbf{f}_{nl}^n$ represents the effects of the nonlinear springs - k_{nl} - of the n-th oscillator, being a function of $\mathbf{x}$ and $\dot{\mathbf{x}}$. In all further matrices and vectors presented henceforth, the superscript n corresponds to the n-th oscillator.

The vector $\mathbf{x}$ represents the system's displacements and is defined as $\mathbf{x} = \{\mathbf{x}_1\, \mathbf{x}_2\, \ldots\, \mathbf{x}_{N+N_o}\}^T$, where N is the total number of shaft nodes, N_o is the number of oscillators, and each component of $\mathbf{x}$ is the displacement vector of each shaft node or oscillator, described by $\mathbf{x}_k = \{x_k\; y_k\; \theta_k^x\; \theta_k^y\}$.

Figure 6.3 presents the composition of a matrix $[\mathbf{K}]$, which contains the linear stiffness coefficients of the model. In the representation, $\mathbf{O}_{M_1\times M_2}$ is a $M_1 \times M_2$ zero matrix and $[\mathbf{K}_{\text{shaft}}]$ is the bare rotor stiffness matrix. $[\mathbf{K}_o]^n$ and $[\mathbf{K}_s]$are sparse $(N+N_o)\times(N+N_o)$ matrices.

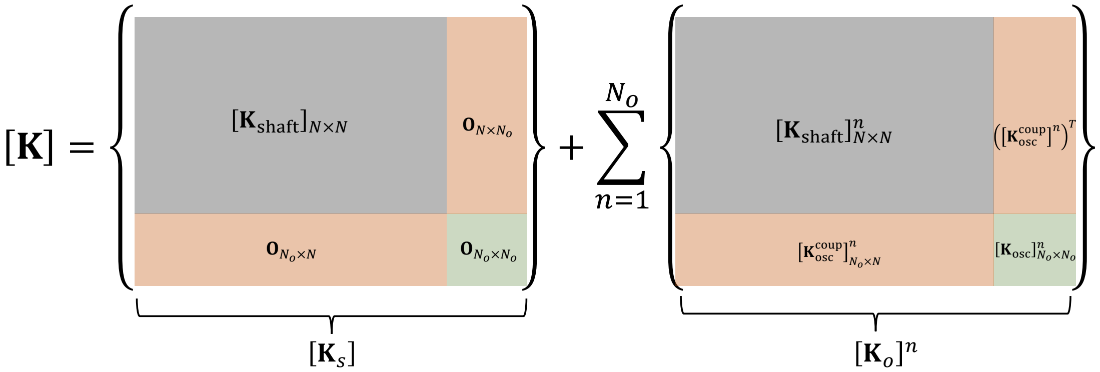

Figure 6.3 – Matrix composition of the linear stiffness components.

The matrix $[\mathbf{K}_o]^n$ defines the connection between the oscillators and the main shaft due to the linear stiffness component. For each oscillator, the connection between shaft node i and respective oscillator node j can be described in terms of the translational and rotational connectivity matrices as follows:

$$[\mathbf{K}_o]^n = k_y[\mathbf{S}_y]^n + k_\theta[\mathbf{S}_\theta]^n, \tag{6.2}$$

where k_y is the linear coupling stiffness in the Y direction and k_θ is the linear isotropic rotational coupling stiffness.

The sparse connectivity matrices $[\mathbf{S}_x]^n$, $[\mathbf{S}_y]^n$ and $[\mathbf{S}_\theta]^n$ can be defined based on the 8×8 compact forms shown in Eqs. 6.3 and 6.4, as explained in the continuation of this section.

$$[S_x] = \begin{bmatrix} 1 & 0 & 0 & 0 & -1 & 0 & 0 & 0 \\ 0 & 0 & 0 & 0 & 0 & 0 & 0 & 0 \\ 0 & 0 & 0 & 0 & 0 & 0 & 0 & 0 \\ 0 & 0 & 0 & 0 & 0 & 0 & 0 & 0 \\ -1 & 0 & 0 & 0 & 1 & 0 & 0 & 0 \\ 0 & 0 & 0 & 0 & 0 & 0 & 0 & 0 \\ 0 & 0 & 0 & 0 & 0 & 0 & 0 & 0 \\ 0 & 0 & 0 & 0 & 0 & 0 & 0 & 0 \end{bmatrix}, [S_y] = \begin{bmatrix} 0 & 0 & 0 & 0 & 0 & 0 & 0 & 0 \\ 0 & 1 & 0 & 0 & 0 & -1 & 0 & 0 \\ 0 & 0 & 0 & 0 & 0 & 0 & 0 & 0 \\ 0 & 0 & 0 & 0 & 0 & 0 & 0 & 0 \\ 0 & 0 & 0 & 0 & 0 & 0 & 0 & 0 \\ 0 & -1 & 0 & 0 & 0 & 1 & 0 & 0 \\ 0 & 0 & 0 & 0 & 0 & 0 & 0 & 0 \\ 0 & 0 & 0 & 0 & 0 & 0 & 0 & 0 \end{bmatrix} \quad \text{and} \tag{6.3}$$

$$[S_\theta] = \begin{bmatrix} 0 & 0 & 0 & 0 & 0 & 0 & 0 & 0 \\ 0 & 0 & 0 & 0 & 0 & 0 & 0 & 0 \\ 0 & 0 & 1 & 0 & 0 & 0 & -1 & 0 \\ 0 & 0 & 0 & 1 & 0 & 0 & 0 & -1 \\ 0 & 0 & 0 & 0 & 0 & 0 & 0 & 0 \\ 0 & 0 & 0 & 0 & 0 & 0 & 0 & 0 \\ 0 & 0 & -1 & 0 & 0 & 0 & 1 & 0 \\ 0 & 0 & 0 & -1 & 0 & 0 & 0 & 1 \end{bmatrix}. \tag{6.4}$$

To define the spatial distribution of the oscillators along the shaft, it is necessary to convert the compact form of $[S_m]$ to its sparse representation $[\mathbf{S}_m]^n$, where $m = x, y, \theta$. This process relies on a mapping vector $\mathbf{x}^{ij} = \{\mathbf{x}_i, \mathbf{x}_j\}^T$, which corresponds to the translational and rotational degrees of freedom (DoFs) of the nodes i and j, respectively. Here, i is the shaft node to which the oscillator is attached, varying from 1 to N, and $j = N + n$, where n corresponds to the n-th oscillator.

The nonlinear component $\mathbf{f}_{nl}$, associated with the nonlinear springs k_{nl} shown in Figure 6.2, is modeled as a Duffing oscillator-type nonlinearity and can also be expressed in terms of the connectivity matrix $[S_x]$ as

$$\mathbf{f}_{nl}(\mathbf{x}, \dot{\mathbf{x}}) = \sum_{n=1}^{N_r} \delta[\mathbf{S}_x]_n \dot{\mathbf{x}} + \beta[\mathbf{S}_x]_n \mathbf{x} + \alpha([\mathbf{S}_x]_n \mathbf{x})^3, \tag{6.5}$$

where δ and β are linear dissipative and restorative components, respectively, and α is the nonlinear coefficient of the cubic component of the Duffing oscillator.

The system investigated, as the one investigated in (BRANDÃO; de Paula; FABRO, 2022) (Chapter 4), represents oscillators rotating around their own symmetry axis, regardless of their relative position to the shaft element to which it is attached. This is a strong and fundamental consideration for the model, especially when considering an arrangement in which the coupling can be bi-stable, allowing an oscillator to have a stable state in which it is eccentric to the main shaft. This assumption enables the system's mathematical modeling to be developed in a fixed, non-rotating reference frame. Thus, the linear and nonlinear connecting stiffnesses, k_y and k_{nl}, act within this fixed reference frame. This consideration leads to a simpler mathematical model but makes the experimental setup more challenging to develop. A hypothetical experimental setup to reproduce this mathematical concept would have, for example, a non-rotating pair of magnets on each side of the oscillator that would provide the cubic component of $\mathbf{f}_{\mathrm{nl}}$.

6.1.1 System parameters

Numerical simulations were performed with the same geometric parameters of the system presented by Brandão, de Paula & Fabro (2022).

The stiffness coefficients k_y and k_θ are calculated in terms of the desired tuning frequency ω_0 as follows:

$$k_y = m_o \omega_0^2 \quad , \quad k_\theta = 100 I_{t_{\text{osc}}} \omega_0^2, \tag{6.6}$$

where m_o and $I_{t_{\text{osc}}}$ are the mass and transverse moment of inertia of the oscillators, respectively. The value of k_y results in oscillators with translational natural frequencies equal to ω_0. The rotational k_θ, on the other hand, is defined as being 100 times higher than the value needed to tune the respective natural frequency to the target natural frequency ω_0. This effectively creates a rigid coupling of the rotational degrees of freedom, which will not display significant relative displacement within the frequency range of interest.

To define the parameter of the Duffing oscillator, δ, β, and α, the parametrization strategy applied by (BRANDÃO; de Paula; FABRO, 2024) was used. The restorative component of Equation 6.5 is given by $F_{\mathrm{r}}(x) = -\beta x - \alpha x^3$. This study explores the case in which $\beta < 0$, corresponding to a bi-stable oscillator. The nonzero roots of the restoring force expression provide the system's equilibrium positions $x_0 = \pm\sqrt{\frac{-\beta}{\alpha}}$, which correspond to the eccentricity of the potential wells.

The derivative of $F_{\mathrm{r}}(x)$ provides the system's locally linearized stiffness $\frac{dF_{\mathrm{r}}}{dx} = k_{\text{lin}}(x)$. From this expression, it is possible to obtain

$$k_{\text{lin}}(x_0) = -\left.\frac{dF_{\mathrm{r}}}{dx}\right|_{x_0=\sqrt{\frac{-\beta}{\alpha}}} = -2\beta, \tag{6.7}$$

which corresponds to the linearized stiffness for small oscillations around the equilibrium position x_0

It is possible to determine the natural frequency ω_0 of the locally linearized oscillator as $\omega_0 = \sqrt{\frac{k_{\text{lin}}(x_0)}{m_0}}$, where m_0 is the oscillator reference mass value. The Duffing oscillator parameters α and β can then be defined in terms of the physical quantities ω_0 and m_0 as $\beta = -\frac{\omega_0^2 m_0}{2}$ and $\alpha = -\frac{\beta}{x_0^2}$. The dissipative term of Equation 6.5 $\delta = c_p k_{\text{lin}} = c_p \omega_0^2 m_0$.

In some cases a graded mass distribution case was also investigated. In this configuration, a linearly increasing gradation is applied according to the function $f_m(m_0)$, defined as

$$m_n = f_m(m_0) = m_0 \left(0.6 \frac{n-1}{N_1 - 1} + 0.7\right) \quad ; \quad n = 1 \ldots N_1. \tag{6.8}$$

This gradation is applied to all oscillators, which are numbered sequentially from 1 to N_1 from left to right. This increasing mass gradation leads to a distribution of oscillators with linearized natural frequencies ranging from $\sqrt{0.7}\omega_0$ to $\sqrt{1.3}\omega_0$. This results in a frequency range of approximately 15% around the centered frequency, within which the oscillators are expected to effectively influence the dynamics of the base system.

A proportional damping $[\mathbf{C}_o]^n = c_p[\mathbf{K}_o]^n$ is also considered.

6.2 Results and discussion

The following subsections present the main results for the system described in section 6.1. The first configuration evaluates the performance of the metastructure with oscillators distributed at the center of the shaft, while the second explores the proposed alternative distribution strategy - Modally Matched Distribution - which enhances vibration attenuation. In both cases, performance is evaluated under forward, backward and unbalanced excitation conditions.

6.2.1 Standard Oscillator Distribution

The results in this chapter present the behavior of the system under different load conditions and system arrangements. In all cases in this section 6.2.1, the oscillator's tuning frequency was set at $\omega_0 = 400$ rad/s, which lies between the third pair of backward and forward natural frequencies. The mode shape of the target critical speed is presented in Figure 6.4. First, speed-independent forward and backward excitation conditions are evaluated. For these cases, $x_0 = 2$ mm was used.

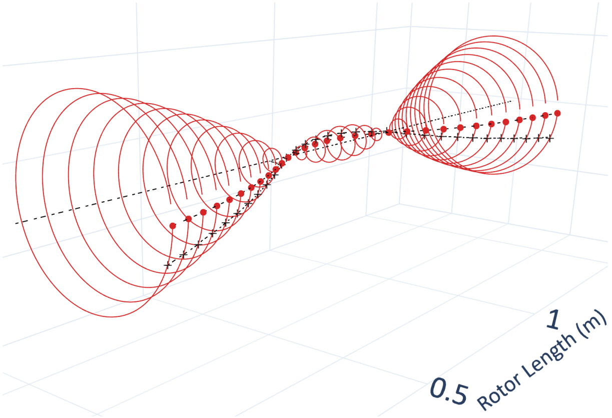

Figure 6.4 – Mode shape at the targeted natural frequency for attenuation.

Figure 6.5 shows the frequency response function of the system under forward and backward excitations for three cases: the rotor with rigid disks instead of oscillators, the rotor with linear resonators, and the rotor with nonlinear oscillators. In the latter case, various excitation amplitudes are considered. The responses shown represent the amplitude in the X direction at the rotor's rightmost node, while the excitation is applied to the rotor's leftmost node as either a purely forward or a purely backward load.

The forward excitation results presented in Figure 6.5 show an enhanced vibration attenuation by the nonlinear metamaterials for frequencies below ω_0. This effect is more pronounced as the excitation amplitude increases. However, for frequencies above ω_0, a

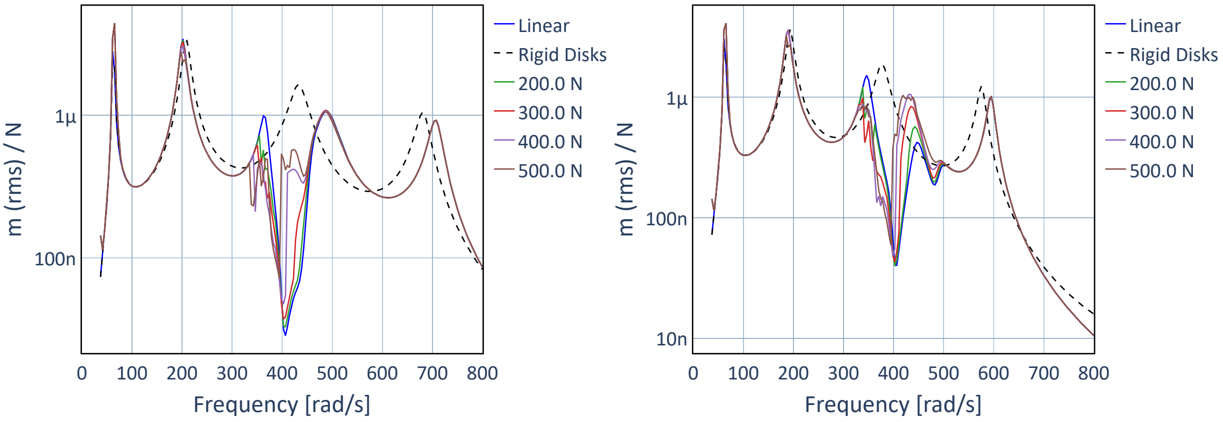

(a) (b)

Figure 6.5 – Frequency Response Functions for (a) forward and (b) backward excitations with identical oscillators.

degradation in attenuation performance is observed within the linear bandgap range. The backward excitation exhibits a similar behavior below the tuning frequency ω_0, with a significant attenuation of the acoustic-mode peak (i.e., below the bandgap), which is clearly present for the linear configuration. However, above the linear bandgap range, the system tends to exhibit higher amplitudes compared to the linear case as the excitation amplitude increases, resulting in a noticeable loss of attenuation performance. Fang et al. (2016) has briefly discussed this asymmetry effect by analyzing the optical and acoustic branches on the dispersion diagram of a nonlinear acoustic metamaterial.

In a complementary interpretation, the loss of attenuation performance due to the bistable metastructure arrangement at frequencies above ω_0 may be attributed to the phase relation between the main shaft and oscillators in optical modes, i.e., above the bandgap (BRANDÃO; de Paula; FABRO, 2024). Optical modes usually present a phase angle close to 180° between the oscillators and the main structure. This may generate higher relative displacements between these elements, leading to increased activation of the stiffening effect from the nonlinear stiffness that connects them. Qualitatively, this has the effect of *mistuning* the oscillators and changing their behavior compared to the linear case. To mitigate this possible mistuning effect, a graded array of oscillators is applied, following the rule defined in Equation 6.8.

Figure 6.6 shows the frequency response function of the system under the same excitation conditions previously applied. Some improvement in the attenuation performance can be noticed if compared with the behavior of bistable identical oscillators, significantly increasing the bandwidth of vibration attenuation. However, the benefits are still largely limited to the frequency range below the bandgap. In this range, we observe the near-complete elimination of the left sideband peak around 330 rad/s. For the forward excitation cases of 400 N and 500 N, a significant attenuation of the second natural frequency is also observed at 200 rad / s.

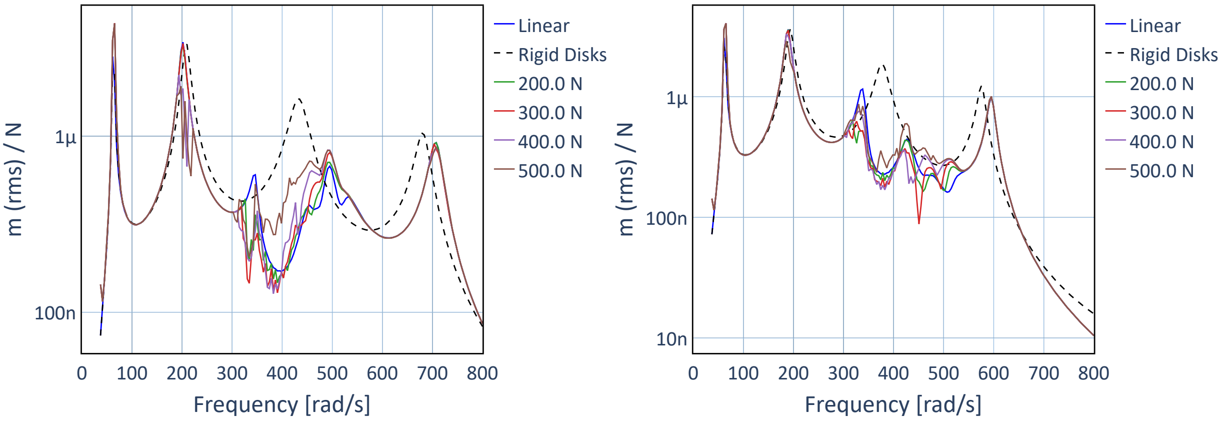

(a) (b)

Figure 6.6 – Frequency Response Functions for (a) forward and (b) backward excitations with graded oscillators.

To evaluate more realistic excitation sources, one should analyze the response of the system to imbalance. Unbalance forces are a very particular type of excitation, with three main characteristics: they are synchronous, purely forward, and their amplitude is proportional to Ω^2, with Ω being the rotor rotation speed. Unbalance excitations are by far the most common source of excitation in rotating systems. In turbomachinery applications, various industry standards define typical allowable magnitudes for these forces. API TR 684 (API TR 684-1, 2019) suggests for unbalance response analyses the use of a baseline unbalance magnitude as follows:

$$U = 6350\frac{W}{\Omega} \tag{6.9}$$

where U is the unbalance magnitude in g-mm, W is the total rotor weight in kg and Ω is the maximum rotation speed of the shaft in rpm. This formula represents a G0.67 balancing grade according to ISO 1940-1 (ISO 1940-1, 2003). This is the typical balancing grade level required for critical machinery in the Oil & Gas Industry, as defined by API Std 617 (API Std 617, 2022) for centrifugal compressors and by API Std 610 (API Std 610, 2021) for large centrifugal pumps. For the rotor used in this analysis, with a total mass of $W = 179.6$ kg and considering $\Omega = \omega_0 = 400$ rad/s, we obtain $U = 316.7$ g-mm.

The aforementioned standards define the use of multiples of U, as defined in Eq. 6.9, to assess the machine's rotordynamic design and its sensitivity to unbalance, guiding the way industrial machines are actually designed and fabricated. Thus, evaluating multiple values of U provides a realistic quantitative estimate of the system's response in real-world conditions.

The unbalance excitation forces are applied to the leftmost node of the rotor, as in the previous analyses, following forward whirl direction. The excitation amplitude is nU, where n is an integer that is varied to observe the effects of increasing load on the system.

This approach also provides a better understanding of the system's design parameters and its scalability to real applications. As discussed, x_0 is one of these parameters that is key to the system's behavior and attenuation performance, and can only be set to a reasonable value once we define the excitation magnitudes for which the rotor is designed. In the cases presented here, the value of $x_0 = 0.5$ mm proved to be adequate for the design excitations of $4U$, and this value is used in all unbalance response results.

Figure 6.7 shows the frequency response functions for the same three conditions previously investigated. The cases of unbalance response show a consistent improvement in attenuating the peak around 330 rad/s when comparing nonlinear with linear resonators. However, within and beyond the linear bandgap frequency range, there is no clear improvement in attenuation.

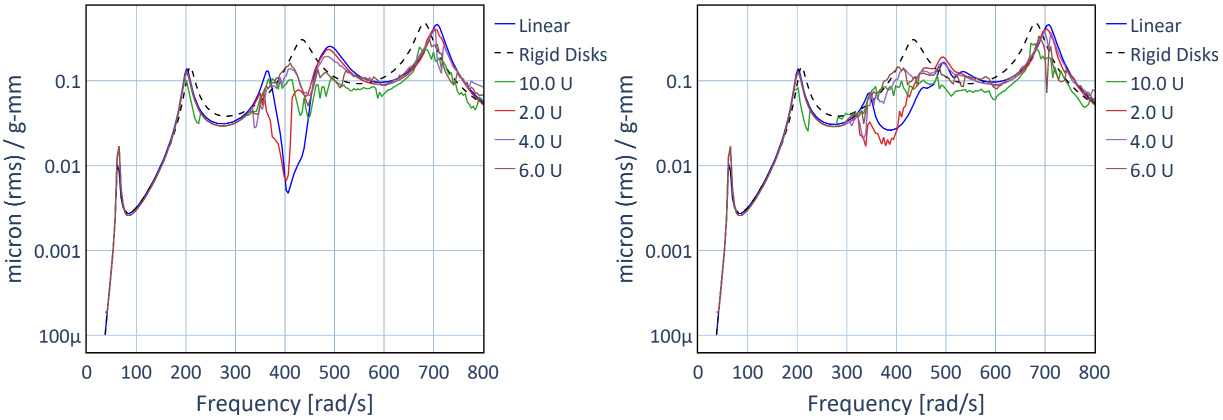

(a)

(b)

Figure 6.7 – Frequency Response Functions for unbalance excitation. (a) Identical oscillators and (b) graded oscillators.

To provide insight into the distinct patterns of dynamic activation of oscillators under different frequency conditions, Figure 6.8 presents phase space trajectories and Poincaré maps for $\Omega = 360$ rad/s and $\Omega = 700$ rad/s.

Figures 6.8a and 6.8b show orbit plots at a frequency below ω_0, for nonlinear and linear oscillators. The chaotic whirl of oscillator 1 exhibits complex dynamics reaching displacements of similar magnitude in both the horizontal and vertical coordinates. This indicates that, although the nonlinear element is oriented along the horizontal direction, both directions, spatially coupled by the gyroscopic force components, are activated in such a way that significant displacements also occur in the vertical direction. As a consequence, lower vibration levels are observed at the end of the shaft compared to its linear counterpart. This indicates that, by activating the dynamics at different spatiotemporal scales, the chaotic behavior creates different pathways for energy transfer between the base structure and oscillators, increasing their potential to function as energy sinks. The different time scales arise from the chaotic response itself, which spreads the system dynamics over a broad range of frequencies. Meanwhile, the different spatial scales result from the gyroscopic nature of the system's dynamics, which induces large-amplitude motions of the oscillators

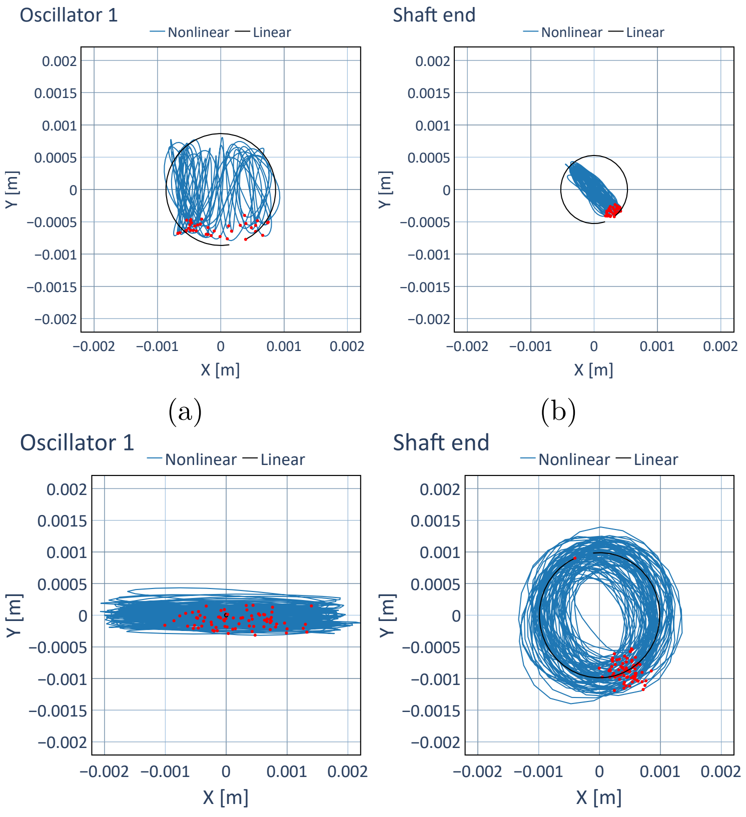

(a) (b)

(c) (d)

Figure 6.8 – Orbit plots of oscillator 1 (left) and shaft end (right) for linear and nonlinear oscillators. All cases correspond to identical resonators under a $10U$ unbalance excitation. Excitation frequencies are 360 rad/s for (a) and (b) and 700 rad/s for (c) and (d).

not only in the direction associated with the nonlinear element but also in the vertical direction.

This interpretation is supported by the orbit plots in Figures 6.8c and 6.8d, which correspond to an excitation frequency higher than ω_0. Although the oscillator's orbit still appears chaotic, it exhibits a predominantly horizontal whirl, with a noticeably weaker dynamic activation in the vertical direction. The vibration of the shaft end in this case shows a higher amplitude than its linear counterpart. One can also note that the linear oscillator trajectory in Figure 6.8c shows very small amplitudes.

An exception to the observations mentioned above can be identified in a narrow frequency range around 500 rad/s in Figure 6.7a. In this range, the $6U$ unbalance case showed significant vibration attenuation of the optical mode peak.

Figure 6.9 shows the orbit plots of the first and second oscillators and their corresponding shaft nodes under conditions where improved vibration attenuation is achieved near 500 rad/s and $6U$ unbalance. These reveal a unique response pattern of the first oscillator, with high amplitude, high energy, and an interwell trajectory, while the second oscillator remains in an intrawell, lower amplitude path. In both cases, it is evident that, although the system excitation source is an imbalance, which is a purely forward and isotropic dynamic load, the system responds with strong asymmetry. Even though the rotor model is perfectly symmetric and isotropic, which would result in an isotropic response with decoupled forward and backward components, the nonlinear asymmetry introduced by the oscillators influences the system response in this very particular way.

Although both patterns show seemingly chaotic motion, the first oscillator behavior appears to be fundamentally different and may contribute to the observed improvement in attenuation performance. This behavior is further investigated in the following section of the paper, as it is promising for improved attenuation performance.

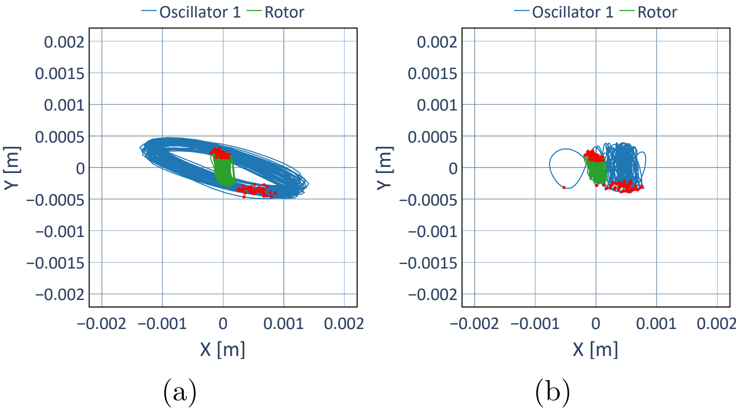

(a) (b)

Figure 6.9 – Orbit plots of the oscillator and corresponding shaft node under $6U$ unbalance excitation condition, with identical oscillators and $\Omega = 503$ rad/s. (a) First leftmost oscillator. (b) Second leftmost oscillator.

Figure 6.10 presents a color scale map representing the spatial average of amplification and phase angle, as proposed for the analysis of periodic linear resonators in rotors (BRANDÃO; de Paula; FABRO, 2022) and periodic lattices with graded bistable resonators (BRANDÃO; de Paula; FABRO, 2024).

Negative frequencies show the backward components, while positive frequencies show the forward ones. The results highlight that phase angle disorder is maintained in a wider frequency band in the case of unbalanced excitation, even for frequencies above the tuning frequency ω_0. This indicates that the system's chaotic response is most likely preserved as well. However, the region close to the synchronous frequency shows significantly lower amplification and a more stable phase angle for $\Omega > \omega_0$, which may explain the reduced attenuation performance.

The analysis of these results can be complemented with the evaluation of full spectrum waterfall plots of the rightmost rotor element, shown in Figure 6.11. It can be seen that the activation of seemingly chaotic response is very limited for the forward excitation case, being restricted to frequencies close to ω_0. On the other hand, the unbalance response condition presents a much more stable and consistent presence of chaos, with broadband response patterns across a wide range of excitation frequencies.

It is also possible to see a particular response pattern in Figure 6.11d around the excitation frequency of 500 rad/s, where a pronounced harmonic component of 3 times

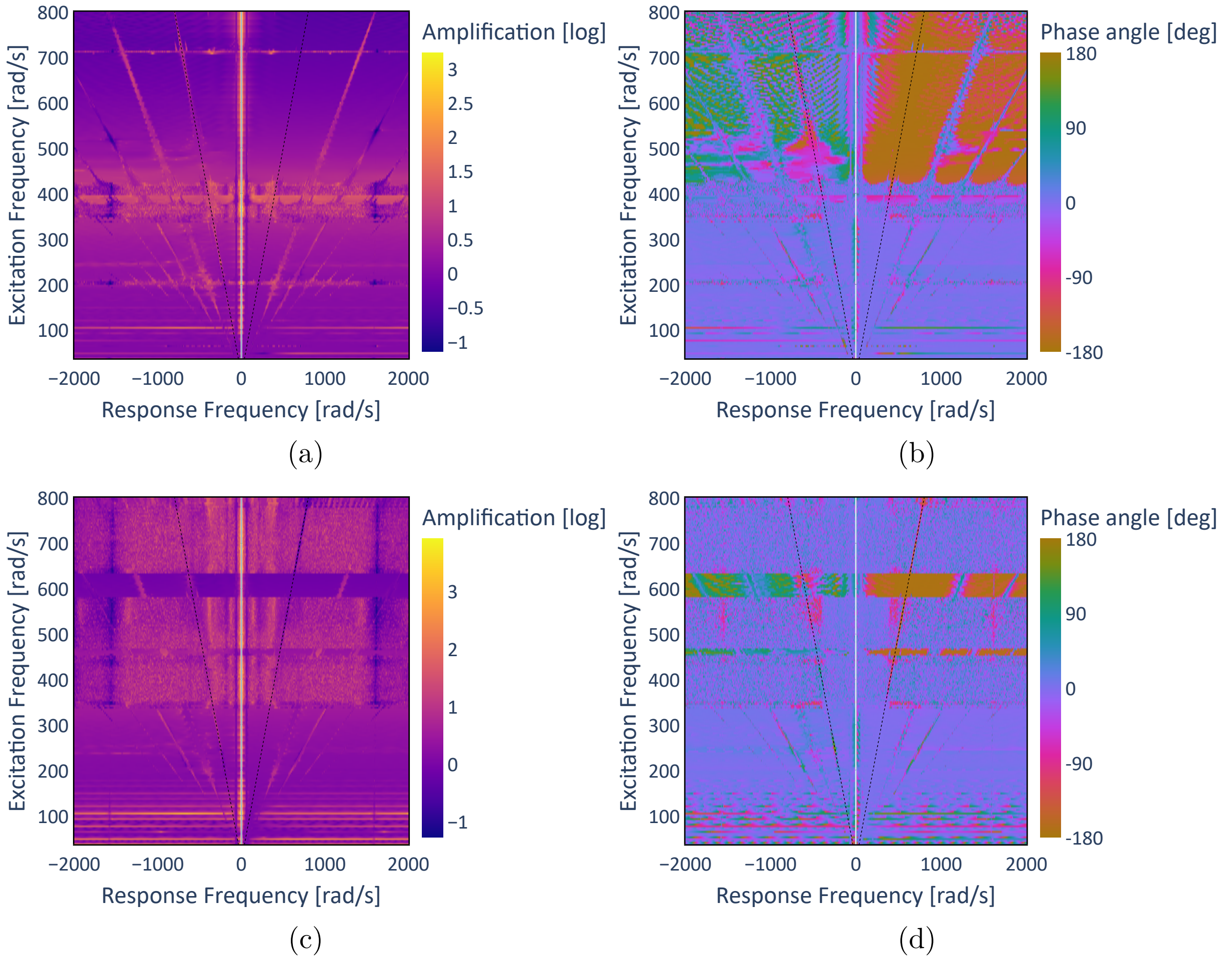

Figure 6.10 – Averaged amplification and phase angle plots for high excitation amplitude. (a) Averaged amplification heatmap and (b) phase angle map for forward excitation of 500 N. (c) Averaged amplification heatmap and (d) phase angle map for unbalance excitation of $4U$.

the synchronous frequency emerges within the chaotic broadband spectrum. The response presented in Figure 6.8 falls within this region.

Another important observation is that the synchronous backward component amplitudes are present in the response mainly during seemingly chaotic behavior. However, some non-synchronous backward components, especially 2X and 3X, have significant amplitudes mostly with excitation frequencies lower than 300 rad/s, where periodic multi-harmonic response patterns are visible.

6.2.2 Modally Matched Distribution of the Oscillators

Motivated by some of the results presented in Section 6.2.1, an alternative method is proposed to determine a more effective distribution of oscillators. This approach proposes the assessment of the specific mode shape targeted for vibration attenuation to determine a near-optimal distribution of the oscillators. This is achieved by matching the oscillator distribution to the regions with the highest relative displacements observed in a specific

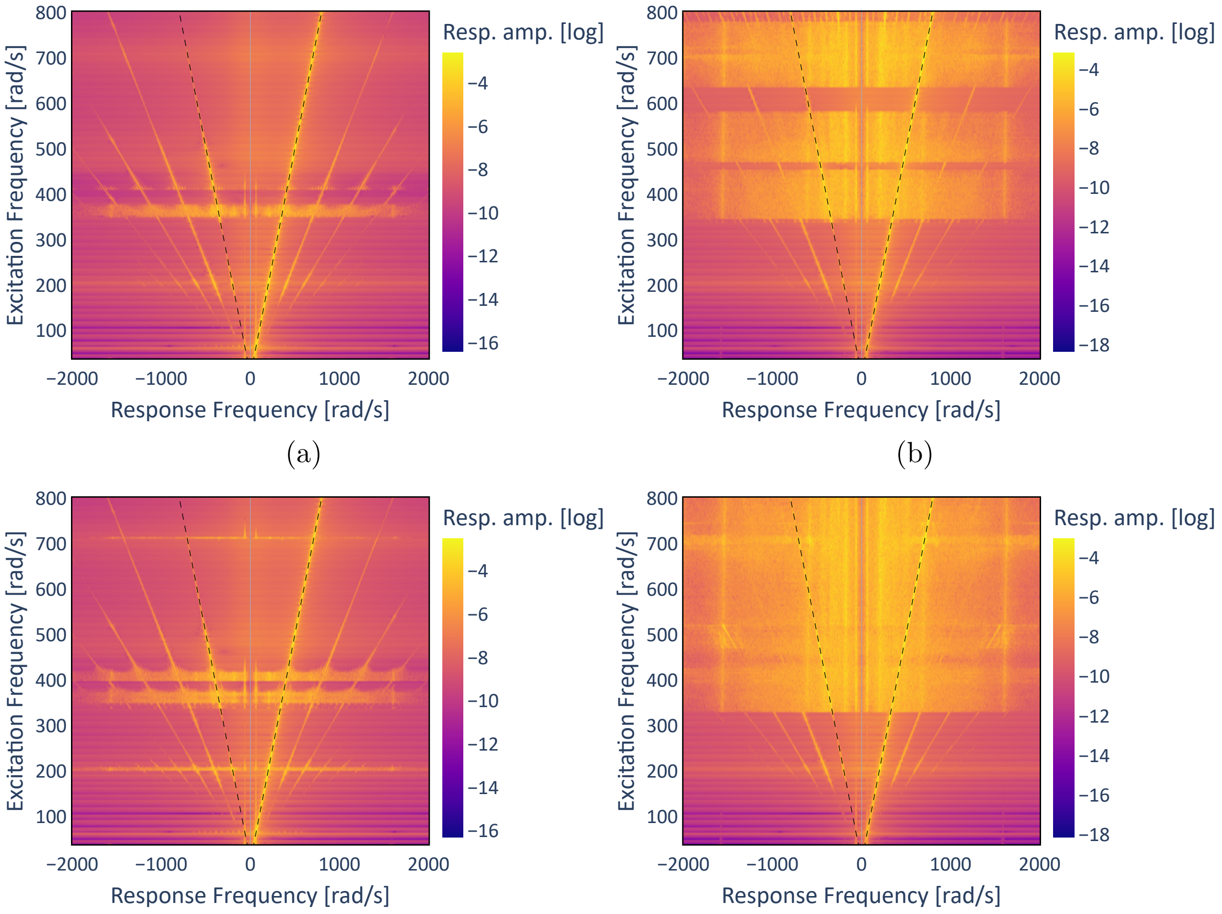

(a) (b) (c) (d)

Figure 6.11 – Full spectrum waterfall heatmaps for the right-most element response. (a) Forward excitation of 400 N. (b) Unbalance excitation of $4U$. (c) Forward excitation of 500 N. (d) Unbalance excitation of $6U$.

mode shape. This strategy is henceforth referred to as Modally Matched Distribution (MMD). The fundamental vibration attenuation mechanisms of periodic oscillators, in linear or nonlinear configurations, rely primarily on energy transfer from the base structure to the oscillators (BRANDÃO; de Paula; FABRO, 2022; BRANDÃO; de Paula; FABRO, 2024). The core idea behind the MMD strategy is to take advantage of this principle by positioning the oscillators in locations that most effectively promote this energy transfer.

By comparing the originally proposed oscillator distribution in Figure 6.1 with the target mode shape presented in Figure 6.4 it becomes clear that the oscillators are positioned on nodes with relatively small modal contribution. A second distribution is defined by shifting the oscillators from their original assigned positions toward the ends of the rotor, where modal displacements are higher. This results in the final configuration shown in Figure 6.12.

The new configuration has a significant influence on the rotor's original frequency response profile, reducing the third backward and forward modes from 382 rad/s and 432 rad/s to 204 rad/s and 308 rad/s, respectively. However, the mode shapes of these natural frequencies are only slightly affected by the new proposed configuration.

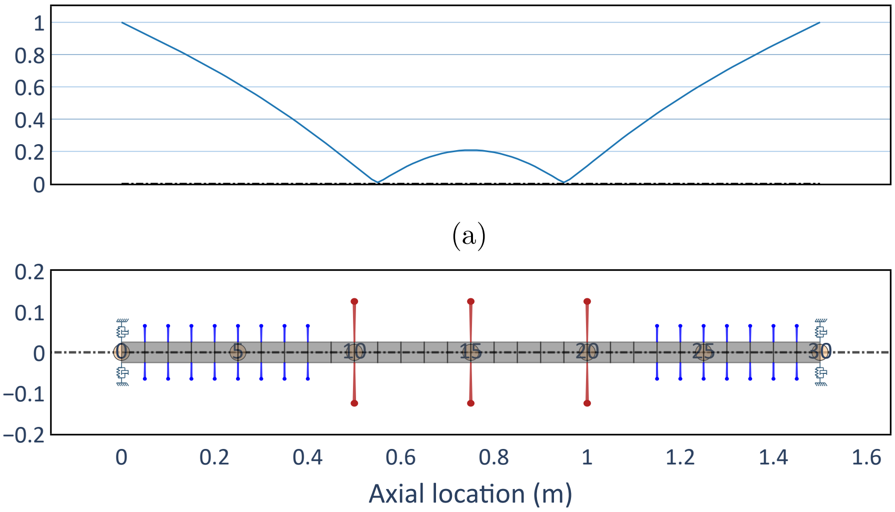

(a)

(b)

Figure 6.12 – Oscillators positioning with Modally Matched Distribution (MMD). (a) Shows the mode shape of the target natural frequency and (b) shows the adjusted distribution of oscillators.

To target the new 308 rad/s forward natural frequency, the oscillator tuning frequency is set to $\omega_0 = 330$ rad/s, introducing a deliberate frequency offset. This offset enhances attenuation performance due to the asymmetric influence of the bi-stable oscillators on the acoustic and optical modes, as briefly discussed in Section 6.2.1. This strategy of deliberately tuning the oscillators to a frequency slightly above the target natural frequency leverages this asymmetry to achieve a significantly broader vibration attenuation bandwidth.

Figure 6.13 compares the system's unbalance response with the unbalance magnitude of $4U$ and ω_0 set at three different values - $\omega_0 = 300$ rad/s, $\omega_0 = 315$ rad/s and $\omega_0 = 330$ rad/s. A clear improvement in attenuation performance is observed at frequencies higher than 350 rad/s as ω_0 increases, with a significant increase in the width of the bandgap. Setting ω_0 to a higher frequency seems to have the effect of delaying the optical (post-bandgap) onset of chaotic behavior, while maintaining the acoustic (pre-bandgap) behavior almost unchanged. Only the $4U$ unbalance case is presented to illustrate the phenomenon, but the same behavior has been observed for all other excitation conditions that were simulated.

Figures 6.14 and 6.15 show the FRFs with forward and backward excitations and oscillators positioned with MMD. These results demonstrate more consistent attenuation, with reduced performance degradation at higher frequencies and more uniform attenuation of lower natural frequency peaks, including those not targeted by the MMD.

Figure 6.16a illustrates the unbalance response, revealing an even stronger attenuation effect. Especially at higher unbalance magnitudes, such as $6U$ and $10U$, the resonance peaks above 200 rad/s are almost completely neutralized, leading to a flat frequency response profile. When the performance of graded oscillators is compared to

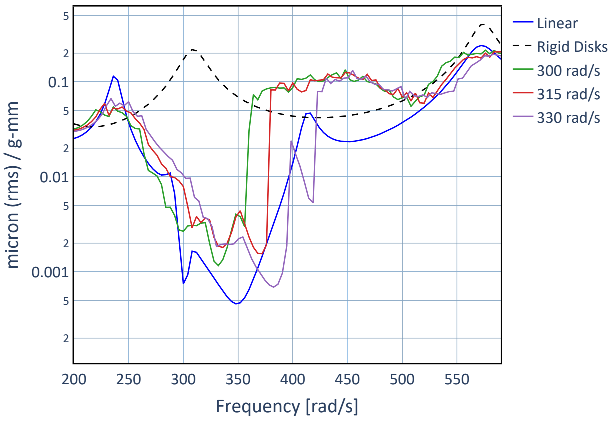

Figure 6.13 – Unbalance response comparison for different values of ω_0. The unbalance is set at $4U$ and the linear case uses $\omega_0 = 300$ rad/s.

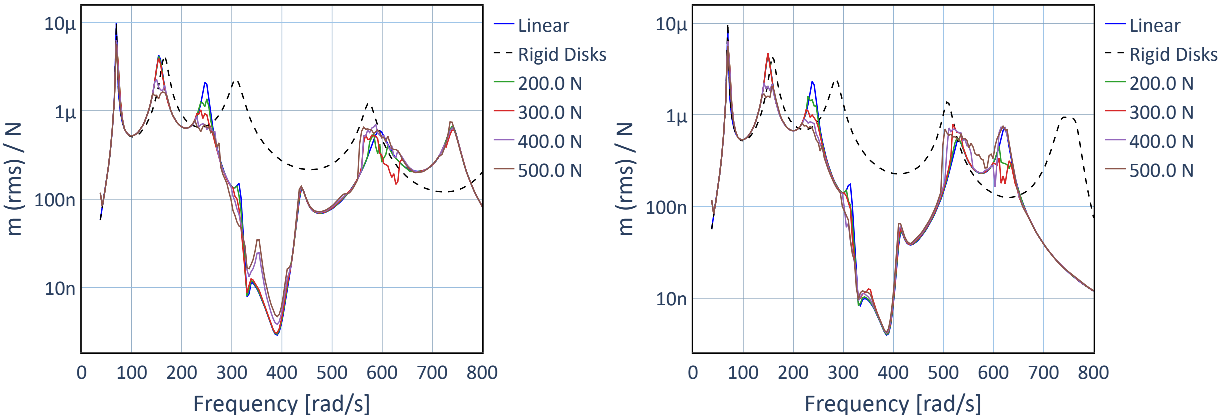

(a)

(b)

Figure 6.14 – Frequency Response Functions for (a) forward and (b) backward excitations and identical oscillators with MMD.

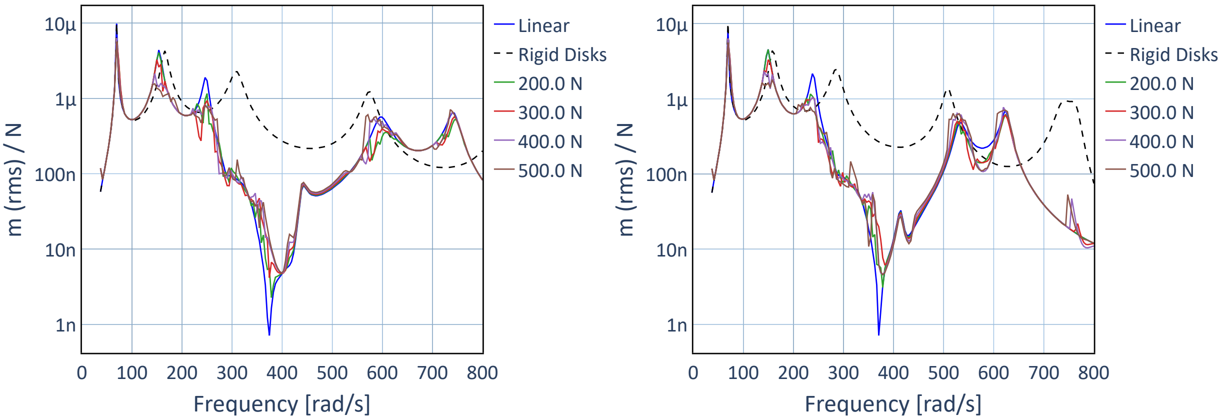

(a)

(b)

Figure 6.15 – Frequency Response Functions for (a) forward and (b) backward excitations and graded oscillators with MMD.

that of uniform oscillators, there is no significant difference, except for a slightly earlier onset of chaotic behavior and consequently the FRF flattening effect.

Figure 6.17 presents orbit plots and Poincaré maps for $\Omega = 250$ rad/s and $\Omega = 730$

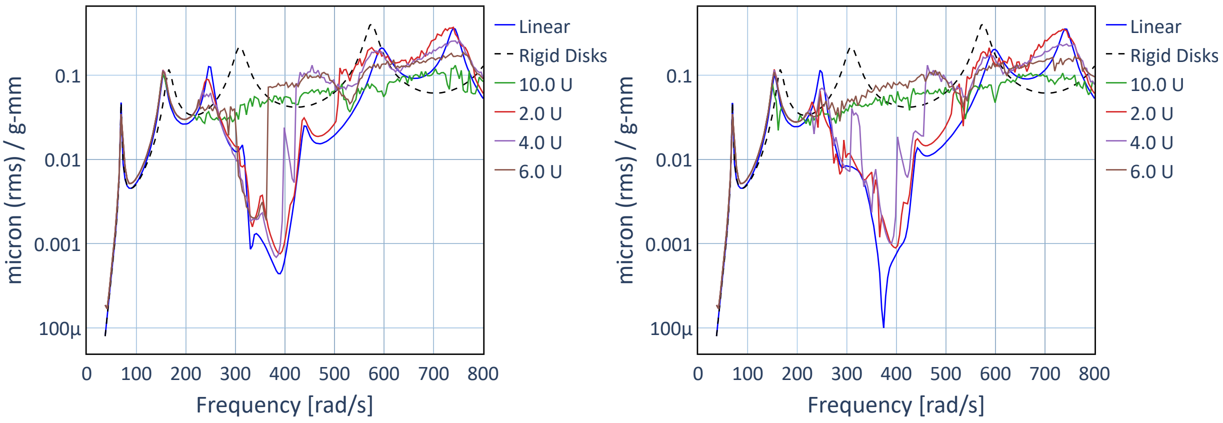

(a) (b)

Figure 6.16 – Frequency Response Functions for unbalance excitation. (a) Identical oscillators and (b) graded oscillators, both with MMD.

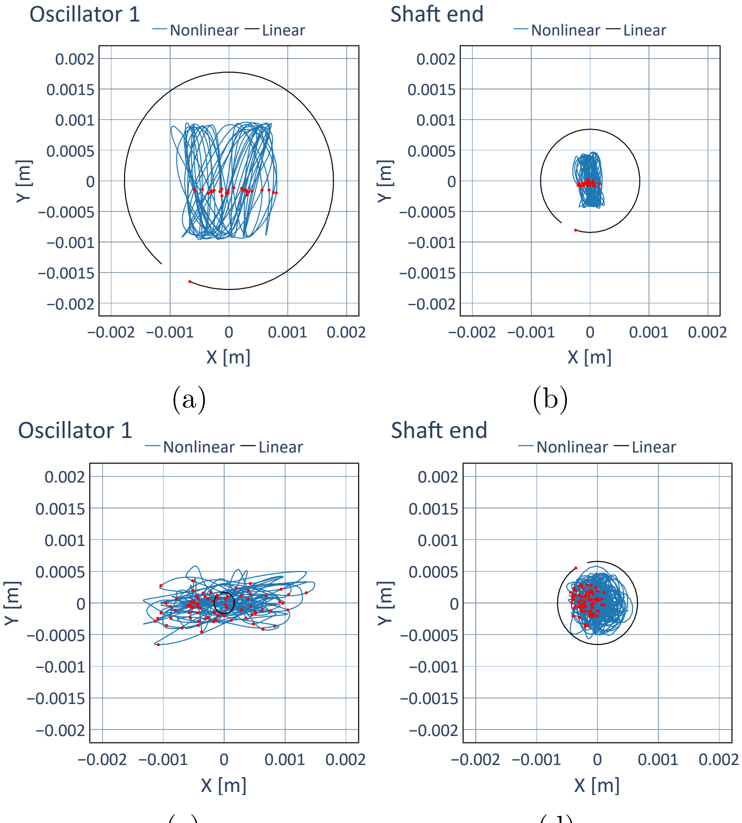

(a) (b)

(c) (d)

Figure 6.17 – Orbit plots of oscillator 1 (left) and shaft end (right) for linear and nonlinear oscillators with MMD. All cases are for identical resonators under $10U$ unbalance excitation. Excitation frequencies are 250 rad/s for (a) and (b) and 730 rad/s for (c) and (d).

rad/s. The results lead to conclusions similar to those drawn from Figure 6.8. However, in this case, the improved MMD arrangement activates the oscillator dynamics more effectively in the vertical direction, resulting in an enhanced attenuation even for excitation frequencies above ω_0.

Figure 6.18 presents the average amplification and phase angle heat maps for the

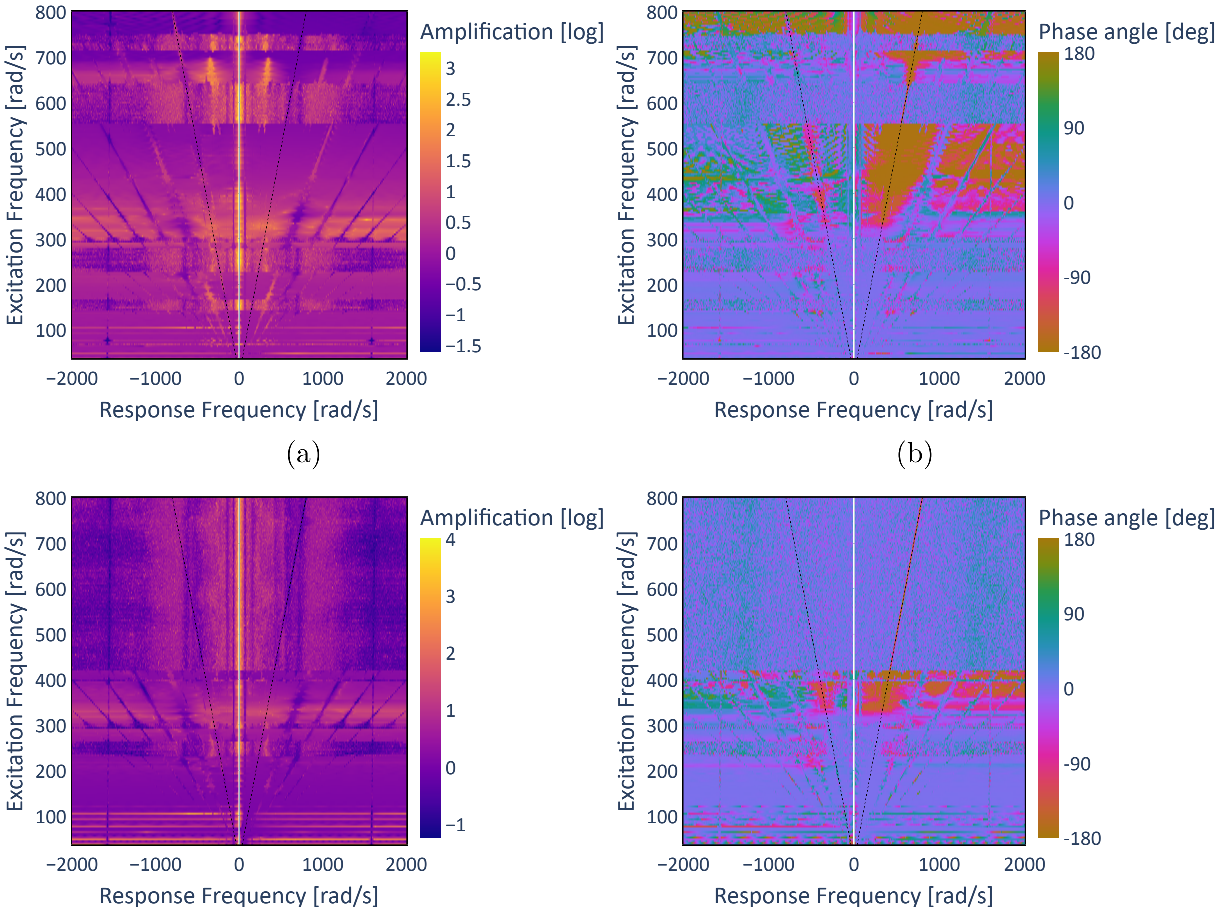

(a) (b)

(c) (d)

Figure 6.18 – Averaged amplification and phase angle plots for high excitation amplitude and oscillator with MMD. (a) Averaged amplification heatmap and (b) phase angle map for forward excitation of 500 N. (c) Averaged amplification heatmap and (d) phase angle map for unbalance excitation of $4U$.

system with MMD under both 500 N forward and $4U$ unbalance excitation conditions. Notably, especially in the attenuation ranges, there is an asymmetric behavior of the phase angle for the forward and backward components. This asymmetry is even more evident when the averaged amplification and phase angle analysis is focused on the first 3 oscillators, the ones on the left, closer to the excitation source. Figure 6.19 shows the same heatmaps, but with only the average of the first 3 oscillators. This highlights the effects on the most affected elements, and arguably the ones that contribute the most to the overall vibration attenuation behavior.

The overall phase angle profile is significantly different and exhibits more pronounced asymmetries between the forward and backward components. Based on the well-described linear attenuation mechanism discussed in previous sections, we know that a very effective attenuation mechanism takes place when the oscillators have 90° phase delay relative to the rotor. In the heatmaps of Figure 6.19 this linear analogy can be assessed by identifying the bright pink areas around the synchronous line, which correspond to $-90°$. These areas are often concentrated on both sides of the spectrum, such as around the tuning frequency $\omega_0 = 330$ rad/s. In other cases, it appears only on the backward or forward sides, such as between 330 rad/s and 400 rad/s. This indicates that the forward and backward components of the rotor response are activated in dissimilar ways under some excitation conditions, especially when the nonlinear behavior becomes more evident. This may be the key to the unique bandgap widening effect observed in this system.

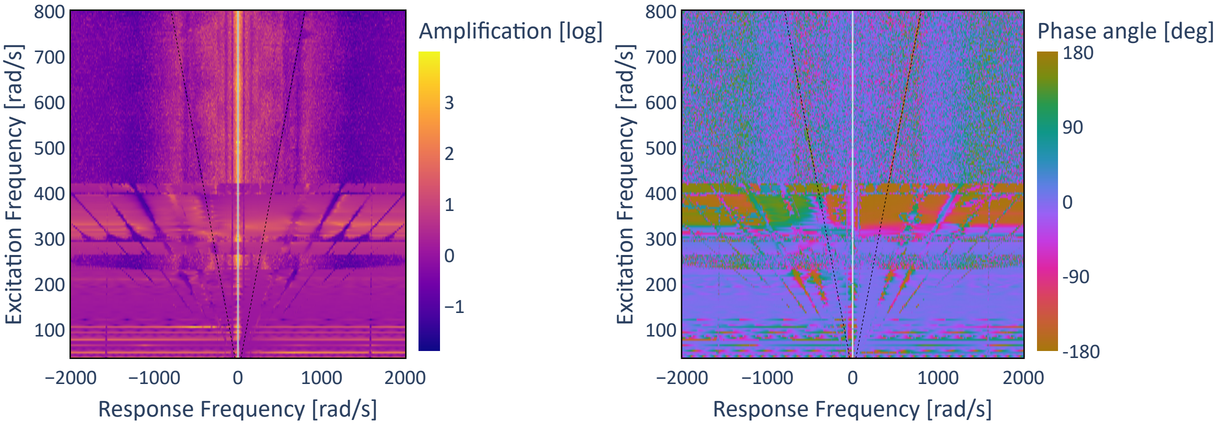

(a)

(b)

Figure 6.19 – Amplification and phase angle averaged of the first three oscillators at high excitation amplitude and oscillator with MMD. (a) Averaged amplification heatmap and (b) phase angle map for unbalance excitation of $4U$.

Comparing the full spectrum waterfall plots for the system with MMD, shown in Figure 6.11, to those presented in Figure 6.20, it is clear that the latter reveals a much richer dynamic behavior. This reinforces the correlation between nonlinear behaviors, such as chaos and multi-harmonic periodic responses, and improved attenuation performance.

An example of the complex dynamics of the system is shown in the Poincaré map in Figure 6.21, corresponding to the condition displayed in Figure 6.11a at an excitation frequency of 600 rad/s. This map displays unique and characteristic patterns that emerge from the system's chaotic response.

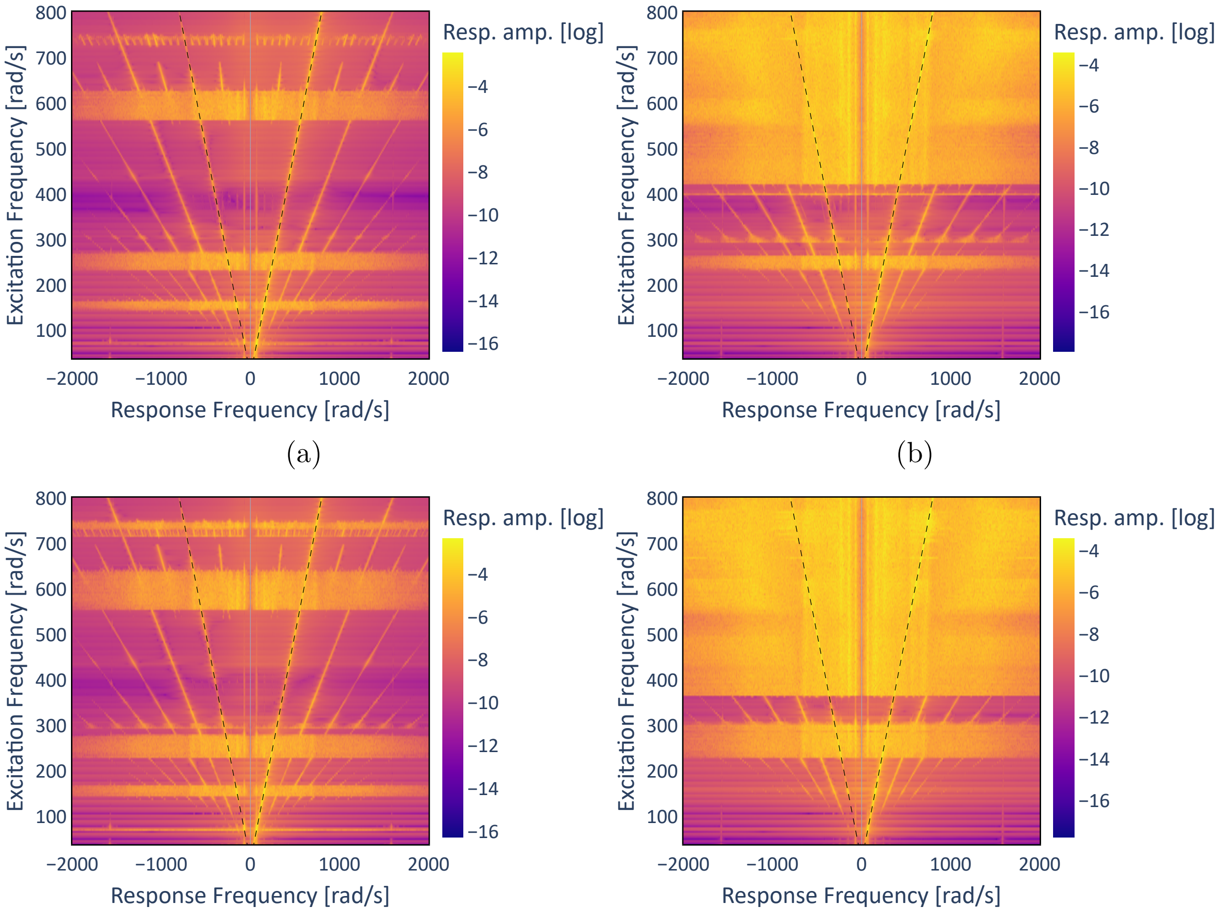

(a) (b)

(c) (d)

Figure 6.20 – Full spectrum waterfall heatmaps for the right-most element response in the system with MMD. (a) Forward excitation of 400 N. (b) Unbalance excitation of $4U$. (c) Forward excitation of 500 N. (d) Unbalance excitation of $6U$.

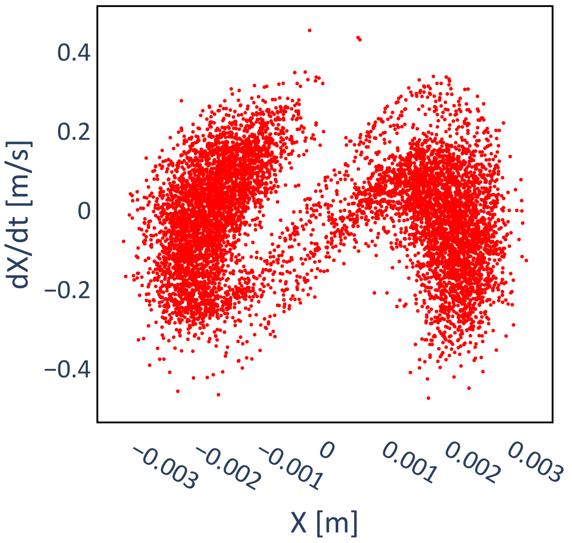

Figure 6.21 – Poincaré map for the X-direction motion of the first oscillator with forward excitation at 400 N amplitude and 600 rad/s frequency.

In terms of a qualitative assessment of the attenuation performance, the results may be evaluated in three separate aspects: (1) **linear resonators** attenuation bandwidth, (2) nonlinear oscillators attenuation of **acoustic modes** (below linear bandgap), and (3) nonlinear oscillators oscillators attenuation of **optical modes** (above linear bandgap).

The attenuation bandwidth with **linear resonators** was dramatically improved. This supports the conclusion that the MMD strategy positively influences the fundamental mechanisms of vibration attenuation in locally resonant structures, in general, and is not limited to nonlinear arrangements. Intuitively, this observation shows that the energy transfer mechanisms between the resonators and the base structure are significantly enhanced when the resonators are placed at locations on the rotor with higher levels of available kinetic energy.

The vibration attenuation behavior of **acoustic modes** with nonlinear oscillators is quite similar between MMD and non-MMD configurations. A consistent reduction is observed in the vibration peak immediately below the linear bandgap. In some cases, attenuation of the second natural frequency peak is also observed in both configurations.

However, the vibration attenuation behavior of **optical modes** with nonlinear oscillators has been somewhat influenced. In general, earlier and more consistent onset of chaos was observed in the MMD cases, which leads to a clearer manifestation of the *flattening* effect of higher frequency vibration peaks, especially for higher excitation amplitude cases.

Regarding the deliberate offset frequency demonstrated in Figure 6.13, it is worth noting that although this tuning strategy was applied only in the context of the MMD configuration, its underlying principle is not exclusive to MMD. Consequently, this approach is likely to yield beneficial results in other nonlinear oscillator configurations exhibiting similar asymmetry. However, the results presented are specific to the studied case, and further investigation is required to assess the scalability of this tuning strategy across a broader range of applications.

6.2.3 Attenuation bandwidth comparison

A comparison of all FRFs presented so far reveals the significant advantages of both nonlinear oscillators and the MMD strategy. Figure 6.22 shows an overall comparison of the attenuation bandwidths for the different cases that were evaluated.

The attenuation bandwidth values were determined by comparing each FRF with and without oscillators and identifying the range around ω_0 where vibration reduction occurs. For the nonlinear cases, the average bandwidth across all forcing magnitudes was considered for each evaluated condition. The improvements in vibration attenuation are evident, even though the evaluated attenuation bandwidth does not capture the attenuation of peaks further away from ω_0, such as those at the second and fourth natural frequencies.

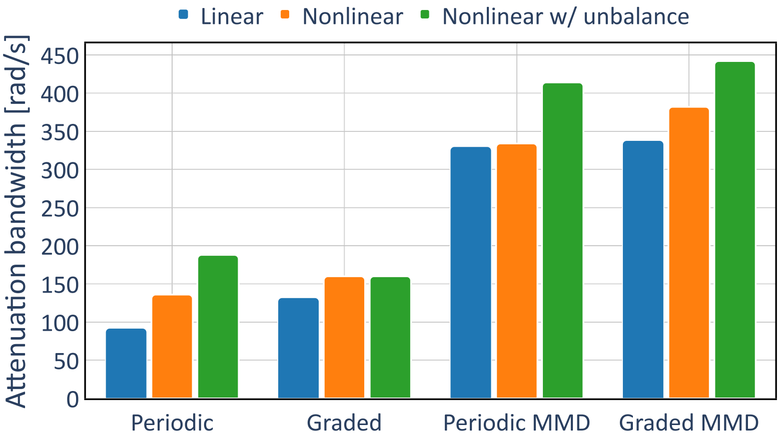

Figure 6.22 – Bar chart showing a comparison of attenuation bandwith for the different configurations.

6.3 Final Remarks

This last chapter concludes the thesis with the combination of all the main concepts introduced in the previous steps, revealing new phenomena, and proposing solutions and optimized strategies for the design of the nonlinear metastructure. This final consolidated approach determined some of the advantages and limitations of this concept.

The main findings and contribution of this final step are summarized below.

- The proposed concept of nonlinear oscillators consistently improves attenuation for frequencies immediately below the linear bandgap range.
- For frequencies above the linear bandgap range, the performance remained unchanged or, in some cases, deteriorated.
- A strategy of shifting the tuning frequency, ω_0, to a value slightly higher than the original target frequency proved to be a useful tool to overcome this disadvantage.
- Asymmetric behaviors between forward and backward whirl components revealed how nonlinear oscillators interact differently with these distinct modes of rotation.
- Unbalance response analysis was performed, indicating slightly improved results compared to unitary excitation.
- The unbalance analysis following the design philosophy of API TR 684-1 (2019) showed that a bi-stable eccentricity of 0.5 mm can be enough to produce significant vibration attenuation.
- The proposed MMD strategy proved to be a powerful tool for improving vibration attenuation without modification of the total oscillator-to-rotor mass ratio.

7 Conclusions

This thesis has systematically investigated the complex dynamic behaviors and vibration attenuation mechanisms in periodic structures, with a particular focus on the interplay between gyroscopic effects and nonlinear dynamics. Through a progressive exploration, adding complexity at each step, we have unveiled novel phenomena and developed innovative approaches that significantly enhance our understanding of mechanical metastructures and pave the way for future practical applications. This step-by-step went through 3 specific stages of increasing complexity, the conclusions of which are presented in the following sections.

7.1 Linear gyroscopic resonators

The investigation, thoroughly described in Chapter 4, examined linear gyroscopic metastructures, where we extended the concept of periodic locally resonant structures to rotating systems. We demonstrated that such arrangements can effectively create frequency bandgaps, providing substantial vibration attenuation effects.

Using the same general concept of resonators, two different dynamics were explored by changing the relevant DoFs that provided the elastic attachment between rotor and resonator. This allowed the gyroscopic effects to be isolated in only one of the cases, providing a clear understanding of how these effects affect the system's behavior.

The implementation of rainbow-type configurations (with graded resonator properties) yielded remarkable results, increasing the bandgap width by approximately 60% compared to simple arrangements of identical resonators.

When the radial (translational) DoFs were chosen for the elastic connection, the resonators were shown to provide strong attenuation capabilities for both backward and forward excitation in the same frequency range. However, when the rotational DoFs were of interest, the distinction between forward and backward motion becomes predominant, and the attenuation ranges are separated.

Still in the rotational resonators case, the transition from acoustic to optical modes were observed to be dependent on the rotation speed and whirl direction (forward or backward), leading to the coexistence of acoustic and optical modes at certain zones in the

Campbell Diagram. This particularly interesting discovery has previously been unreported for rotating metastructures.

A case study was presented using industry standard design practices to apply the concept of linear periodic resonators to a turboexpander compressor model. The evaluation showed that the resonators effectively attenuate vibration in the target frequency range, neutralizing the amplification of the first critical speed and allowing compliance with the vibration amplitude acceptance criteria defined by API Std 617 (2022). Finally, we demonstrate that, although providing increased attenuation bandwidth, the rainbow arrangement of resonators is not always the best choice, especially for applications in which the attenuation depth is more important than its bandwidth.

7.2 Nonlinear 1-D oscillators

In a second step, in Chapter 5, the introduction of nonlinearities in the system dynamics was investigated by including bistable Duffing-type oscillators attached to a one-dimensional periodic lattice. In this case gyroscopic effects were naturally not present, since the simple 1-D lattice system does not rotate. The main purpose in this case was to isolate the aspects related solely to nonlinearities by applying this concept to a very simple base structure. This should allow for the characterization of main fundamental phenomena and guide further, more complex steps of investigation.

Our findings revealed that these nonlinear systems exhibit amplitude-dependent response patterns with distinct attenuation mechanisms compared to their linear counterparts. While linear systems rely primarily on phase relationships for vibration attenuation, nonlinear systems demonstrate remarkable capabilities to redistribute energy across multiple frequency scales, particularly in chaotic regimes. This energy dispersion mechanism creates ultra-broadband attenuation effects that would most likely be unattainable with typical, purely linear arrangements. This observation was made possible by the analysis of averaged amplification and phase angle frequency maps, which is a tool developed and proposed in the course of this work.

Finally, we established that graded configurations of nonlinear resonators further enhance this broadband attenuation by activating different sections of the resonator array at different frequencies.

7.3 Nonlinear gyroscopic oscillators

In a final converging step, explored in Chapter 6, the innovative integration of these concepts is investigated, combining nonlinear bistable oscillators with gyroscopic effects in rotating structures. The fundamental behavior characteristics of the nonlinear and chaotic vibration attenuation phenomena, as explored in the previous step, could be reproduced in this case. However, the combination with a more complex base structure dynamics presented unique challenges and opportunities that led to several significant contributions.

We introduced the concept of Modally Matched Distribution (MMD), a strategic positioning of oscillators aligned with the target mode shapes, which substantially improved vibration attenuation without increasing the overall mass ratio. Our investigations also yielded practical insights for implementation in real-world rotating machinery. We demonstrated that careful tuning strategies, such as deliberate frequency offsetting, can significantly increase the overall attenuation bandwidth. These proposals were primarily proposed as a way to overcome or mitigate the observed degradation of vibration attenuation performance in the post-bandgap frequency range. This performance degradation was also not previously reported in the literature, and some hypotheses for its origins were discussed, although further aspects would need to be determined for a complete definition of this phenomenon.

Asymmetric behaviors between forward and backward whirl components, revealing how nonlinear oscillators interact differently with these distinct modes of rotation. The analysis of response under standardized unbalance excitation conditions (following recognized industry standards such as API 617) provided realistic performance metrics that can guide future applications in industrial settings.

7.4 Final remarks

The underlying physical mechanisms uncovered in this work represent a significant advancement in our understanding of complex dynamic systems. We have shown that chaotic behavior, often considered detrimental in engineering applications, can be harnessed constructively to achieve superior vibration attenuation. The energy frequency-scale redistribution that occurs during chaotic response may effectively transform harmful concentrated vibration energy into broadly distributed, lower-amplitude oscillations.

Looking ahead, this research opens several promising directions for future research. The experimental validation of these numerical findings would be a natural next step, particularly focusing on the practical implementation challenges of bistable oscillators in rotating environments. Additionally, optimization of the MMD strategy and extension to more complex rotor geometries could further enhance the applicability of these concepts. The potential for active or semi-active tuning of the bistable oscillators also presents an intriguing avenue for adaptive vibration control systems that could respond to changing operational conditions.

This thesis has demonstrated that the integration of nonlinear dynamics, gyroscopic effects, and strategic positioning in metastructures can create powerful synergies for vibration control in rotating machinery. The fundamental understanding developed here not only contributes to the theoretical body of knowledge in nonlinear dynamics but also provides practical design principles for next-generation vibration attenuation systems in high-performance rotating machinery.

Bibliography

ALAM, M. S. et al. A new analytical technique to find periodic solutions of non-linear systems. *International Journal of Non-Linear Mechanics*, Elsevier, v. 42, n. 8, p. 1035–1045, 2007. Cited on page 33.

ALSAFFAR, Y. et al. Band gap characteristics of periodic gyroscopic systems. *Journal of Sound and Vibration*, Academic Press, v. 435, p. 301–322, nov 2018. ISSN 0022-460X. Cited on page 14.

ANIGBOGU, W.; BARDAWEEL, H. A metamaterial-inspired structure for simultaneous vibration attenuation and energy harvesting. *Shock and Vibration*, v. 2020, p. –, 2020. Cited on page 13.

API Std 610. *API Std 610 - Centrifugal Pumps for Petroleum, Petrochemical, and Natural Gas Industries.* [S.l.], 2021. 12th Ed. Cited on page 92.

API Std 617. *Axial and Centrifugal Compressors and Expander-compressors.* [S.l.], 2022. 9th Ed. Cited 4 times on pages xii, 61, 92, and 107.

API TR 684-1. *API TR 684-1 - Rotordynamic Tutorial: Lateral Critical Speeds, Unbalance Response, Stability, Train Torsionals, and Rotor Balancing.* [S.l.], 2019. Rev. 1. Cited 2 times on pages 92 and 105.

ATTARZADEH, M. A. et al. Non-reciprocal wave phenomena in energy self-reliant gyric metamaterials. *The Journal of the Acoustical Society of America*, Acoustical Society of America ASA, v. 146, n. 1, p. 789, jul 2019. ISSN 0001-4966. Disponível em: <https://asa.scitation.org/doi/abs/10.1121/1.5114916>. Cited 2 times on pages 14 and 44.

BABA, T. et al. Light localizations in photonic crystal line defect waveguides. *IEEE Journal of Selected Topics in Quantum Electronics*, v. 10, n. 3, p. 484–491, 2004. Cited on page 6.

BAILY, E. M. *Steady-state harmonic analysis of nonlinear networks.* [S.l.]: Stanford University, 1968. Cited on page 33.

BARAVELLI, E.; RUZZENE, M. Internally resonating lattices for bandgap generation and low-frequency vibration control. *Journal of Sound and Vibration*, Elsevier, v. 332, n. 25, p. 6562–6579, 2013. Cited on page 22.

BAZ, A. Active control of periodic structures. *Journal of Vibration and Acoustics, Transactions of the ASME*, v. 123, n. 4, p. 472–479, 2001. Cited on page 13.

BELI, D. et al. Wave attenuation and trapping in 3D printed cantilever-in-mass metamaterials with spatially correlated variability. *Scientific Reports*, v. 9, n. 1,

p. 5617, apr 2019. ISSN 2045-2322. Disponível em: <https://www.nature.com/articles/s41598-019-41999-0>. Cited 3 times on pages 2, 6, and 10.

BENTLY, D. *Fundamentals os Rotating Machinery Diagnostics*. Minden, NV: Bently Pressurized Bearing Press, 2002. Cited on page 15.

BISWAS, R. et al. Impedance of photonic crystals and photonic crystal waveguides. *AIP Journals (American Institute of Physics)*, v. 84, n. 8, p. 1254, 2004. Cited on page 6.

BOECHLER, N. et al. Bifurcation-based acoustic switching and rectification. *Nature materials*, Nature Publishing Group UK London, v. 10, n. 9, p. 665–668, 2011. Cited on page 12.

BRANDÃO, A. et al. Bandgap formation and chaos in periodic lattices with graded bistable resonators. *Journal of the Brazilian Society of Mechanical Sciences and Engineering*, v. 46, n. 2, p. 1806–3691, 2024. Cited 7 times on pages 3, 4, 84, 89, 91, 95, and 97.

BRANDÃO, A. et al. Nonlinear dynamics and chaos of a nonsmooth rotor-stator system. *Mathematical Problems in Engineering*, v. 2017, n. 1, p. 8478951, 2017. Disponível em: <https://onlinelibrary.wiley.com/doi/abs/10.1155/2017/8478951>. Cited on page 14.

BRANDÃO, A. A. et al. Rainbow gyroscopic disk metastructures for broadband vibration attenuation in rotors. *Journal of Sound and Vibration*, Elsevier, v. 532, p. 116982, 2022. Cited 8 times on pages 4, 75, 82, 84, 85, 88, 95, and 97.

BRANDÃO, A. A. et al. Modally matched bistable disk metastructure for vibration attenuation in rotors: bandwidth widening and chaos. *Nonlinear Dynamics*, Springer Nature, 2025. Cited 2 times on pages 4 and 84.

BRILLOUIN, L. *Wave Propagation in Periodic Structures*. U.S.A.: McGraw-Hill Book Company, Inc., 1946. Cited 2 times on pages 2 and 21.

CAI, G.; LIN, Y. Localization of wave propagation in disordered periodic structures. *AIAA journal*, v. 29, n. 3, p. 450–456, 1991. Cited 2 times on pages 2 and 10.

CAMPBELL, W. *Protection of steam turbine disk wheels from axial vibration*. [S.l.]: General electric Company, 1924. Cited on page 32.

CELLI, P. et al. Bandgap widening by disorder in rainbow metamaterials. *Applied Physics Letters*, v. 114, p. 91903, 3 2019. ISSN 0003-6951. Disponível em: <https://aip.scitation.org/doi/abs/10.1063/1.5081916>. Cited 2 times on pages 6 and 7.

CHAN, K. et al. Helical structure of the waves propagating in a spinning timoshenko beam. *Proceedings of the Royal Society A: Mathematical, Physical and Engineering Sciences*, The Royal Society London, v. 461, n. 2064, p. 3913–3934, 2005. Cited on page 14.

CHASALEVRIS, A.; DOHNAL, F. Improving stability and operation of turbine rotors using adjustable journal bearings. *Tribology International*, v. 104, p. 369–382, 2016. ISSN 0301-679X. Disponível em: <https://www.sciencedirect.com/science/article/pii/S0301679X16301943>. Cited on page 15.

CHATELET, E. et al. A three dimensional modeling of the dynamic behavior of composite rotors. *International Journal of Rotating Machinery*, v. 8, n. 3, p. 805189, 2002. Disponível em: <https://onlinelibrary.wiley.com/doi/abs/10.1155/S1023621X02000179>. Cited on page 14.

COLOMBI, A. et al. A seismic metamaterial: The resonant metawedge. *Scientific reports*, v. 6, n. 1, p. 1–6, 2016. Cited on page 11.

COLOMBI, A. et al. Forests as a natural seismic metamaterial: Rayleigh wave bandgaps induced by local resonances. *Scientific Reports*, v. 6, 2016. Cited 2 times on pages 10 and 11.

CREMER, L. et al. Attenuation of structure-borne sound. In: _____. *Structure-Borne Sound: Structural Vibrations and Sound Radiation at Audio Frequencies*. Berlin, Heidelberg: Springer Berlin Heidelberg, 2005. p. 341–448. ISBN 978-3-540-26514-6. Disponível em: <https://doi.org/10.1007/3-540-26514-7_6>. Cited on page 6.

DALELA, S. et al. A review on application of mechanical metamaterials for vibration control. *Mechanics of Advanced Materials and Structures*, Taylor Francis, p. 1–26, feb 2021. ISSN 1537-6494. Disponível em: <https://www.tandfonline.com/doi/full/10.1080/15376494.2021.1892244>. Cited on page 7.

DELGADO, A.; ERTAS, B. Dynamic characterization of a novel externally pressurized compliantly damped gas-lubricated bearing with hermetically sealed squeeze film damper modules. *Journal of Engineering for Gas Turbines and Power*, American Society of Mechanical Engineers Digital Collection, v. 141, n. 2, p. –, 2019. Cited on page 15.

DELLACORTE, C.; BRUCKNER, R. J. Remaining technical challenges and future plans for oil-free turbomachinery. *Journal of engineering for gas turbines and power*, American Society of Mechanical Engineers Digital Collection, v. 133, n. 4, p. –, 2011. Cited 2 times on pages 3 and 15.

DENG, B. et al. Nonlinear waves in flexible mechanical metamaterials. *Journal of Applied Physics*, AIP Publishing, v. 130, n. 4, 2021. Cited on page 11.

DETROUX, T. et al. The harmonic balance method for bifurcation analysis of large-scale nonlinear mechanical systems. *Computer Methods in Applied Mechanics and Engineering*, v. 296, p. 18–38, 2015. ISSN 0045-7825. Disponível em: <https://www.sciencedirect.com/science/article/pii/S0045782515002297>. Cited on page 33.

DEYMIER, P. A. *Acoustic metamaterials and phononic crystals*. [S.l.]: Springer Science & Business Media, 2013. v. 173. Cited on page 22.

DING, H.; CHEN, L.-Q. Designs, analysis, and applications of nonlinear energy sinks. *Nonlinear Dynamics*, Springer, v. 100, n. 4, p. 3061–3107, 2020. Cited on page 13.

DONG, Z. et al. Enhancement of wave damping for metamaterial beam structures with embedded inerter-based configurations. *Applied Acoustics*, Elsevier, v. 178, p. 108013, 2021. Cited on page 10.

ELMADIH, W. et al. Three-dimensional resonating metamaterials for low-frequency vibration attenuation. *Scientific reports*, Nature Publishing Group UK London, v. 9, n. 1, p. 11503, 2019. Cited on page 22.

ERTAS, B. Compliant hybrid gas bearing using integral hermetically sealed squeeze film dampers. *Journal of Engineering for Gas Turbines and Power*, American Society of Mechanical Engineers, v. 141, n. 10, p. 101020, 2019. Cited on page 15.

ERTAS, B.; DELGADO, A. Hermetically sealed squeeze film damper for operation in oil-free environments. *Journal of Engineering for Gas Turbines and Power*, American Society of Mechanical Engineers Digital Collection, v. 141, n. 2, p. –, 2019. Cited on page 15.

ERTAS, B.; GARY, K. Frequency dependancy of dynamic force coefficients for hermetic squeeze film dampers utilizing fluid-bounding flexible structures. In: . Virtual Conference: [s.n.], 2021. (Turbo Expo: Power for Land, Sea, and Air, Volume 9A: Structures and Dynamics — Aerodynamics Excitation and Damping; Bearing and Seal Dynamics; Emerging Methods in Design and Engineering), p. –. V09AT24A020. Disponível em: <https://doi.org/10.1115/GT2021-60007>. Cited on page 15.

FABRO, A. T. et al. Wave and vibration analysis of elastic metamaterial and phononic crystal beams with slowly varying properties. *Wave Motion*, Elsevier B.V., v. 103, p. 102728, jun 2021. ISSN 01652125. Cited 3 times on pages 6, 45, and 78.

FABRO, A. T. et al. Correlated disorder in rainbow metamaterials for vibration attenuation. *Proceedings of the Institution of Mechanical Engineers, Part C: Journal of Mechanical Engineering Science*, SAGE PublicationsSage UK: London, England, v. 235, p. 2610–2621, 5 2021. ISSN 20412983. Disponível em: <http://journals.sagepub.com/doi/10.1177/0954406220986596>. Cited 3 times on pages 6, 7, and 25.

FANG, X. et al. Ultra-low and ultra-broad-band nonlinear acoustic metamaterials. *Nature Communications*, v. 8, p. 1288, 11 2017. ISSN 20411723. Disponível em: <https://www.nature.com/articles/s41467-017-00671-9>. Cited 3 times on pages 12, 73, and 77.

FANG, X. et al. Broadband and tunable one-dimensional strongly nonlinear acoustic metamaterials: Theoretical study. *Physical Review E*, American Physical Society, v. 94, p. 052206, 11 2016. ISSN 24700053. Disponível em: <https://journals.aps.org/pre/abstract/10.1103/PhysRevE.94.052206>. Cited 4 times on pages 12, 73, 77, and 91.

FILIPPOV, A. Das problem der laval'shen turbinewelle. *Civilingenieur*, p. 332–342, 1895. Cited on page 26.

FLOQUET, G. Sur les équations différentielles linéaires à coefficients périodiques. In: *Annales scientifiques de l'École normale supérieure*. [S.l.: s.n.], 1883. v. 12, p. 47–88. Cited on page 37.

GARY, K.; ERTAS, B. Experimental rotordynamic force coefficients for a diffusion bonded compliant hybrid journal gas bearing utilizing fluid-filled hermetic dampers. *Journal of Engineering for Gas Turbines and Power*, American Society of Mechanical Engineers Digital Collection, v. 142, n. 4, p. –, 2020. Cited on page 15.

HE, M. *Thermoelastohydrodynamic analysis of fluid film journal bearing*. 2003. PhD thesis — University of Virginia, Charlottesville, VA. Cited on page 61.

HODGES, C. Confinement of vibration by structural irregularity. *Journal of sound and vibration*, v. 82, n. 3, p. 411–424, 1982. Cited 2 times on pages 2 and 10.

HODGES, C.; WOODHOUSE, J. Vibration isolation from irregularity in a nearly periodic structure: Theory and measurements. *The Journal of the Acoustical Society of America*, v. 74, n. 3, p. 894–905, 1983. Cited on page 10.

HOSEN, M. A. et al. An analytical technique for solving a class of strongly nonlinear conservative systems. *Applied Mathematics and Computation*, Elsevier, v. 218, n. 9, p. 5474–5486, 2012. Cited on page 33.

HUSSEIN, M. I. et al. Dynamics of phononic materials and structures: Historical origins, recent progress, and future outlook. *Applied Mechanics Reviews*, American Society of Mechanical Engineers Digital Collection, v. 66, n. 4, p. –, 2014. Cited on page 7.

HWANG, M.; ARRIETA, A. F. Extreme frequency conversion from soliton resonant interactions. *Phys. Rev. Lett.*, American Physical Society, v. 126, p. 073902, Feb 2021. Disponível em: <https://link.aps.org/doi/10.1103/PhysRevLett.126.073902>. Cited on page 12.

ISO 1940-1. *ISO 1940-1 - Mechanical vibration — Balance quality requirements for rotors in a constant (rigid) state - Part 1: Specification and verification of balance tolerances.* [S.l.], 2003. 2nd Ed. Cited on page 92.

JEFFCOTT, H. The lateral vibration of loaded shafts in the neighbourhood of a whirling speed-the effect of want of balance [j]. *Phil. Mag*, v. 37, p. 304, 1919. Cited 3 times on pages 25, 26, and 28.

JENSEN, K. M.; SANTOS, I. F. Design of actively-controlled oil lubrication to reduce rotor-bearing-foundation coupled vibrations - theory & experiment. *Proceedings of the Institution of Mechanical Engineers, Part J: Journal of Engineering Tribology*, v. 236, n. 8, p. 1493–1510, 2022. Cited on page 15.

JOANNOPOULOS, J. D. et al. Photonic crystals. *Solid State Communications*, Elsevier, v. 102, n. 2-3, p. 165–173, 1997. Cited on page 6.

KANAMARU, T. Duffing oscillator. *Scholarpedia*, v. 3, n. 3, p. 6327, 2008. Revision #91210. Cited on page 71.

KIM, T. et al. Super- and sub-harmonic response calculations for a torsional system with clearance nonlinearity using the harmonic balance method. *Journal of Sound and Vibration*, v. 281, n. 3, p. 965–993, 2005. ISSN 0022-460X. Disponível em: <https://www.sciencedirect.com/science/article/pii/S0022460X04002378>. Cited on page 35.

KRÖDEL, S. et al. Wide band-gap seismic metastructures. *Extreme Mechanics Letters*, v. 4, p. 111–117, 2015. Cited on page 10.

KRODKIEWSKI, J.; SUN, L. Modelling of multi-bearing rotor systems incorporating an active journal bearing. *Journal of Sound and Vibration*, v. 210, n. 2, p. 215–229, 1998. ISSN 0022-460X. Disponível em: <https://www.sciencedirect.com/science/article/pii/S0022460X97913237>. Cited on page 15.

KUSHWAHA, M. S. et al. Theory of acoustic band structure of periodic elastic composites. *Phys. Rev. B*, American Physical Society, v. 49, p. 2313–2322, Jan 1994. Disponível em: <https://link.aps.org/doi/10.1103/PhysRevB.49.2313>. Cited on page 6.

LAMAS, P.; NICOLETTI, R. Wave analysis of rotors with longitudinal periodicity. *Journal of Sound and Vibration*, v. 571, p. 118095, 2024. ISSN 0022-460X. Disponível em: <https://www.sciencedirect.com/science/article/pii/S0022460X23005448>. Cited 3 times on pages 3, 7, and 14.

LAMAS, P. B.; NICOLETTI, R. The band gap formation in rotors with longitudinal periodicity and quasi-periodicity. *Journal of Engineering for Gas Turbines and Power*, v. 144, n. 5, p. 051003, 02 2022. Disponível em: <https://doi.org/10.1115/1.4053193>. Cited on page 14.

LAMAS, P. B.; NICOLETTI, R. Experimental evidence of the band gap formation in rotors with longitudinal periodicity. *Journal of Engineering for Gas Turbines and Power*, v. 145, n. 2, p. 024501, 11 2022. ISSN 0742-4795. Disponível em: <https://doi.org/10.1115/1.4055776>. Cited on page 14.

LAMAS, P. B.; NICOLETTI, R. Optimization of band gaps in rotors with longitudinal periodicity and quasi-periodicity. *Journal of Vibration and Acoustics*, v. 145, n. 2, p. 021005, 10 2022. ISSN 1048-9002. Disponível em: <https://doi.org/10.1115/1.4055808>. Cited on page 14.

LAZAROV, B. S.; JENSEN, J. S. Low-frequency band gaps in chains with attached non-linear oscillators. *International Journal of Non-Linear Mechanics*, Elsevier, v. 42, n. 10, p. 1186–1193, 2007. Cited on page 22.

LIU, L.; HUSSEIN, M. I. Wave motion in periodic flexural beams and characterization of the transition between bragg scattering and local resonance. *Journal of Applied Mechanics*, v. 79, n. 1, 2012. Cited on page 8.

LIU, X. et al. Wave propagation characterization and design of two-dimensional elastic chiral metacomposite. *Journal of Sound and Vibration*, v. 330, n. 11, p. 2536–2553, 2011. Cited 2 times on pages 3 and 9.

LIU, Z. et al. Locally resonant sonic materials. *science*, American Association for the Advancement of Science, v. 289, n. 5485, p. 1734–1736, 2000. Cited on page 8.

LUST, K. Improved numerical floquet multipliers. *International Journal of Bifurcation and Chaos*, World Scientific, v. 11, n. 09, p. 2389–2410, 2001. Cited on page 37.

MACE, B. R. Discussion of "dynamics of phononic materials and structures: historical origins, recent progress and future outlook"(hussein, mi, leamy, mj, and ruzzene, m., 2014, asme appl. mech. rev., 66 (4), p. 040802). *Applied Mechanics Reviews*, American Society of Mechanical Engineers, v. 66, n. 4, p. 045502, 2014. Cited on page 7.

MANKTELOW, K. et al. Finite-element based perturbation analysis of wave propagation in nonlinear periodic structures. *Mechanical Systems and Signal Processing*, v. 39, n. 1-2, p. 32–46, 2013. Cited on page 12.

MATLACK, K. H. et al. Composite 3d-printed metastructures for low-frequency and broadband vibration absorption. *Proceedings of the National Academy of Sciences*, National Acad Sciences, v. 113, n. 30, p. 8386–8390, 2016. Cited 3 times on pages 3, 9, and 22.

MATOS, P. H. et al. Analytical and experimental investigation of flexural waves in horizontal pipes conveying two-phase periodic intermittent flow. *Applied Acoustics*, Elsevier, v. 192, p. 108714, 4 2022. ISSN 0003-682X. Cited on page 11.

MEAD, D. Wave propagation and natural modes in periodic systems: Ii. multi-coupled systems, with and without damping. *Journal of Sound and Vibration*, v. 40, n. 1, p. 19–39, 1975. ISSN 0022-460X. Disponível em: <https://www.sciencedirect.com/science/article/pii/S0022460X75802288>. Cited on page 2.

MEAD, D. Wave propagation in continuous periodic structures: Research contributions from southampton, 1964–1995. *Journal of Sound and Vibration*, v. 190, n. 3, p. 495–524, 1996. ISSN 0022-460X. Disponível em: <https://www.sciencedirect.com/science/article/pii/S0022460X96900760>. Cited on page 6.

MENG, H. et al. 3d rainbow phononic crystals for extended vibration attenuation bands. *Scientific Reports*, Nature Publishing Group, v. 10, n. 1, p. 1–9, 2020. Cited 4 times on pages 2, 6, 7, and 9.

MENG, H. et al. Investigation of 2d rainbow metamaterials for broadband vibration attenuation. *Materials*, v. 13, n. 22, p. 1–9, 2020. Cited on page 7.

MENG, H. et al. Optimal design of rainbow elastic metamaterials. *International Journal of Mechanical Sciences*, Elsevier Ltd, v. 165, p. 105185, jan 2020. ISSN 00207403. Cited 2 times on pages 55 and 65.

MENG, H. et al. Rainbow metamaterials for broadband multi-frequency vibration attenuation: Numerical analysis and experimental validation. *Journal of Sound and Vibration*, Academic Press, v. 465, p. 115005, 1 2020. ISSN 10958568. Cited 3 times on pages 6, 9, and 78.

MICKENS, R. Mathematical and numerical study of the duffing-harmonic oscillator. *Journal of Sound and Vibration*, v. 244, n. 3, p. 563–567, 2001. Cited on page 33.

MOHAN, S.; HAHN, E. J. Design of Squeeze Film Damper Supports for Rigid Rotors. *Journal of Engineering for Industry*, v. 96, n. 3, p. 976–982, 08 1974. ISSN 0022-0817. Cited on page 15.

MOROSI, S.; SANTOS, I. F. Active lubrication applied to radial gas journal bearings. part 1: Modeling. *Tribology International*, v. 44, n. 12, p. 1949–1958, 2011. ISSN 0301-679X. Disponível em: <https://www.sciencedirect.com/science/article/pii/S0301679X1100226X>. Cited on page 15.

MOSQUERA-SÁNCHEZ, J.; De Marqui, C. Broadband and multimode attenuation in duffing- and nes-type piezoelectric metastructures. *International Journal of Mechanical Sciences*, v. 270, p. 109084, 2024. ISSN 0020-7403. Disponível em: <https://www.sciencedirect.com/science/article/pii/S0020740324001279>. Cited 3 times on pages 2, 3, and 13.

MUHAMMAD et al. Forest trees as naturally available seismic metamaterials: Low frequency rayleigh wave with extremely wide bandgaps. *International Journal of Structural Stability and Dynamics*, v. 20, n. 14, 2020. Cited 2 times on pages 10 and 11.

MUSZYNSKA, A. *Rotordynamics*. Boca Raton, FL: CRC Press - Taylor & Francis Group, 2005. Cited 5 times on pages 25, 26, 28, 46, and 66.

NADKARNI, N. et al. Dynamics of periodic mechanical structures containing bistable elastic elements: From elastic to solitary wave propagation. *Physical Review E - Statistical, Nonlinear, and Soft Matter Physics*, v. 90, n. 2, 2014. Cited on page 12.

NARAYANAN, S.; SEKAR, P. A frequency domain based numeric–analytical method for non-linear dynamical systems. *Journal of sound and vibration*, Elsevier, v. 211, n. 3, p. 409–424, 1998. Cited on page 35.

NARISETTI, R. et al. A perturbation approach for predicting wave propagation in one-dimensional nonlinear periodic structures. *Journal of Vibration and Acoustics, Transactions of the ASME*, v. 132, n. 3, p. 0310011–03100111, 2010. Cited 3 times on pages 2, 3, and 12.

NEWTON, I. *Principia - Book II.* [S.l.]: Imprimatur S. Pepys, Reg. Soc. Præses, London, 1686. Cited on page 2.

ORMONDROYD, J. Theory of the dynamic vibration absorber. *Transaction of the ASME*, v. 50, p. 9–22, 1928. Cited on page 18.

PAI, P. et al. Acoustic metamaterial beams based on multi-frequency vibration absorbers. *International Journal of Mechanical Sciences*, v. 79, p. 195–205, 2014. Cited 2 times on pages 3 and 9.

PIERART, F. G.; SANTOS, I. F. Active lubrication applied to radial gas journal bearings. part 2: Modelling improvement and experimental validation. *Tribology International*, v. 96, p. 237–246, 2016. ISSN 0301-679X. Disponível em: <https://www.sciencedirect.com/science/article/pii/S0301679X15005721>. Cited on page 15.

POLICARPO, H. et al. Dynamical response of a multi-laminated periodic bar: Analytical, numerical and experimental study. *Shock and Vibration*, v. 17, n. 4-5, p. 134016, 2010. Disponível em: <https://onlinelibrary.wiley.com/doi/abs/10.3233/SAV-2010-0545>. Cited on page 7.

RANKINE, W. M. On the centrifugal force of rotating shafts. *Van Nostrand's Eclectic Engineering Magazine (1869-1879)*, Center for Research Libraries, v. 1, n. 7, p. 598, 1869. Cited on page 25.

RAZZAK, M. A. A simple harmonic balance method for solving strongly nonlinear oscillators. *Journal of the Association of Arab Universities for Basic and Applied Sciences*, Elsevier, v. 21, p. 68–76, 2016. Cited on page 33.

RIBEIRO, E. A. et al. Passive vibration control in rotor dynamics: Optimization of composed support using viscoelastic materials. *Journal of Sound and Vibration*, v. 351, p. 43–56, 2015. ISSN 0022-460X. Disponível em: <https://www.sciencedirect.com/science/article/pii/S0022460X15003181>. Cited on page 20.

RICHARDS, D.; PINES, D. Passive reduction of gear mesh vibration using a periodic drive shaft. *Journal of Sound and Vibration*, v. 264, n. 2, p. 317–342, 2003. ISSN 0022-460X. Disponível em: <https://www.sciencedirect.com/science/article/pii/S0022460X02012130>. Cited on page 7.

ROSSO, C. et al. On the implementation of metastructures in rotordynamics. In: *Rotating Machinery, Vibro-Acoustics & Laser Vibrometry, Volume 7.* [S.l.]: Springer, 2019. p. 43–51. Cited on page 14.

ROSSO, C. et al. On the implementation of metastructures in rotordynamics. *Conference Proceedings of the Society for Experimental Mechanics Series*, Springer, Cham, p. 43–51, 2019. Cited on page 14.

RUZZENE, M. et al. Wave beaming effects in two-dimensional cellular structures. *Smart Materials and Structures*, v. 12, n. 3, p. 363–372, 2003. Cited on page 11.

SAEED, A. S. et al. A review on nonlinear energy sinks: designs, analysis and applications of impact and rotary types. *Nonlinear Dynamics*, Springer, v. 111, n. 1, p. 1–37, 2023. Cited on page 13.

SÁNCHEZ-DEHESA, J. et al. Noise control by sonic crystal barriers made of recycled materials. *The Journal of the Acoustical Society of America*, v. 129, n. 3, p. 1173–1183, 03 2011. Disponível em: <https://doi.org/10.1121/1.3531815>. Cited on page 6.

SANTOS, I. F. Controllable sliding bearings and controllable lubrication principles—an overview. *Lubricants*, v. 6, n. 1, 2018. ISSN 2075-4442. Disponível em: <https://www.mdpi.com/2075-4442/6/1/16>. Cited on page 15.

SHENG, P. et al. Vibration properties and optimized design of a nonlinear acoustic metamaterial beam. *Journal of Sound and Vibration*, v. 492, p. 115739, 2021. Cited 3 times on pages 2, 3, and 12.

SKUBACHEVSKII, A. L.; WALTHER, H.-O. On the floquet multipliers of periodic solutions to non-linear functional differential equations. *Journal of Dynamics and Differential Equations*, Springer, v. 18, n. 2, p. 257–355, 2006. Cited on page 37.

SLATER, J. C. Mousai: An open source harmonic balance solver for nonlinear systems. In: *13th ASME Dayton Engineering Sciences Symposium*. Dayton, OH: [s.n.], 2017. Cited on page 33.

SMITH, M. C. Synthesis of mechanical networks: the inerter. *IEEE Transactions on automatic control*, IEEE, v. 47, n. 10, p. 1648–1662, 2002. Cited on page 10.

SOUSA, V. D. et al. Tunable metamaterial beam with shape memory alloy resonators: Theory and experiment. *Applied Physics Letters*, v. 113, n. 14, 2018. Cited on page 13.

STEFFEN, V.; RADE, D. Absorbers, vibration. In: BRAUN, S. (Ed.). *Encyclopedia of Vibration*. Oxford: Elsevier, 2001. p. 9–26. ISBN 978-0-12-227085-7. Disponível em: <https://www.sciencedirect.com/science/article/pii/B0122270851001764>. Cited on page 18.

SUGINO, C. et al. A general theory for bandgap estimation in locally resonant metastructures. *Journal of Sound and Vibration*, v. 406, p. 104–123, 2017. Cited 4 times on pages 7, 9, 22, and 23.

SUN, H. et al. Theory of metamaterial beams for broadband vibration absorption. *Journal of Intelligent Material Systems and Structures*, Sage Publications Sage UK: London, England, v. 21, n. 11, p. 1085–1101, 2010. Cited 3 times on pages 8, 44, and 45.

TIMBÓ, R. et al. Ross - rotordynamic open source software. *Journal of Open Source Software*, The Open Journal, v. 5, n. 48, p. 2120, 2020. Disponível em: <https://doi.org/10.21105/joss.02120>. Cited 3 times on pages 39, 40, and 85.

TRAINITI, G.; RUZZENE, M. Non-reciprocal elastic wave propagation in spatiotemporal periodic structures. *New Journal of Physics*, v. 18, n. 8, p. 083047, 2016. Cited on page 11.

TSAKMAKIDIS, K. L. et al. 'Trapped rainbow' storage of light in metamaterials. *Nature*, v. 450, n. 7168, p. 397–401, nov 2007. ISSN 14764687. Disponível em: <https://www.nature.com/articles/nature06285>. Cited on page 6.

VASILEIADIS, T. et al. Progress and perspectives on phononic crystals. *Journal of Applied Physics*, AIP Publishing LLCAIP Publishing, v. 129, n. 16, p. 160901, apr 2021. ISSN 0021-8979. Disponível em: <https://aip.scitation.org/doi/10.1063/5.0042337>. Cited on page 6.

VASSEUR, J. O. et al. Complete acoustic band gaps in periodic fibre reinforced composite materials: the carbon/epoxy composite and some metallic systems. *Journal of Physics: Condensed Matter*, v. 6, n. 42, p. 8759, oct 1994. Disponível em: <https://dx.doi.org/10.1088/0953-8984/6/42/008>. Cited on page 6.

WALSER, R. M. Metamaterials: What are they? what are they good for? In: *APS March Meeting Abstracts*. [S.l.: s.n.], 2000. p. Z5–001. Cited on page 6.

WALSER, R. M. Electromagnetic metamaterials. In: LAKHTAKIA, A. et al. (Ed.). *Complex Mediums II: Beyond Linear Isotropic Dielectrics*. SPIE, 2001. v. 4467, p. 1 – 15. Disponível em: <https://doi.org/10.1117/12.432921>. Cited 2 times on pages 6 and 7.

WU, F. et al. Current progress of acoustic metastructures: Design strategy and prospective application. *Advanced Engineering Materials*, Wiley Online Library, v. 27, n. 10, p. 2402910, 2025. Cited on page 7.

WU, L. et al. A brief review of dynamic mechanical metamaterials for mechanical energy manipulation. *Materials Today*, Elsevier, v. 44, p. 168–193, apr 2021. ISSN 1369-7021. Cited on page 6.

XIA, Y. et al. Dramatic bandwidth enhancement in nonlinear metastructures via bistable attachments. *Applied Physics Letters*, v. 114, n. 9, 2019. Cited 4 times on pages 2, 3, 11, and 13.

XIA, Y. et al. Bistable attachments for wideband nonlinear vibration attenuation in a metamaterial beam. *Nonlinear Dynamics*, v. 102, n. 3, p. 1285–1296, 2020. Cited 5 times on pages 2, 3, 11, 13, and 71.

XIAO, Y. et al. Closed-form bandgap design formulas for beam-type metastructures. *Mechanical Systems and Signal Processing*, Elsevier, v. 159, p. 107777, 2021. Cited on page 9.

XIAO, Y. et al. Broadband locally resonant beams containing multiple periodic arrays of attached resonators. *Physics Letters A*, v. 376, n. 16, p. 1384–1390, 2012. Cited 2 times on pages 3 and 10.

XU, Q. et al. Vibration characteristics of multi-acoustic metamaterials rotor with geometrical nonlinearity. *Nonlinear Dynamics*, Springer, p. 1–17, 2023. Cited 2 times on pages 3 and 14.

YANG, X.-D. et al. Dynamics of Structures with Distributed Gyroscopes: Modal Discretization Versus Spatial Discretization. *Applied Sciences 2020, Vol. 10, Page 160*, Multidisciplinary Digital Publishing Institute, v. 10, n. 1, p. 160, dec 2019. Cited on page 14.

ZHU, J. et al. Acoustic rainbow trapping. *Scientific Reports*, v. 3, p. 1728, 4 2013. ISSN 20452322. Disponível em: <https://www.nature.com/articles/srep01728>. Cited on page 6.

ZHU, R. et al. A chiral elastic metamaterial beam for broadband vibration suppression. *Journal of Sound and Vibration*, v. 333, n. 10, p. 2759–2773, 2014. Cited on page 9.